Fluorescence Spectroscopy and Electrical Transport in 1D-Semiconductors

From Individual Nanostructures to Hybrid Devices

Anton Myalitsin

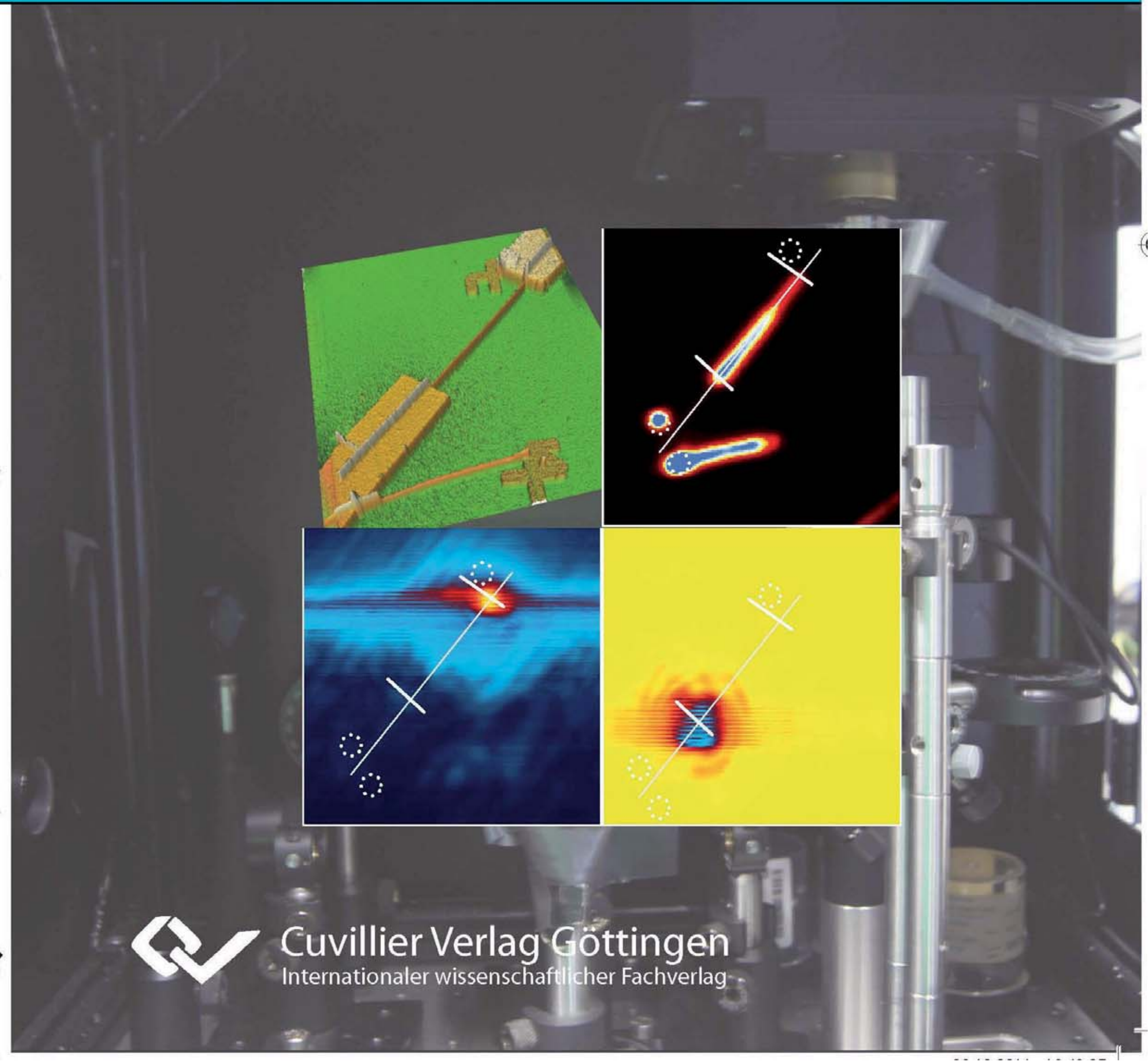

Cuvillier Verlag Göttingen
Internationaler wissenschaftlicher Fachverlag

Fluorescence Spectroscopy and Electrical Transport in 1D-Semiconductors

From Individual Nanostructures to Hybrid Devices

Ph. D. Thesis

for the attainment of the degree

Doctorate rerum naturalis
(Dr. rer. nat.)

submitted by

Anton Myalitsin

Department of Physical Chemistry
University of Hamburg
Hamburg, GERMANY

2011

Bibliografische Information der Deutschen Nationalbibliothek
Die Deutsche Nationalbibliothek verzeichnet diese Publikation in der Deutschen Nationalbibliografie; detaillierte bibliografische Daten sind im Internet http://dnb.d-nb.de abrufbar.
1. Aufl. - Göttingen: Cuvillier, 2011
Zugl.: Hamburg, Univ., Diss., 2011

978-3-86955-893-6

Gutachter der Dissertation:	Prof. Dr. Alf Mews Jun.-Prof. Dr. Christian Klinke
Gutachter der Disputation:	Prof. Dr. Alf Mews Jun.-Prof. Dr. Julien Bachmann Dr. Hauke Heller
Datum der Disputation:	26. 08. 2011

Nonnenstieg 8, 37075 Göttingen
Telefon: 0551-54724-0
Telefax: 0551-54724-21
www.cuvillier.de

1. Auflage, 2011
Gedruckt auf säurefreiem Papier

978-3-86955-893-6

I may not have gone
where I intended to go,
but I think I have ended up
where I needed to be.

- Douglas Adams -

Abstract

Subject of this dissertation is the investigation of inorganic cadmium-based nanowires by optical and electrical means. CdSe and CdS are structurally similar materials with a direct band gap in the visible region of the electromagnetic spectrum. Their size-dependent optical properties make them valuable materials for nanoscale devices.

Atomic force microscopy, scanning fluorescence microscopy, and transmission electron microscopy were used for experimental investigation. The home-built confocal microscope was reconstructed in a new lab and additional equipment for optoelectrical measurements was implemented in the setup; a detailed account of this is given.

Four different types of nanostructures were investigated in detail: First, a diameter dependence of the optical band gap of single CdSe nanowires was established. Simultaneously, theoretical calculations of the band gap's diameter-dependence within the effective-mass approximation were performed, taking into account quantization, electron-hole Coulomb interaction, and dielectric mismatch, which were found to be in agreement with experimental results. Further, the effects of alternating wurtzite and zinc blende segments along the nanowire axis were analyzed, concluding that the wavefunctions are not localized inside these segments but rather spread over a large domain.

Second, a hybrid CdSe-Bi-carbon nanotube system was studied. The optical properties of this structure were strongly influenced by the bismuth catalyst which is needed for the nanowire growth. The CdSe nanowires exhibited a decrease in diameter and an increase in photoluminescence towards the catalyst. This was explained by a gradual doping of the CdSe through the infusion of bismuth during growth.

Third, CdS nanowires were asymmetrically contacted with different metals and their electronic transport behavior was studied in a two-terminal field-effect transistor configuration. The electronic band structure along the wire was modulated by a lateral drain-source bias as well as an external electric field applied through a back-gate electrode. Thereby, a direct relation between the fluorescence and the photocurrent was demonstrated. By applying a bias across the CdS nanowire axis, the dissociation of electrons and holes was either promoted or suppressed.

Fourth, the process of light absorption in a CdSe-P3HT hybrid photovoltaic device was studied. A continuous tuning of the excitation light revealed that the absorption does not only happen in the CdSe, but a more complex process at the polymer-nanocrystal interface is responsible for the creation and separation of electron-hole pairs.

Zusammenfassung

Diese Dissertation befasst sich mit der optischen und elektrischen Untersuchung von anorganischen Nanodrähten aus CdSe und CdS. Beide Cadmiumverbindungen sind strukturell ähnliche Halbleiter mit einer direkten Bandlücke im sichtbaren Bereich des elektromagnetischen Spektrums. Die optischen Eigenschaften der Nanodrähte hängen von ihrer räumlichen Ausdehnung, insbesondere von ihrem Durchmesser, ab und machen sie dadurch zu einem interessantem Ausgangmaterial für nanoskalige Anwendungen.

Die Experimente wurden mit Rasterkraftmikroskopie, Fluoreszenz- und Transmissionselektronenmikroskopie durchgeführt. Ein speziell angepasstes konfokales Mikroskop wurde in einem neuen Labor wiederaufgebaut und auf andere Anwendungsgebiete erweitert. In den Aufbau wurde eine spezielle Ausstattung für optoelektronische Messungen integriert.

Insgesamt wurden vier unterschiedliche Typen von Nanostrukturen untersucht: Zunächst wurde im Rahmen dieser Arbeit die Abhängigkeit der optischen Bandlücke vom Durchmesser einzelner CdSe-Nanodrähte experimentell erfasst. Dies wurde mit einer Simulation dieser Abhängigkeit verglichen, wobei in dem Modell der Effektiven-Masse-Näherung der Einfluss der Quantisierung, die Coulombwechselwirkung der Elektron-Loch-Paare und Spiegelladungen berücksichtigt werden. Die theoretischen Ergebnisse stehen in guter Übereinstimmung mit dem Experiment. Außerdem wurden Bereiche mit abwechselnder Wurtzit- und Zinkblendestruktur entlang der Nanodrahtachse analysiert. Es zeigt sich, dass die Wellenfunktionen nicht innerhalb einzelner Abschnitte lokalisiert sind, sondern mehrere Segmente überspannen.

Zweitens wurde ein CdSe-Bi-Kohlenstoff-Hybridsystem untersucht. Optische Eigenschaften dieser Struktur wurden stark vom Bismuth-Katalysator beeinflusst, der für das Wachstum des Nanodrahtes verwendet wurde. Der Durchmesser der Drähte verringerte sich und die Photolumineszenz nahm in Richtung des Katalysators zu. Dies kann durch eine sukzessive Dotierung des CdSe-Drahtes mit Bismuth während des Wachstumsprozesses erklärt werden.

Drittens wurden CdS-Nanodrähte asymmetrisch mit unterschiedlichen Metallen kontaktiert und als Feldeffekt-Transistor angeordnet. Anschließend wurde die elektrische Leitfähigkeit der Drähte untersucht. Die elektronische Bandstruktur entlang des Drahtes wurde mit einer lateralen Spannung zwischen

Source und Drain variiert. Dabei wurde ein direkter Zusammenhang zwischen Photolumineszenz und Photostrom demonstriert. Beim Anlegen einer Spannung entlang der Achse des CdS-Drahtes konnte die Trennung der Elektronen und Löcher kontrolliert gefördert oder unterdrückt werden.

Schließlich wurde der Prozess der Lichtabsorption in einem CdSe-P3HT-Photoelement untersucht. Kontinuierliches Durchstimmen der Wellenlänge des Anregungslichts hat gezeigt, dass der Absorptionsprozess nicht ausschließlich im CdSe stattfindet, sondern dass ein komplexer Vorgang an der Polymer-Nanokristall-Grenzfläche für die Erzeugung und den Zerfall der Elektron-Loch Paare verantwortlich ist.

Contents

1 Introduction

In the last decades *nanoscience* emerged as a new research field at the interface of chemistry and physics. Materials, whose properties were well-known and understood, show novel and unexpected properties when their size is reduced from bulk to just a few nanometers in one or more dimensions[1].

In general, two effects are responsible for the change in material properties upon approaching the nanoscale: First, the surface to volume ratio increases dramatically when the dimensions shrink to only a few nanometers. For example, in nanocrystals with a diameter of about $\sim 2\,\text{nm}$ almost half of the atoms are located at the surface and are available for chemical reactions. At the same time, surface atoms contribute significantly to the Gibbs free energy of the nanoparticles, changing their thermodynamic properties. E.g., nanocrystals show a melting point depression as their size decreases[1].

Second, with sizes of only a few nanometer the assumption of an infinite periodicity of the crystal lattice is no longer valid. Therefore, electrons and holes feel a confinement in one, two and three dimensions, and so-called quantum wells, wires or dots are formed, respectively. Further, since the movement of charges is restricted spatially, the Coulomb interaction becomes more important.

Overall, this means that for given materials, their properties can be tuned solely by size (and morphology) variation. Perhaps one of the best-known and extensively studied examples is the size-dependence of the optical band gap in semiconductor nanocrystals[2].

1.1 Motivation

Over the last decade nanowires (NWs) became the subject of intensive research. As an advantage to zero dimensional quantum dots, one dimensional NWs can be used as building elements to arrange hierarchical superstructures for optical, optoelectronic and electrical instruments. These NWs can function as both, active devices and interconnections at the same time[3]. In addition, their internal structure serves as a guide for charge carriers and photons along one axis. Direct band gap materials are of particular interest for light emission applications, since their radiative recombination is converted primarily into photon emission. Several pioneering studies have demonstrated the use of NWs, e.g., as gain media for lasers[4], gas sensors[5], photo sensitizers for solar cells[6], field-effect transistors[7] or as probes for biological tissues[8]. However, their diameter is typically far above the Bohr radius and thus quantization effects are less prominent. With the catalyst-based solution-liquid-solid (SLS) synthesis, NWs with diameters smaller than the Bohr radius have been prepared in larger quantities[9]. Such NWs are of special interest for devices based on their optical properties since the band gap depends on the diameter, which is relatively easy to tailor[10–14]. In fact, measurements on ensembles of NWs revealed an increase of absorption and photoluminescence (PL) peak energies with decreasing diameter[12–14].

Optical measurements on single NWs can reveal electronic band structure properties that often remain hidden in averaging experiments on ensembles. Such measurements show many interesting features, yet not all of them are fully understood. In CdSe NWs, prepared with wet-chemical methods, structural variations[10] were observed, as well as fluorescence intensity fluctuations along individual NWs[15]. Alterations in crystal structure between wurtzite and zinc blende segments, with different band gaps and offsets, were reported to lead to a formation of separated quantum mechanical systems, a model which was used to explain the "hot spots" in the PL signal[15–17], with a blinking behavior similar to quantum dots (QDs). In other experiments, however, CdSe NWs have been reported to behave like single quantum mechanical systems[18,19]. The interpretation of fluorescence data is further complicated by photobrightening effects in the presence of organic ligands[20], by agglomerates of colloidal nanoparticles[21] and by variations in ligand coverage, that may lead to spectral heterogeneity as well as different emission intensities along the wire[22].

Since micro-electronic devices like transistors in integrated circuits are approaching the nano scale limit, the traditional "top-down" approach, which relies on conventional lithography techniques, to create smaller and smaller templates, from which the device is finally built, becomes extremely expensive[23]. Therefore, the "bottom-up" approach, i.e. building devices from atoms and molecules, offers a new perspective for the miniaturization of electronic components[3]. Recent advances in wet-chemical synthesis resulted in applications of hybrid nanostructures, containing NWs in photovoltaic elements[24], photocatalysis[25] and electronic devices[26]. However, for that a detailed understanding of the relation between the morphology of the nanostructure and its electronic properties is required.

1.2 Scope of this Work

This thesis has been organized as follows: Chapter 1 provides an introduction. The second chapter gives a concise overview of the theoretical background used in this work. The crystalline structure of CdSe and CdS nanowires are described. Models, which were used to calculate the optical band gap, are explained and basic terms of electrical measurements in semiconductor devices are defined.

In the third chapter the experimental methods to synthesize nanowires are outlined and the equipment used to characterize and manipulate the nanostructures is briefly described. In particular, parameters of the components, which comprise the confocal microscope are addressed and explanations for their particular use are given.

In Chapters 4, 5 and 6 the results of this thesis are presented:

Chapter 4 describes the close connection between the diameter of a NW and their band gap. A detailed correlation between the morphology and the fluorescence of NWs was established and a model for the shift in the exciton energy was developed. Further, CdSe-carbon nanotubes hybrids were investigated by PL spectroscopy.

In Chapter 5, the interplay between the PL and photocurrent (PC) is discussed. Certain regions of CdS NWs were illuminated to locally create electron-hole pairs which in turn were separated by a bias or an external electric field.

The subject of chapter 6 are heterojunction solar cells, built from CdSe nanocrystals as absorbers and poly(3-hexylthiophene-2,5-diyl) (P3HT), a common hole-conducting polymer in organic photovoltaics. The influence of the CdSe nanoparticles on the performance of the photovoltaic cell was studied and the charge generation and diffusion processes were considered.

In Chapter 7, the results are summarized and an outlook for further experiments are given.

2 Theoretical Background

In this chapter fundamental solid state theories, underlying the interpretation of the experiments in the later chapters, are presented.

2.1 II-VI Nanowires

Nanowires (NWs) are anisotropic nanocrystals, elongated along one axis. The wires can have any length from a few 100 nm up to several 100 µm. If the diameter of the wire is small enough to induce quantization effects, they are also referred to as quantum wires or quasi-1 D structures.

Crystal Structure

At atmospheric pressure II-VI semiconductors, such as CdSe or CdS, exist in two modifications of their crystal structure: wurtzite (WZ) in a hexagonal packing and zinc blende (ZB) in a cubic packing. The two structures are sketched in figure 2.1. CdSe NWs, grown by the SLS method, typically exhibit alternating lattice modifications with average segment lengths of only a few nm along their axes[10,13]. This is illustrated in figure 2.2 a and b) by transmission electron microscopy (TEM) images. The two phases differ in their respective band structure and, in particular, electron affinities, ionization potentials and fundamental band gaps[15,16,27–29].

The hexagonal structure consists of tetrahedrally coordinated Cd^{2+} and Se^{2-} atoms, stacked in the *ABAB* pattern. Zinc blende is also built up from

	CdSe		CdS	
	WZ	ZB	WZ	ZB
a / nm	0.430	0.607	0.414	0.582
b / nm	0.430	0.607	0.414	0.582
c / nm	0.701	0.607	0.675	0.582
space group	186 P6$_3$mc	216 F43m	186 P6$_3$mc	216 F43m

Table 2.1: Lattice parameters of CdSe and CdS for wurtzite (WZ) and zinc blende (ZB) modifications.

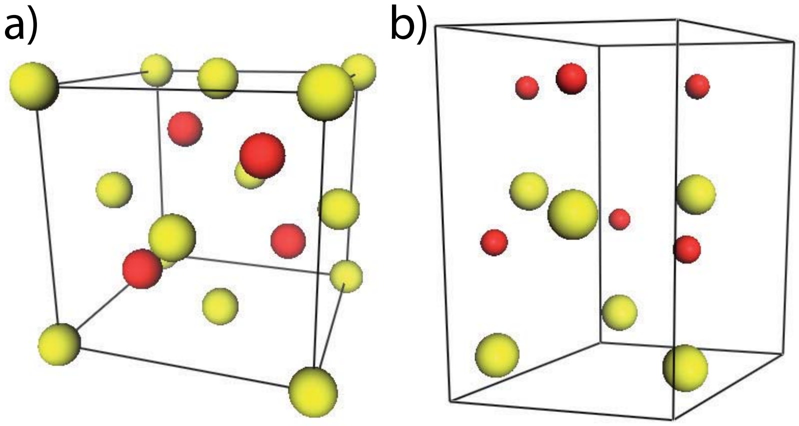

Figure 2.1: A sketch of the two possible crystal structures of CdSe: a) Zinc Blende (ZB) and b) Wurtzite (WZ) unit cell. The Cd^{2+}-ions are shown in yellow, the Se^{2-}-ions are red.

tetrahedrally coordinated atoms, but the structural pattern is *ABCABC*. The lattice parameters are given in table 2.1. Difference in inter-atomic distance between the cubic and hexagonal structure is very small along the growth axis, <1 Å, making it very difficult to distinguish between the two modifications. The differences along the a- and b-axis are around 30 % and can therefore be easily resolved. The space group is denoted with an integer from 1 to 230, followed by the Hermann-Mauguin notation. The first letter gives the Bravais lattice (*P* for primitive centering and *F* for face centred). The next three numbers and letters describe the most prominent symmetry operation visible when projected on one of the high symmetry directions of the crystal.

To determine the crystal structure of individual SLS-grown CdSe NWs they were deposited either on a copper grid with a thin carbon film or on a Si_3N_4-membrane and investigated with a transmission electron microscope (cf. section 4.1.2). In a TEM the electron beam is focused on a sample and the transmitted beam is either projected on a fluorescent screen or recorded with a digital camera. Areas with high electron density, i. e., heavy atoms, scatter electrons and appear dark in the image. In areas with low electron density, e. g., "empty space" and light atoms, the beam passes considerably unhindered and is recorded with high intensity. Therefore the TEM enables one to measure a 2-D projection of the 3-D crystal structure of the NW.

If the wire has a particular orientation, where the atomic layers are stacked behind each other, a high lattice contrast is obtained, as exemplarily shown in figure 2.2 a. Since the NWs are usually randomly oriented by the deposition, in most cases only one lattice plane can be observed, as shown in figure 2.2 b.

For a better understanding of possible orientations and the alteration between WZ and ZB segments, TEM images of a junction between these two

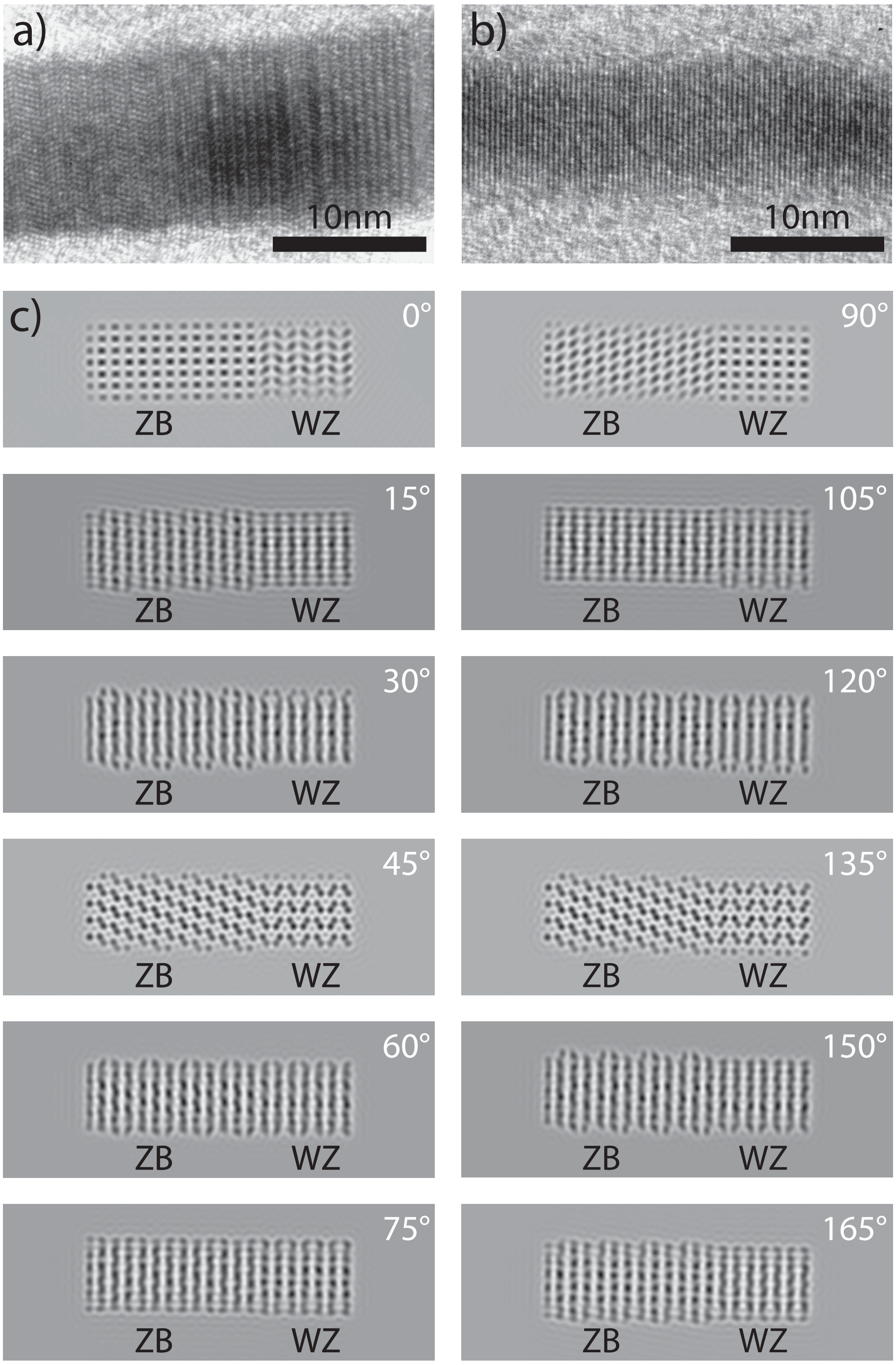

Figure 2.2: a) CdSe NW on a carbon film, the orientation corresponds to the simulated 45° image. b) A CdSe NW with an orientation, where the segments cannot be distinguished. c) Calculated TEM images, rotated in steps of 15°. The left part of the wire is zinc blende (ZB), the right segment is wurtzite (WZ). Only orientation in 45°/135° gives a clear distinction between both structures. Orientation at 0°/90° suggests that stacking faults may occur without changing between the ZB and WZ packing.

segments were simulated for different crystallographic orientations of the wire with the software SimulaTEM 1.3.2[30]. In the simulation the specimen is cut into several slices and the propagation of an electron wave is calculated after interacting with the Coulomb potential of each of the slices. Figure 2.2 c shows the simulated TEM image of a typical wire segment in different rotations. The left part of the wire consists of ZB, the right part of WZ, merged together. The NW was rotated around its growth axis in steps of 15°. The results of the simulations show that only the orientation at 45° and 135° allows for a clear distinction between both structures. Unfortunately in real samples stacking faults may rotate the lattice during growth around its main axis, leading to a different appearance of the same phase. In addition, both phases appear the same for different orientations. In the TEM, the substrate may be rotated by up to 10°, to achieve a favorable orientation.

2.2 Effective Mass Approximation

To calculate the electronic properties of a crystalline nanostructure with many thousands of atoms, one would have to consider all interactions between every atom core and every electron. Since this is not possible with computers available today, several approximations have to be made.

The effective mass approximation transfers fundamental properties of bulk to the nano-sized material in a descriptive way. It can be derived from the nearly free electron approach, assuming the charge in a crystal behaves like a free electron with a different ("effective") mass m^*, due to the influence of the lattice.

The energy of a particle is given by

$$E = \frac{\hbar^2 k^2}{2m^*} , \tag{2.1}$$

with the quasi-momentum k. Without any boundary conditions, the momentum can take any value.

In the next step the influence of the lattice potential is taken into account, i.e., the Coulomb interaction of the electrons with the positively charged atom cores and other electrons in the vicinity. This leads to a phase dependence of the wave function and a discontinuity of the energy at certain k-vectors. The band diagrams of CdS and CdSe in the WZ modification are shown in figure 2.3, calculated by the pseudopotential method[31]. High symmetry points in the reciprocal space are commonly labeled with capital letters Γ, X, L, U, K and W and the electronic band structure calculations are typically performed along

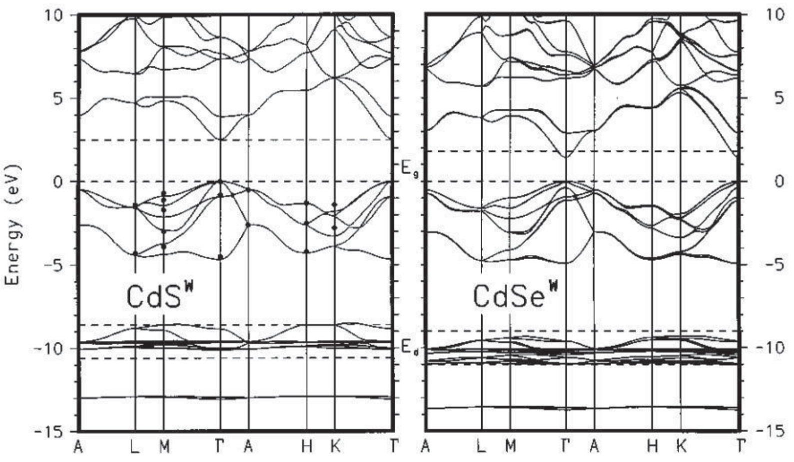

Figure 2.3: Full electronic band diagram for the WZ modification of a) CdS and b) CdSe, calculated by the pseudopotential method [31].

directions of the reciprocal space connecting such points. According to Bloch's theorem the wave functions can be separated into a plane wave and a function with the periodicity of the lattice:

$$\Psi(\mathbf{k}, \mathbf{r}) = e^{i\mathbf{k}\cdot\mathbf{r}} \times \psi(\mathbf{k}, \mathbf{r}) \, . \tag{2.2}$$

The effective mass of an electron in the conduction band is deduced from the energy dispersion $E(k)$ in the reciprocal space. Close to the Γ-Point, where the quasi-momentum equals zero, the conduction band is approximated by a parabola. The band curvature is referred to as the reciprocal of the effective mass:

$$\partial^2 E / \partial k^2 = \frac{\hbar^2}{m^*} \, . \tag{2.3}$$

The same consideration holds true for holes. Categorized by the valence band curvature, a distinction is made between heavy, light and split-off holes. For any given material the effective mass is a function of k and depends on the crystallographic axis.

In semiconductor-nanostructures an electron and hole can be bound by Coulomb interaction. Thus they can form a quasi-particle without a net charge, an exciton. In nanocrystals (NCs) in general and NWs in particular, the energy of an exciton can be decomposed into the fundamental band gap energy of the material E_g, the quantization energy E_q and the Coulomb interaction energy E_c:

$$E_\mathrm{exciton} = E_\mathrm{g} + E_\mathrm{q} + E_\mathrm{c} \, . \tag{2.4}$$

The Coulomb term acts over all coordinates and makes it therefore difficult to solve the Schrödinger equation. Therefore, the Coulomb interaction is disregarded when the quantization potential is calculated. Consequently, the electron and the hole do not interact with each other and the quantization energy is calculated separately for both of them. The Hamiltonian comprises then the kinetic energy of the electron and the hole in three dimensions, their confinement potential in radial direction $V_e(r,\varphi)$ and $V_h(r,\varphi)$ and the Coulomb interaction between both charges $W(\vec{r}_e - \vec{r}_h)$.

$$H = \frac{\hbar^2}{2m_e}\nabla_e^2 + V_e(r_e,\varphi_e) - \frac{\hbar^2}{2m_h}\nabla_h^2 + V_h(r_h,\varphi_h) + W(\vec{r}_e - \vec{r}_h)\,. \tag{2.5}$$

Further, the wave function is separated adiabatically into the radial coordinates r and φ on the one hand and the position of the center of mass of the exciton Z along the growth axis of the wire and the relative motion of the charges $z = z_e - z_h$ on the other hand. This is possible, because the confinement energy in radial direction, is much larger:

$$\Psi(r_e,\varphi_e,r_h,\varphi_h,Z,z) = e^{iKZ}\psi(z)\psi(r_e,\varphi_e)\psi(r_h,\varphi_h)\,. \tag{2.6}$$

The wave function, which solves the time-independent Schrödinger equation is a product of a plane wave along the wire axis and a Bessel function of the first kind in the radial direction within the wire:

$$\Psi_{m,k_z}(r,\varphi,z) = Ce^{-im\varphi}J_m\left(\frac{\beta_m}{R}r\right)e^{ik_z z}\,, \tag{2.7}$$

where C is a normalization constant and β_m is the m^{th} zero of $J_m(r)$. For the ground state of the exciton the values are $m = 0$ and $\beta_0 = 2.408$. The corresponding Hamiltonian is written as

$$H = \frac{\hbar^2}{2m_e}\nabla_e^2 + V_e(r_e,\varphi_e) - \frac{\hbar^2}{2m_h}\nabla_h^2 + V_h(r_h,\varphi_h)\,. \tag{2.8}$$

A suitable value for the depth of the potential is chosen for the environment, e.g., a ligand shell. Outside the wire, the k-vector is imaginary and the evanescent wave function is described by a MacDonald function. The continuity condition

$$\Psi(x)_{\text{in}} = \Psi(x)_{\text{out}}\,, \tag{2.9}$$

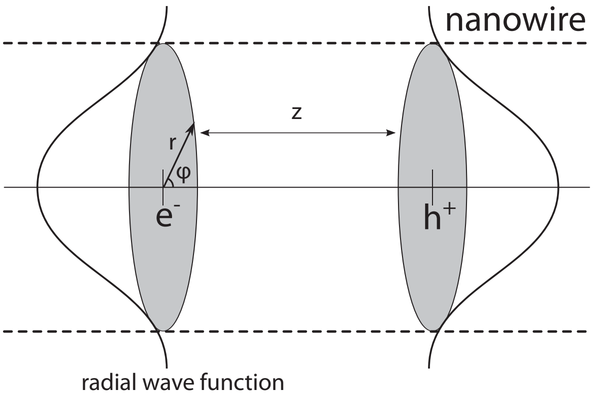

Figure 2.4: Illustration of the direct Coulomb interaction. The dashed line signifies the NW perimeter, where the radial part of the wave function, depicted as a solid curve, has to become zero. Integration over the radial variables of the electron and hole yields the "wave function discs", leaving only the relative distance z as a free parameter. To obtain the direct interaction "wave function discs" have to be integrated for every distance z.

as well as the so-called Ben Daniel-Duke boundary condition have to be fulfilled, which puts the following constitution on the mass flow of the electron and the hole at the interface[32]:

$$\left(\frac{1}{m^*}\frac{\partial}{\partial z}\psi(z)\right)_{\text{in}} = \left(\frac{1}{m^*}\frac{\partial}{\partial z}\psi(z)\right)_{\text{out}} . \tag{2.10}$$

These boundary conditions give the allowed quantization energies E_e and E_h. The eigenenergy problem can be solved numerically by a suitable software, e.g. Mathematica. Hereby a coefficient matrix is set up, the matrix is then diagonalized and the eigenvalues are obtained.

To obtain the Coulomb energy, a method described by Slachmuylders *et al.* was used[33,34]. The authors assume an infinitely high potential at the wire perimeter. This avoids the evanescent part of the wave function and simplifies the calculations significantly.

Further, the Coulomb potential is divided into a direct interaction $U_{\text{dir}}(z)$ between the electron and the hole, the induced interaction with the mirror charges outside the wire $U_{\text{ind}}(z)$ and the self-energy E_{self}, a potential energy felt by the electron and hole due to the polarization of the medium.

The direct potential is calculated by integrating over the radius r and angle φ of the electron and hole wave functions, weighted with their radial distribution for every relative distance z, as shown in figure 2.4. After calculating the direct potential for several different radii, an analytical function was fitted to the results[33].

The induced potential depends on the dielectric mismatch between the dielectric constants ϵ_1 inside the wire and ϵ_2 outside. The results were also fitted, but, depending on the mismatch ratio ϵ_1/ϵ_2, a unique set of fitting parameters was used[34].

Finally, the total Coulomb potential for the exciton is obtained by

$$U_{\text{tot}}(z) = C[U_{\text{ind}}(z) + U_{\text{dir}}(z)] + 2E_{\text{self}} \,. \tag{2.11}$$

With this potential the exciton binding energy is calculated numerically.

2.3 Electrical Measurements on Contacted MSM Structures

2.3.1 Schottky and Ohmic Contacts

Electrons fill the bands of a semiconductor according to the Fermi-Dirac distribution. The highest occupied energy level of a material at 0 K is denoted as the Fermi energy. The Fermi level lies inside a band for a metal and between the valence band and the conduction band for a semiconductor. Intrinsic semiconductors are not doped with impurity atoms, so that their Fermi energy E_F lies in the middle of the forbidden band gap. Their conductivity is very poor and is the result of thermally activated electrons in the conduction band and holes in the valence band. Additional charge carriers may be introduced to increase conductivity by doping. Hereby impurity atoms with an excess or deficiency of electrons are introduced into the material. The Fermi energy is then either lifted (n-doping) or lowered (p-doping).

When two different materials are brought into contact electrons flow from the material with the lower work function to that with the higher work function and their fermi levels equilibrate. Figure 2.5 shows the situation for an n-doped semiconductor, i.e., the Fermi energy lies closer to the conduction band, and two metals with different work functions. The contact is called ohmic, when majority charge carriers (electrons) do not encounter a barrier and the resulting current-voltage (I-V) curve of the device is linear. A rectifying I-V curve is observed, when the band alignment at the metal-semiconductor interface leads to a barrier for the major charge carriers (figure 2.5). The contact is then referred to as a Schottky contact and the barrier as a Schottky barrier.

Specific electronic states are created, when the periodicity of a crystal lattice terminates at its surface. This is specifically true for a metal-semiconductor interface. In metals the electronic states lead to a surface dipole, which contributes to the work function of the metal. In semiconductors, on the other hand, surface states lead to a “pinning” of the Fermi level above the valence band. For a high number of interface states the barrier height is independent of

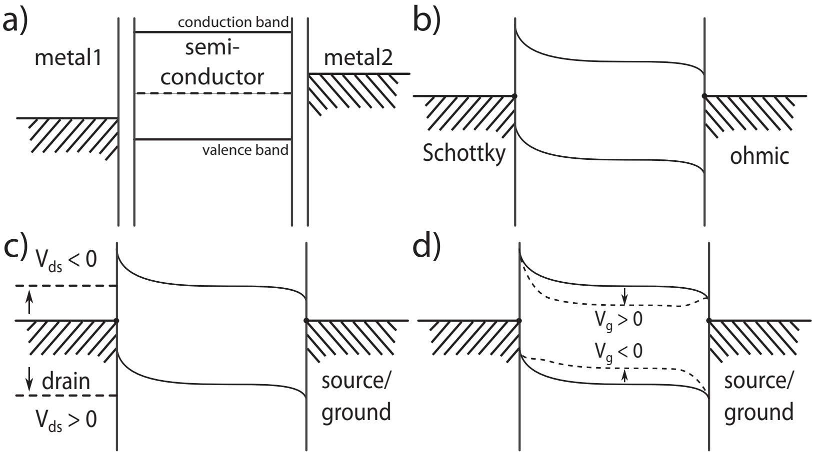

Figure 2.5: a) A semiconductor and two metals with different work functions. b) Ohmic and Schottky contacts between a metal and a n-doped semiconductor are formed.[35] c) Overview of the influence of the bias and gate on the bands of the metal-semiconductor device. A positive bias V_{ds} lowers the drain electrode, a negative bias lifts it. d) A positive gate voltage V_{g} may be applied to lower the bands of the semiconductor; a negative gate raises it.

the metal work function and is entirely determined by the surface properties of the semiconductor.

The most important definitions for electrical measurements are summarized in figure 2.5b. In the course of this thesis, the source was connected to the ground and the bias was applied at the drain. Positive bias lowers the drain potential, negative bias lifts it (figure 2.5c). The gate electrode was used to apply an electric field to shift the bands of the semiconductor: a positive gate lowers the position of the valence and conduction band, negative gate raises them (figure 2.5d). Since this drastically influences the conductivity of the semiconductor, this effect is widely used to utilize field effect transistors as switches in electrical devices.

2.3.2 Solar Cell

The photovoltaic effect, where absorbed light is converted to electrical energy, was first described by A. E. Becquerel in 1839, when he exposed a junction between an electrode and an electrolyte to light[36]. However, it did not receive much attention as a method to generate energy until the 1950s with the works of Chapin on silicon[37] and Reynolds on cadmium sulfide[38].

Semiconductors can absorb photons when illuminated, hereby creating excitons (electron-hole pairs). If the exciton binding energy, in form of Coulomb attraction, is overcome by an electric field, the electrons and holes can be spatially separated from each other. Once the charge carriers are free, they can be

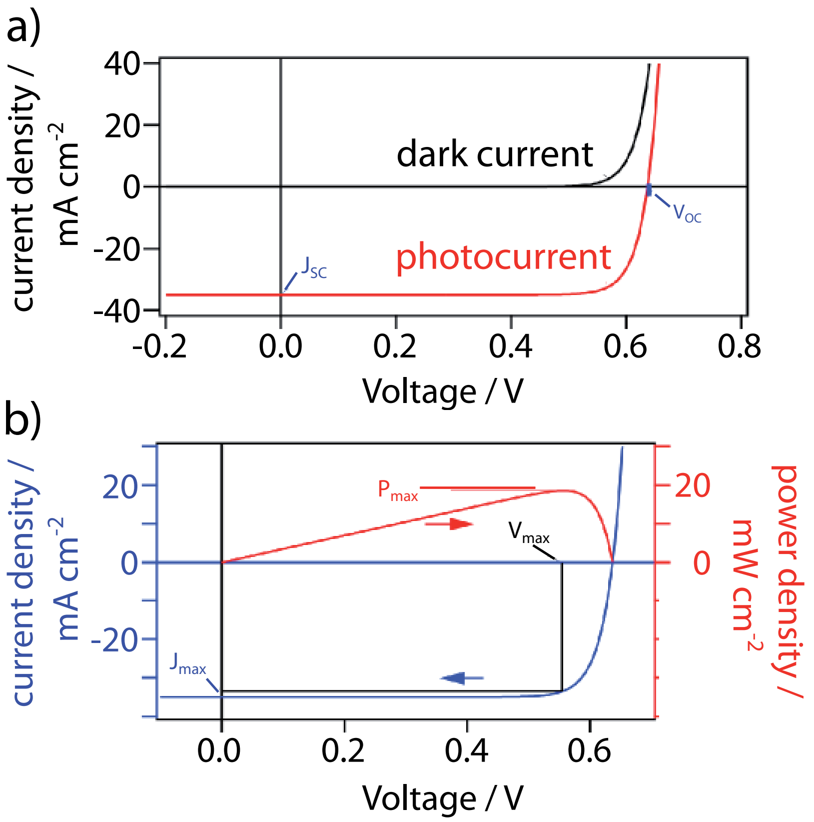

Figure 2.6: a) I-V characteristic of a solar cell in dark and under illumination. The maximum voltage is denoted by V_{oc} and the maximum current by J_{max}. b) The generated power is the product of the current and the voltage. Maximum power P_{max} output is obtained for a certain load with J_{max} and V_{max} [35].

collected at the metal contacts and contribute to the measured current. Without illumination solar cells display a diode I-V characteristic due to asymmetric contacts, as displayed in figure 2.6. Current flows for forward bias and is approximately zero for reverse bias. For an ideal diode, the dark current can be calculated as:

$$J_{\mathrm{dark}} = J_0 \left(e^{qV/k_B T} - 1 \right) , \tag{2.12}$$

where J_0 is a constant, k_B is the Boltzmann's constant and T is the absolute temperature.

When photons are absorbed during illumination excitons are created. They decay into electrons and holes in the depletion region by a built-in electric field and result in a short-circuit current J_{sc}. Thereby the whole curve is shifted

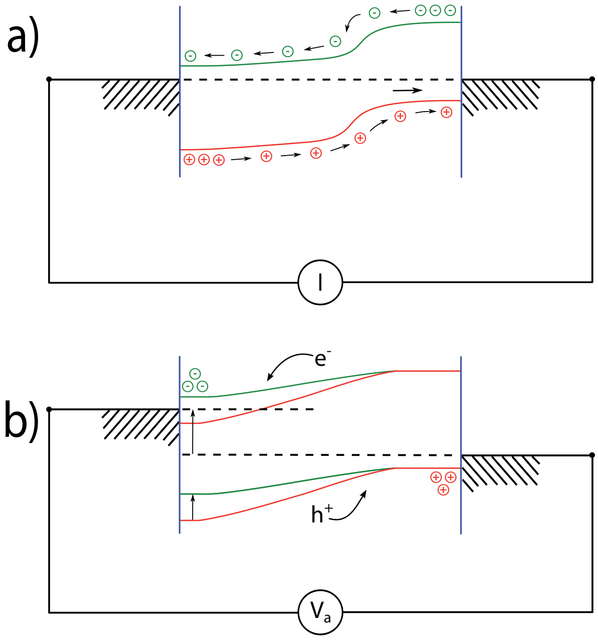

Figure 2.7: Different configurations of a solar cell: a) The band-diagram of a short-circuited solar cell under illumination. Excitons are separated by the electric field in the space charge region, and the short-circuit current I_{sc} flows. b) The band diagram for a cell with open contacts. The charges accumulate at the contacts and build-up the open-circuit voltage V_{oc}.[35]

down by a constant value. In a first approximation, the dark current and the photocurrent J_{sc} can be added:

$$J = J_0 \left(e^{qV/k_B T} - 1 \right) - J_{sc} \, . \tag{2.13}$$

With open contacts the potential difference reaches its maximum value at the open circuit voltage V_{oc} . The ideal diode equation 2.13 is then rearranged to

$$V_{oc} = \frac{k_B T}{q} \ln \left(\frac{J_{sc}}{J_0} + 1 \right) \tag{2.14}$$

With voltages $0 < V < V_{oc}$ the solar cell generates power. For $V < 0$ the device operates as a photodetector. The photocurrent depends on the light intensity, but is independent of the applied bias.

The solar cell power is given by

$$P = J \cdot V \tag{2.15}$$

The optimal load (electrical unit with a resistance) of the cell is then given by the resistance V_{max}/J_{max}. The efficiency η of a solar cell is described by the ratio of generated electrical power P_{el} and the power of the incident light P_{L}. The electrical power can be calculated from the current flow and the voltage applied. At both limits, I_{sc} and V_{oc}, the power is zero, reaching a maximum in between.

$$\eta = \frac{P_{\mathrm{el}}}{P_{\mathrm{L}}} = \frac{V_{\mathrm{max}} \times I_{\mathrm{max}}}{P_{\mathrm{L}}} = \frac{V_{\mathrm{oc}} \times I_{\mathrm{sc}} \times FF}{P_{\mathrm{L}}} \tag{2.16}$$

This equation also defines the fill factor FF as the ratio between $V_{\mathrm{max}} \times I_{\mathrm{max}}$ and $V_{\mathrm{oc}} \times I_{\mathrm{sc}}$ and is a measure for the steepness (or "squareness") of the I-V characteristic. Fill factors of good solar cells can reach around 60-70%.

The four parameters: V_{oc}, I_{sc}, FF and η are the key performance characteristics of a solar cell. These are usually measured under well-defined illumination conditions: The Standard Test Condition (STC) for solar cells is the Air Mass 1.5 spectrum, an incident power density of $1000\,\mathrm{W\,m^{-2}}$, and a temperature of $25\,^{\circ}\mathrm{C}$.

3 Experimental Methods

This chapter covers the experimental details of this thesis and describes the functionality of the equipment used. The emphasis lies on the detection of PL from single NWs and charge separation in the same structures. The first part of the experiments focused on fluorescence investigations of individual CdSe NWs. For this purpose a confocal microscope was used, which had been established previously[39]. During this thesis, the system was modified several times in order to address optoelectronic issues. In the second part of the experiments photoactive devices were fabricated and correlation between current flow and fluorescence was investigated.

The workflow is shown in figure 3.1. After the synthesis CdSe/CdS NWs were deposited from solution on the SiO_2 surface of the substrate. In contrast, carbon nanotubes (CNTs) are directly grown on the substrate. These samples were either directly used for optical measurements or contacted via lithography for optoelectronic investigations. To localize individual nanostructures and correlate them in the optical microscope, atomic force microscopy (AFM) and electronic microscope gold markers or corners of the membrane are used. To find a suitable working position, optical images and *I-V* curves were recorded.

The CdSe and CdS wires were excited with intensities of a few µW or less to avoid bleaching. CNTs, as they are (photo)chemically much more stable, were excited with up to a few mW in order to observe their Raman signal. Structural and spectral studies were performed on CdSe NWs. However, electrical studies were limited to thick CdS NWs and CdSe NCs due to their higher conductivity. In the end, the measurements were compared with both simulations and theoretical models.

3.1 Synthesis

CdSe Nanocrystals There are several methods to produce CdSe NCs with a high quantum yield. Typically, the CdSe particle is passivated with another material, such as CdS or ZnO (core-shell structure)[40]. For applications in photovoltaic devices this step was omitted to ease charge separation within the connected structures. For bare CdSe particles, CdO and tetraoctylphosphonic acid (TOPO) are loaded into a three neck flask and evacuated for about an

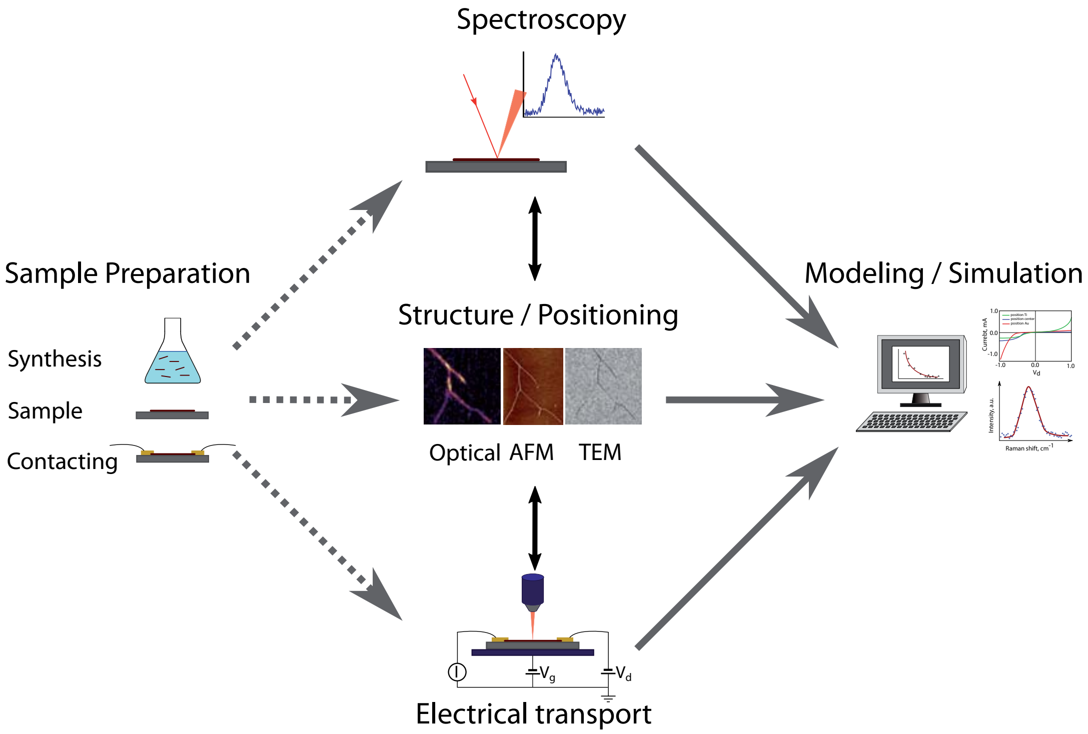

Figure 3.1: Workflow sketch.

hour. The flask was then filled with inert gas and heated stepwise to 320 °C until a clear solution showed that CdO had been completely dissolved. A fresh solution of Se/tributylphosphine (TBP) was injected and the temperature was reduced to 250 °C. The growth of the particles was observed by a change of the color of the solution. After a few minutes the reaction was quenched by rapid cooling of the solution to 50 °C and the particles were precipitated by injecting methanol. The NCs were purified by centrifugation and decantation in toluene or chloroform.

CdSe Nanowires Nanowires are synthesized under similar conditions as nanocrystals in the presence of low melting-point nanocrystals[41], according to the SLS mechanism. A scheme of the growth process is shown in figure 3.2a. As the catalyst melts, Cadmium and Selenium precursors dissolve in the Bismuth droplets. Upon saturation, CdSe precipitates and grows out of the catalyst particle in the form of a wire. As a competitive process CdSe nanodots grow directly in solution and have to be removed at the end of the reaction by centrifugation and fractional precipitation.

CdS Nanowires CdS nanowires are usually grown by chemical vapor deposition (CVD) (figure 3.2 b). As the reaction occurs at much higher temperatures

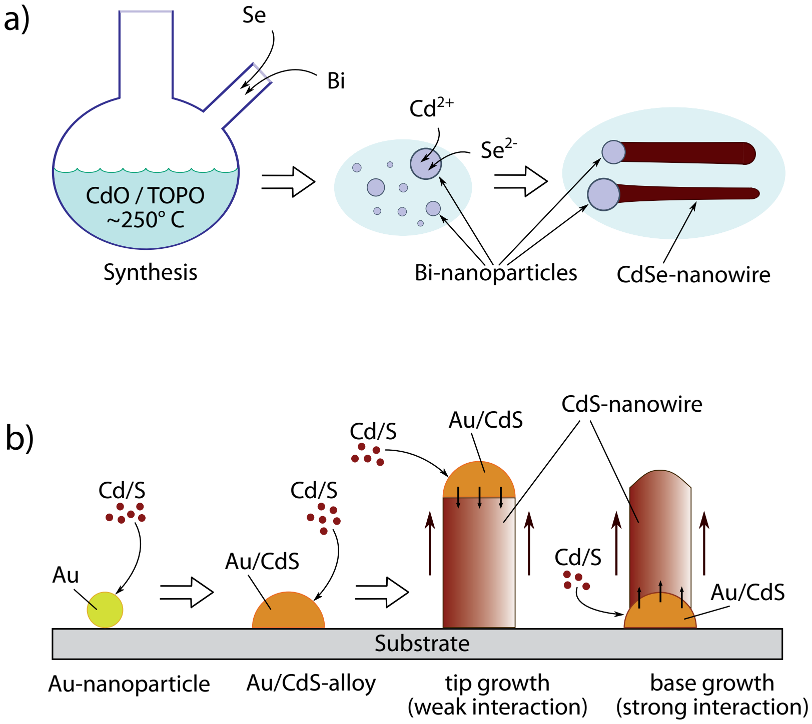

Figure 3.2: a) Wet-chemical synthesis of CdSe NWs: CdO- and Se-precursors dissolve in already molten Bi-NPs. They precipitate and a NW grows out of the bismuth. Competitive processes are the agglomeration of Bi and the growth of CdSe-NCs. b) CdS nanowires grow according to the same principle, but under different reaction conditions. Depending on the interaction between the catalyst particle and the substrate, either tip growth or base growth is achieved.

than SLS synthesis, a wider range of metal catalysts is available. The substrate is covered with gold nanoparticles and placed in a furnace. A metal-organic precursor is evaporated and decomposes at the catalyst particles. The elements form a Cd-S-Au alloy which melts at the reaction temperature. Again, upon saturation the CdS-NW starts to grow out of the gold particle[42].

Carbon Nanotubes The CNTs can also be grown by CVD. In this case, the substrate is dip-coated in a $FeCl_3$ solution. By adjusting the pH-value of the solution, different iron hydroxides are formed and adsorb to the substrate surface. The substrate is then annealed in a furnace, where iron oxide particles are formed. The oxide is reduced to iron under an Ar/H_2 atmosphere, followed by the introduction of a carbon precursor - typically acetylene or ethanol. Growth of the CNTs is interrupted, when gas supply stops, when the reaction temperature cools below a critical point, or when the catalyst particle is completely coated with an amorphous carbon layer, which stops supply of carbon material needed for structured growth[43,44].

3.2 Optical Setup

The main instrument for investigating nanostructures was a custom-built confocal microscope with electrical connections for optoelectronic measurements. An overview is shown in figure 3.3.

In confocal microscopy the excitation light is focused to a small spot. Parallel light from a laser is reflected from a beamsplitter onto the sample and is focused by the objective to a diffraction limited spot on the sample. There the light is either backscattered or excites fluorescence. The returning light passes the objective for a second time. Parallel light exits the infinity corrected objective and the beamsplitter, after which a lens focuses it on a slit or a pinhole. In a confocal arrangement, the sample and the detector are placed in conjugate planes so that only light coming from the focus of the objective will be focused on the detector.

For the excitation of nanostructures two different lasers were used: the Argon-Krypton laser is a modified version of the Coherent Innova 300 series (see also section). It offers a broad range of different narrow laser lines in the visible region with high output powers, necessary for Raman spectroscopy. The second laser is a Fianium Supercontinuum laser, which provides a continuous spectrum in the visible and near infra-red spectrum (figure 3.4b). As it is continuously tunable over the whole visible range, it can be used for light absorption spectroscopy.

Flipable laser line filters (F 1) are inserted to clean-up the beam from the Ar-Kr laser, as the main beam usually has several interfering neighboring bands of higher and lower energies. It is not possible to filter the light of the white laser other than with a monochromator, as described in section 3.2.2.

A shutter prevents the beam from illuminating the sample when no measurements are taking place. The light intensity is adjusted by an attenuator (At). Two absorbing wedges are moved against each other. They are aligned in such a manner that the second wedge corrects the beam displacement of the first. A combination of a $\lambda/2$- and $\lambda/4$-waveplate ensures circular polarized light (see also section 3.2.3).

Both beams pass several optical elements to tune the laser light. The pellicle beam splitter (PBS) diverts 8 % of the light on a compact pocket-spectrometer (USB2000+VIS-NIR Miniature Fiber Optic Spectrometer, Ocean Optics). It is thus possible to select any excitation wavelength without interfering with actual measurements. A cubic beamsplitter (CBS) directs 50 % of the light to the objective which is focused on the sample (S) inside the sample holder, a multi-axes piezometric nanopositioner (PI-500, Physik Instrumente GmbH). This can be moved laterally by 200 × 200 µm and vertically by up to 20 µm. A closed loop feedback ensures subnanometer precision. The sample holder has

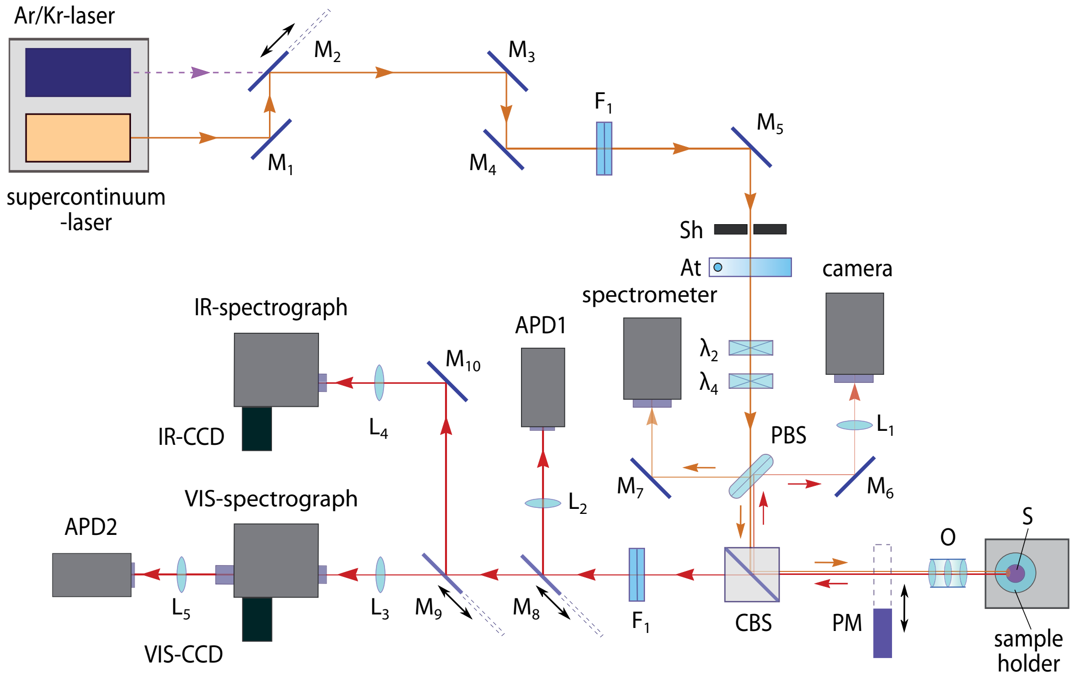

Figure 3.3: Overview of the home-built confocal microscope, used for optoelectrical measurements. M – mirror, F – filter, L – lens, Sh – motorized shutter, At – attenuator, PBS – pellicle beam splitter, CBS – cubic beam splitter, S – sample, λ_2 – half-wave plate, λ_4 – quarter-wave plate, PM – power meter, O – objective. For details, see text.

connections to an electrical transport rack to apply a drain and gate voltage and measure the current.

The objective is not only used to focus light on a region of interest but also to collect light reflected or emitted from the sample. Part of this light traces back to the camera, which lies in the plane conjugate to the sample. Thus the laser spot appears sharp on the camera only when it is focused on the sample.

The residual light is filtered with a notch or long pass filter to remove the reflected laser light. It passes the beam splitter cube and is directed to one of the spectrographs with a charge coupled device (CCD) camera, where the dispersed light is used to record spectra (VIS and IR). Alternatively, it can be sent to an avalanche photodiode (APD) for confocal imaging and recording timetraces. APD 1 collects all light coming from the sample, while APD 2 is located behind a spectrograph to collect light at specific wavelengths. This is especially useful when looking for distinct spectral features and high signal/noise suppression.

All instruments used were controlled by a home-written LabView program.

3.2.1 Argon-Krypton Laser

A laser is a coherent and powerful light source, suitable for investigations of nanostructures. The first gas laser was invented in 1960 by Ali Javan und William R. Bennett[45]. The basic components of a laser are an optical resonator, a pump source, and an optically active medium. For lasing an inversion of population of electronic states is necessary. This means that an electronic state with a higher energy is populated with more electrons than an electronic state with a lower energy. In the case of a gas laser, an electrical discharge is responsible for the population inversion. The resonator consists of plane-parallel highly reflecting mirrors. The reflectivity of one of the mirrors is slightly reduced to 98 % to 99 %, which allows part of the laser beam to exit from the cavity. The discharge tube is sealed with Brewster windows to minimize surface reflection losses and to select one particular light polarization. This laser was mostly used for Raman spectroscopy of carbon nanotubes, due to narrow line width. The four most extensively used lines were 488 nm (Ar), 514 nm (Ar), 568 nm (Kr) and 647 nm (Kr). The relative power of the lines is given in tables 3.1 and 3.2 for a new tube[46]. Yet it should be kept in mind that the color balance (relative intensity of these wavelengths) may shift with the tube's age.

λ / nm	E / eV	rel. intensity
457.9	2.71	0.07
476.5	2.60	0.12
488.0	**2.54**	**0.375**
496.5	2.50	0.12
501.7	2.47	0.07
514.5	**2.41**	**0.45**

Table 3.1: Most important laser lines of the Ar-laser in the visible range in nm and eV and their relative intensities

λ / nm	E / eV	rel. intensity
413.1	3.00	0.06
530.9	2.33	0.05
568.2	**2.18**	**0.04**
647.1	**1.91**	**0.10**
676.4	1.83	0.03
752.5	1.65	0.04

Table 3.2: Most important laser lines of the Kr-laser in the visible range in nm and eV and their relative intensities

3.2.2 Supercontinuum Laser

A supercontinuum laser, or white light laser, emits light of broad spectral bandwidth that covers the whole visible electromagnetic spectrum and extends well into the near IR, spanning nearly two octaves in the wavelength domain - from 450 nm to 1600 nm. The supercontinuum is achieved by utilizing several non-linear effects, such as self-phase modulation, Raman scattering and four wave mixing, most important of which is the Kerr effect: When light of high intensity propagates through a crystal, non-linear polarization leads to a change in the refractive index. For normal group dispersion the Kerr and dispersive terms lead to a dispersion of the pulse, consequently the peak intensity drops. Anomalous group velocity counteracts these effects of group-velocity dispersion (GVD) and Kerr nonlinearity and pulses can propagate through the fiber as solitons without dispersing. It should be noted, however, that details of most of the physical processes happening inside the fiber are not understood so far.

The pump laser is a Q-switched InGaAs/GaAs laser, emitting at 1060 nm. Broad spectra are reached when the pump wavelength is close to the zero dispersion wavelength (ZDW). Bulk silica has a ZDW of 1270 nm. By removing most of the cladding, as shown in figure 3.4, an array of hexagonal close-packed air-filled holes is formed and the ZDW is shifted towards the desired wavelength. This fiber confines light within the core in a single transverse mode[47]. The laser (SC450-PP, Fianium) used in the performed experiments employs a Yb-doped optical fiber for SC generation and generates 6 ps pulses at a frequency of 30 MHz. The spectral broadening with higher power of the pump laser is shown in figure 3.4b.

A simple monochromator, built to select the excitation wavelength from the supercontinuum white laser is shown in figure 3.5. Parallel white light exits the optical fiber (OF) through the laser head (LH). This light is dispersed by a prism (P) and parallelized by a 2″ lens (L). An adjustable slit (S) and a mirror (M) are mounted on a movable platform to select a certain wavelength[48]. As the mirror is slightly tilted upwards, the reflected beam is also shifted and can exit the box through a decoupling mirror (DM).

The supercontinuum laser was only used for PL measurement, since the selected excitation wavelength was comparatively broad and the emitted power is smeared over a wide electromagnetic range.

3.2.3 Beam Formation

The laser beam is focused, modified and shaped by lenses and other optical elements. The most important of them will be discussed here.

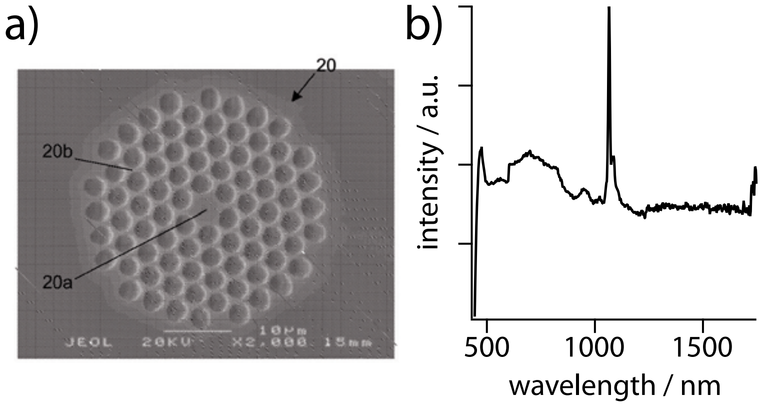

Figure 3.4: a) Cross-section of the optical fibre. Most of the cladding has been removed[47]. b) Emission spectrum of the Fianium laser at full power. The cut-off wavelength of around 450 nm and the pump laser emission (1060 nm) are clearly visible.

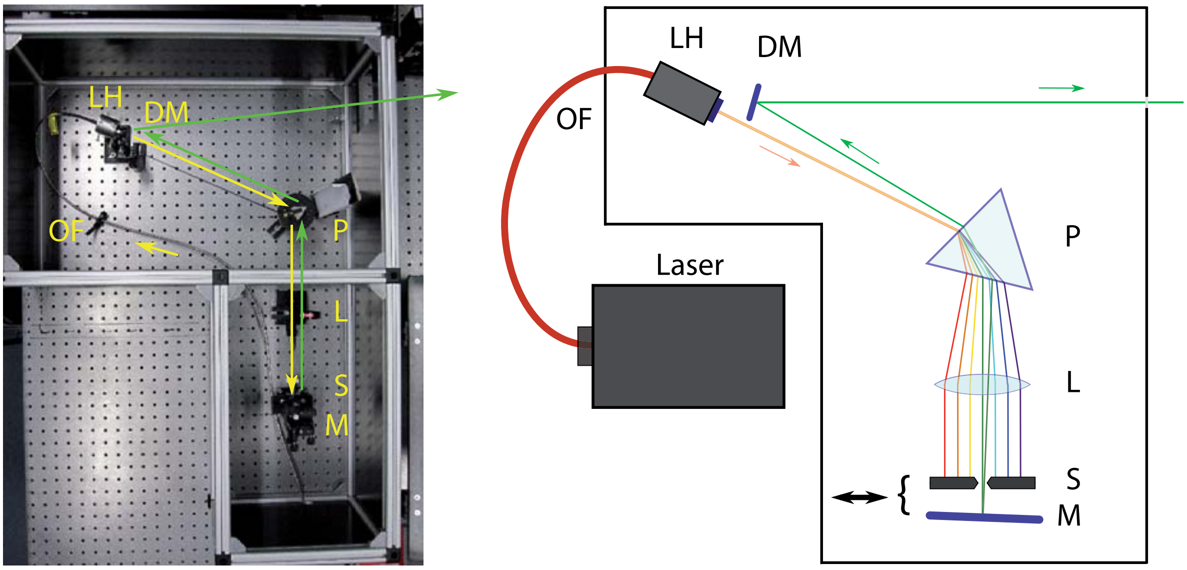

Figure 3.5: Simple monochromator, built to select the excitation wavelength from the supercontinuum white laser. OF - optical fibre; LH - laser head; DM - decoupling mirror; P - prism; L - lens; S - slit; M - mirror.

Various optical filters are used in the setup (figure 3.6). The laser line filter is a very narrow bandpass filter which removes spectral lines of the plasma from the Ar-Kr laser, but also neighboring laser lines. The long pass filter has a steep cutting profile. Thus it is possible to measure Raman peaks very close to the excitation wavelength (e.g. radial breathing modes (RBMs) of CNTs). A Notch filter, on the other hand, has the advantage of blocking just the respective wavelength whereas light of both higher and lower energy can pass, which is desirable for Stokes and anti-Stokes Raman lines.

For homogenous excitation circular polarized light was used. This was realized through a combination of a half- and a quarter-waveplate. These are

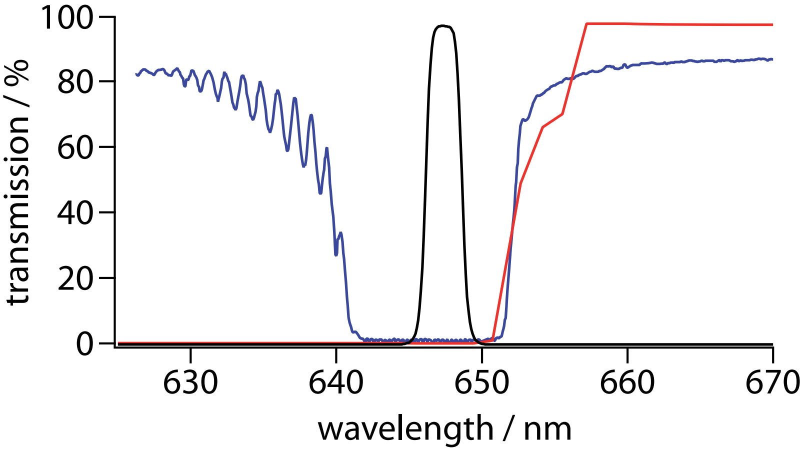

Figure 3.6: Transmission profiles of different types of filters for 647.1 nm. A laser line filter lets through light of only a particular wavelength (black), a longpass filter blocks light with energies above the laser wavelength (red), whereas a notch filter cuts out the a region around the laser wavelength (blue).

made from a birefrigent crystal (MgF_2). Along the fast axis polarized light travels through the crystal with a different speed than along the slow axis, thus creating a phase shift. The phase can be described as

$$\Gamma = \frac{2\pi \Delta n L}{\lambda_0}\,, \tag{3.1}$$

with Δn being the difference of the refractive indexes of the ordinary and extraordinary axes and L being the thickness of the crystal. A $\lambda/4$ plate shifts the phase by a quarter-wavelength and linear polarized light is changed into circular polarized light and vice versa. A $\lambda/2$-plate leads to a rotation of the polarized light. Combination of both can form linear, elliptical and circular light to compensate for the influences of all optical components.

The polarization was measured in front of the objective with a powermeter and a polarizer. The circular polarization was regarded as satisfactory when the condition $1 < I_{max}/I_{min} < 1.2$ was fulfilled.

3.2.4 Microscope

A microscope objective with a high numerical aperture focuses the laser beam on the sample. Two different objectives were used: when possible, an Epiplan-Apochromat objective with a 150× magnification and a working distance of 230 µm. The other, an LD Epiplan objective with a magnification of 50× has a long working distance of 7 mm and was therefore used for bonded samples

objective	Epiplan Apochromate	LD Epiplan
magnification	150×	50×
NA	0.95	0.5
α	72°	30°
η_{geo}	34 %	7 %
η_{trans}	∼ 90 % to 95 %	95 % to 98 %
w_0 (488 nm)	256 nm	488 nm
w_0 (647 nm)	341 nm	647 nm
f	1.645 mm	1.645 mm
AA	0.23 mm	7.0 mm
EA	3.5 mm	3.5 mm

Table 3.3: Parameters of the used objectives. NA is the numerical aperture, α is the semiangle of the collected light, η_{geo} is the geometrical collection efficiency, η_{trans} is the transmission of the objective, w_0 is the FWHM of the minimum spot size, f is the effectve focal length, AA is the working distance and EA the entrance aperture of the objective.

which were embedded in a chip carrier. Characteristics of both objectives are given in table 3.3.

The performance of a microscope is characterized by its resolution power, i.e. the minimum distance between two illuminated objects at which they can still be distinguished as two separate entities. Due to the wavelike nature of light the resolution is limited by diffraction, where the propagating wavefront is acts as an emitter of secondary wavelets which can interfere with each other. This leads to the formation of concentric rings (Airy pattern) which can be described by the Bessel function:

$$I(x) = I_0 \left[\frac{2J_1(x)}{x}\right]^2 , \tag{3.2}$$

where $J_1(x) = x \sum\limits_{n=1}^{\infty} (-1)^{n+1} \frac{x^{2n-2}}{(n-1)!n!2^{2n-1}}$, with $x = (\frac{\pi d}{\lambda}) \sin\theta$. The majority (83.8 %) of the light intensity is concentrated in the central disk . The subsequent rings contribute 7.2 %, 2.8 %, 1.5 % and 1.0 %. For practical reasons the Airy profile is often approximated with a Gaussian function:

$$I = I_0 \exp\left[-(4\ln 2)\frac{r^2}{w^2}\right] , \tag{3.3}$$

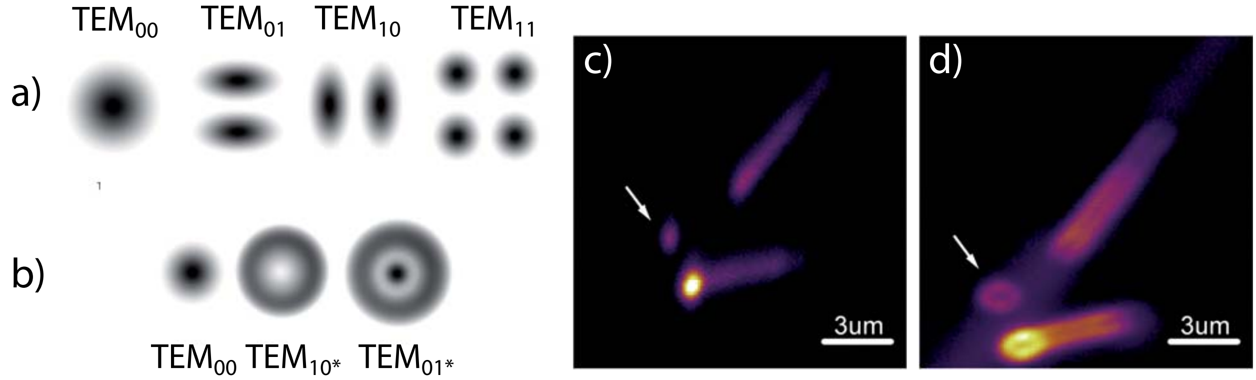

Figure 3.7: a) Low-order Hermite-Gaussian resonator modes; b) low-order asymmetric resonator modes; c) a CdS-nanowire measured with TEM_{00}; d) same wire measured with TEM_{01*}, the same position is marked with an arrow.

where ω is the half-width-half-maximum of the Gaussian bell curve. The Gaussian approximation is only valid for the fundamental order of the transverse mode of the laser beam which leaves the resonator cavity. However, modes of higher order might also be emitted and decrease the image quality significantly. They can be described as Hermite Gaussians (figure 3.7 a) and Laguerre Gaussians (fig. 3.7 b). For comparison, images of a confocal scan with a TEM_{00} (figure 3.7 a) and a TEM_{01*} (figure 3.7 a) are shown.

If the laser operates in a TEM_{00} mode and best optical components are used, the highest resolution obtainable is

$$d_0 = 0.6098 \frac{\lambda}{NA} \, . \tag{3.4}$$

At this distance the maximum intensity of one object coincides with the minimum of the second object (Rayleigh criterion). In the case of confocal microscopy the resolution can be further improved by a factor of $\sqrt{2}$:

$$d_{0,\mathrm{conf}} = 0.4312 \frac{\lambda}{NA} \, . \tag{3.5}$$

NA is the numerical aperture of the objective, given by:

$$NA = n \sin \alpha \, , \tag{3.6}$$

where n is the diffraction index of the medium between the lens and the substrate (typically air) and α the semiangle of the focused light beam.

The laser intensity measured directly in front of the objective with a power meter can be converted into the intensity on the sample by:

$$I_0 = \frac{2P_{max}}{\pi w_0^2} \approx \frac{2 \times 0.95 P_{sample}}{\pi w_0^2} \tag{3.7}$$

$$I_0 / P_{max} = 6 \cdot 10^{+8} \mathrm{cm}^2 \qquad \text{for the Apochromate objective, 150x} \tag{3.8}$$

$$I_0 / P_{max} = 3 \cdot 10^{+8} \mathrm{cm}^2 \qquad \text{for the LD Epiplan objective, 50x} \tag{3.9}$$

3.2.5 Detection Path

The signal, emitted from the sample, is collected by the microscope objective and is directed to the detection part of the setup. It consists of two APDs and two CCDs with their respective spectrographs. Usually a long pass, notch or optical density (OD) filter is used to reduce the laser light to an acceptable level.

Avalanche Photodiode The APDs are used as point detectors for confocal measurements. The first APD, APD 1, can detect all light emitted and reflected from the sample. APD 2 is installed behind a spectrograph, which is used as a monochromator and acquires light only of a specific energy. The active part of an APD is a semiconductor p-n junction, a "pixel" of 175 µm size for the APDs used[49]. The absorption of a photon with an energy higher than the band gap creates an electron-hole pair in the silicon layer. Both charges are accelerated with a high reverse bias of 100 V to 200 V. When the electron gains enough kinetic energy before being scattered it can create another electron-hole pair through ionization, which in turn leads to an avalanche (figure 3.8a)[50]. Most commonly used materials are silicon, germanium and InGaAs. Figure 3.8b shows their respective quantum efficiencies for different wavelengths in comparison to a photomultiplier tube (PMT).

Spectrograph The light is focused by a lens on the entrance slit of the spectrograph. This slit functions as a pinhole to block ambient light and defines the confocal plane of the microscope. The light is diverted by a collimating mirror on a turret with two different gratings and a mirror. The grating disperses the light by diffraction and reflects it on to the second collimating mirror (figure 3.9). Constructive interference occurs when the grating equation is fulfilled:

$$m \cdot \lambda = d(\sin\alpha + \sin\beta)\ , \tag{3.10}$$

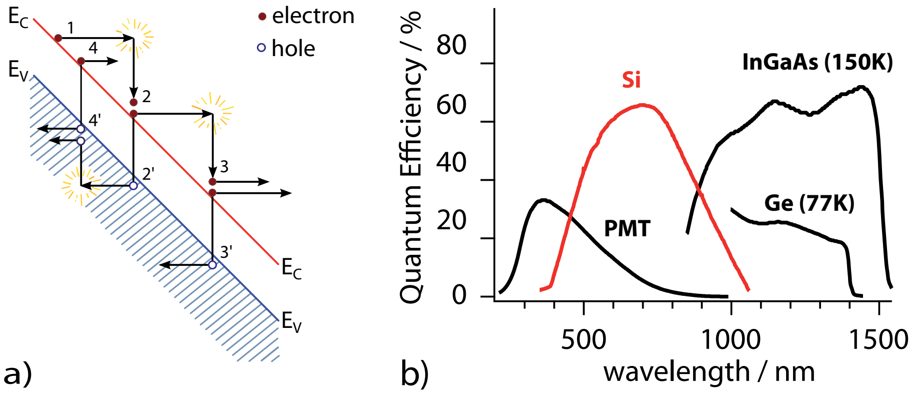

Figure 3.8: a) Working principle of an APD: Charges are accelerated in an electric field and lead to an avalanche of electrons/holes. b) Quantum efficiency of an APD for different materials and a photomultiplier tube (adapted from [49,50]).

where m is an integer. When $m = 0$, the incident angle and the reflected angle are the same, i.e., the grating functions as a mirror (0^{th} order of diffraction).

For light of a particular wavelength, the maxima occur at a specific angle β according to the rearrangement of equation 3.10:

$$\beta = \arcsin\left(\frac{m \cdot \lambda}{d} - \sin\alpha\ .\right) \tag{3.11}$$

Usually, the dispersion power of the grating is given by the groove density $G = 1/d$, with the units "number of grooves per mm". This leads to the dispersion relation:

$$G \cdot m \cdot \lambda = \sin\alpha + \sin\beta\ . \tag{3.12}$$

The angular dispersion D_{ang} is the spectral range per unit angle and is obtained by differentiating equation 3.10:

$$D_{ang} = \frac{\partial\beta}{\partial\lambda} = \frac{m}{d\cos\beta} = \frac{m}{d}\sec\beta = G \cdot m \cdot \sec\beta\ . \tag{3.13}$$

The effective length of the spectrograph has also to be taken into account, resulting in the linear dispersion D_{lin}:

$$D_{lin} = D_{ang} \cdot l = G \cdot m \cdot l \cdot \sec\beta\ . \tag{3.14}$$

The grating has a sawtooth-like structure with a characteristic angle (blaze angle). This is an important characteristic of a grating, as it determines at which wavelength the grating will be most efficient. This is achieved by forming right angles with a specified blaze angle, measuring the angular distance to the

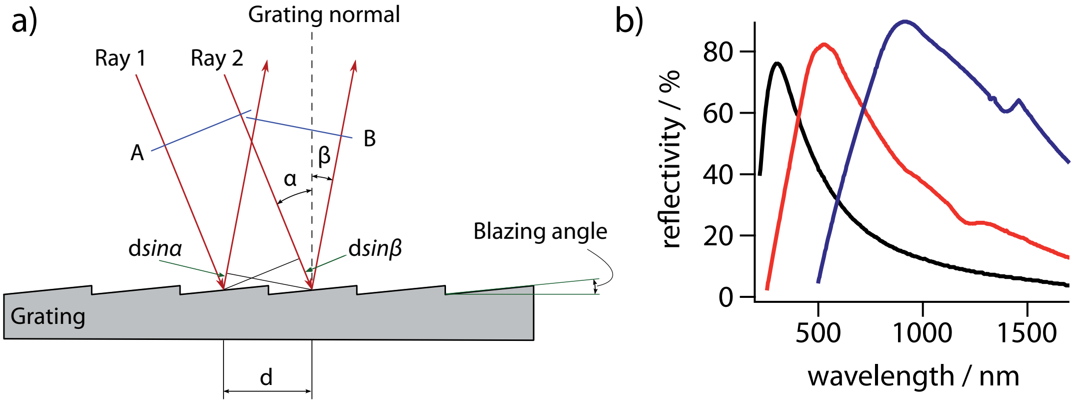

Figure 3.9: a) Diffraction process on a grating. b) Reflectivity of gratings with different blazing wavelength: black - 200 nm, red - 500 nm and blue - 1000 nm.

normal of the blazed surface. Figure 3.9b shows the influence of different blaze angles.

Charge Coupled Device A CCD with a silicon chip with a pixel matrix is used as a multi-channel detector at the output of the spectrometer (figure 3.10). A thin isolating layer (0.1 µm to 0.15 µm) is deposited on a semiconducting support, which in turn is covered with an array of electrodes. This forms a metal-oxide-semiconductor capacitance. When a positive bias is applied, major change carriers (holes) are quickly removed from the semiconductor surface. This results in a depletion layer with a thickness of around one micron. Minor carriers (electrons) generated in the depletion layer (thermally or by diffusion) move to the semiconductor-insulator interface under the influence of the electric field and localize in the narrow inversion layer. In this way, a potential well for electrons is created.

When the CCD is illuminated, photons generate electron-hole pairs. The holes are "ejected" into the neutral part of the semiconductor, while electrons are accumulated in the pixel with their number proportional to the number of photons.

After exposure, the charge is transferred row by row. This is done by increasing the potential on an adjacent electrode and by reducing that of the first electrode. When the electrons reach the shift register they are "emptied" sequentially into the output node (figure 3.10c). Only after all pixels from the first row have been digitized, the second row can be moved into the shift register. As soon as the pixel has been emptied, it is available for the next measurement.

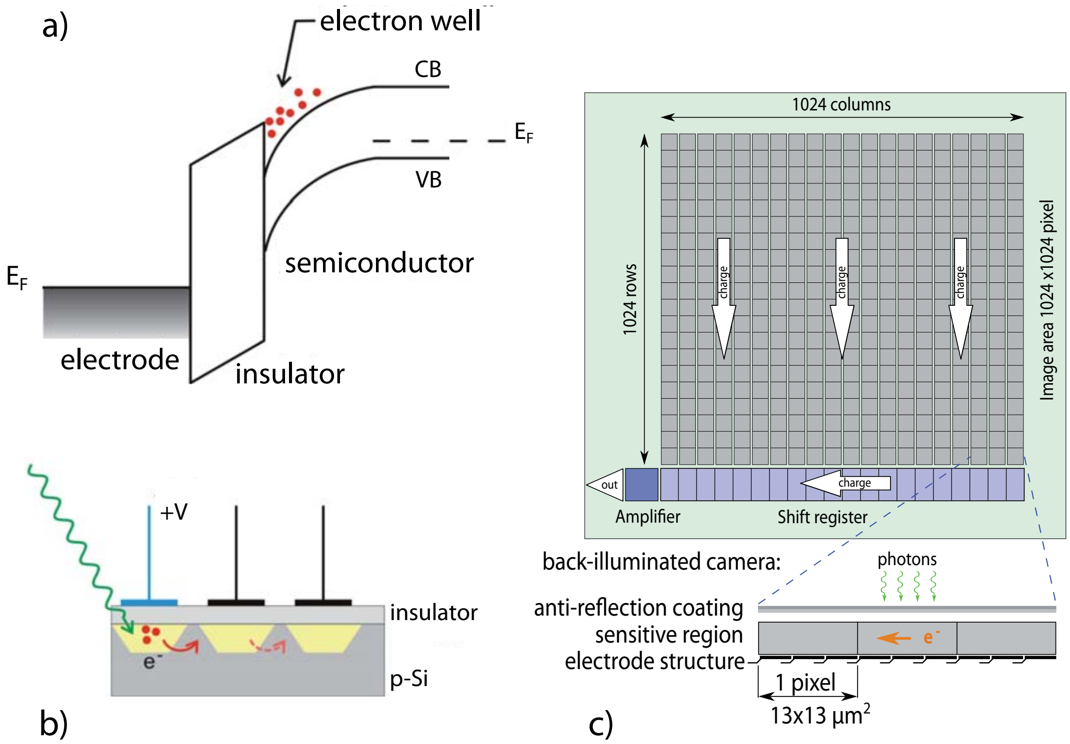

Figure 3.10: Working principle of a CCD camera: a) electrons are accumulated due to a positively charged electrode, b) which are transferred from pixel to pixel, c) the signal is read out sequentially from the shift register through the output node.

Electron Bombarded CCD Conventional CCDs based on silicon cannot be used for IR light detection since the energy is not sufficient to excite an electron into the conduction band. In this case, an Electron Bombarded Charge Coupled Device (EBCCD) is used. Incident photons cause electron emission due to the photovoltaic effect. The electrons are accelerated by a high voltage (HV) gradient (few kV) and directly hit a (back-thinned) CCD (figure 3.11). The advantages of a EBCCD are additional gain and a fast read-out speed [51]. Gating of the HV can reduce the noise to a minimum. However, the dynamic range is limited. Since a photoelectron generates around 300 e-h pairs, the potential well is also filled 300 times faster. Thus a pixel is filled with a few hundred photons.

The CCD chip used in this work is of the "back-illuminated" type, i.e., the silicon wafer is thinned down to 10-20µm and the electrodes which create the potential well are placed at the back, thus avoiding absorption of the emitted light. To reduce dark noise, the camera was cooled down to $-55\,^{\circ}$C and the spectra were acquired in spectroscopy mode, in which the relevant vertical pixels were binned to a 1024×1 line.

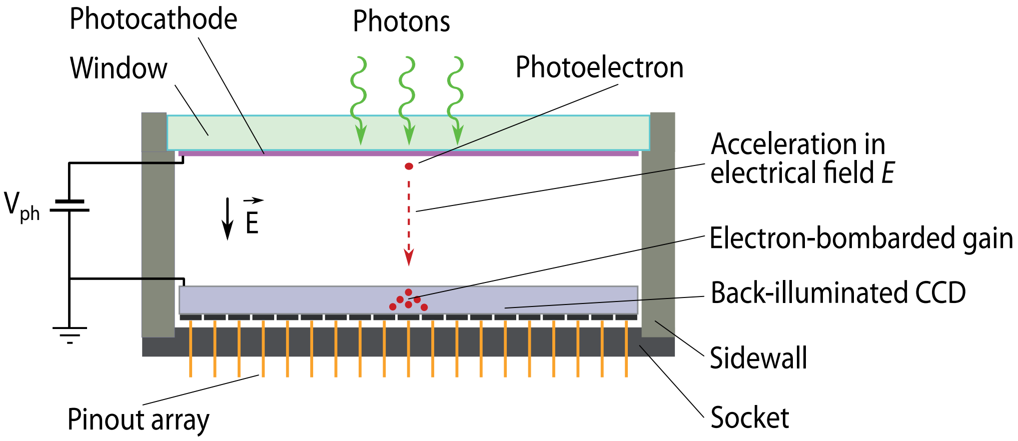

Figure 3.11: Scheme of an electron bombarded CCD, used for IR light detection: Incident photons knock out electrons, which are accelerated in an electric field. These, in turn, can be detected via a CCD.

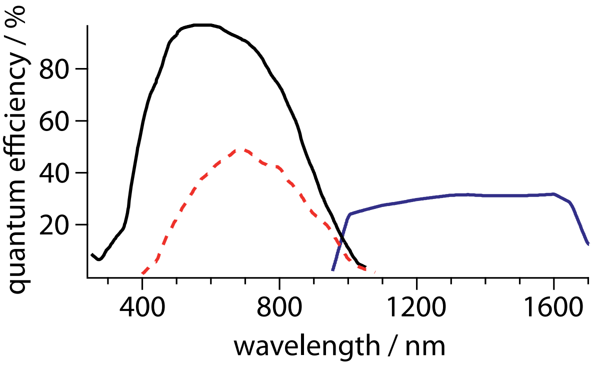

Figure 3.12: Quantum efficiency of a VIS and IR-CCD camera. Black - front-illuminated CCD, red - back-illuminated CCD and blue - electron bombarded CCD (EBCCD), which is used in the infra-red.

Noise The noise obscuring the signal in a CCD can be divided into three different types: read-out noise, signal shot noise and dark current shot noise. The read-out noise is introduced during the readout and arises mainly from the on-chip preamplifier. The signal noise refers to the inherent natural variation of the incident photon flux. The number of photo-generated carriers collected in a potential well in a time t is therefore a random variable. The standard deviation of this random variable is the photon noise. The dark noise results from the dark current. It arises from the thermal generation of minority carriers that takes place in every semiconductor. Dark current is the rate of generation of the thermal electrons, and the dark noise, which also follows a Poisson relationship, is the square root of the number of the thermal electrons generated within a given exposure.

3.3 Electrical Measurements

3.3.1 Lithography

For electrical measurements it is necessary to contact individual nanostructures. This is usually done with optical lithography. Thereby the substrate is coated with a light-sensitive organic film and a mask with a defined pattern is placed on top. Then the substrate is illuminated with UV light, thus modifying the coating. For example, diazonaphthoquinone (DNQ) releases N_2 upon illumination, which changes its polarity. Exposed regions can therefore be dissolved faster in aqueous solutions. These substances are called positive resists. In negative photoresists, such as SU-8, illumination decreases solubility and these structures remain after development.

Usually, conventional optical lithography is sufficient to produce microscopic devices. For higher resolution, however, the photoresist can be illuminated by a focused electron beam in a scanning electron microscopy (SEM). This method offers a much higher resolution of only a few 10 nm. Yet, only sub-micrometer structures and pre-selected nanoparticles are contacted by e-beam lithography due to much higher effort. The procedure is shown in detail in 3.13.

Lithography with a negative photoresist was conducted as follows:

- A NW-coated silicon wafer was spin-coated at 3000 RPM for 10 seconds with 10 µL of AZ-nLOF 2000.
- After application of the light-sensitive polymer, the silicon wafer was soft-baked for 8 min at 100 °C.
- The optical mask was applied on the silicon wafer, weighted with a glass panel and exposed to UV light for the duration of 60 s.

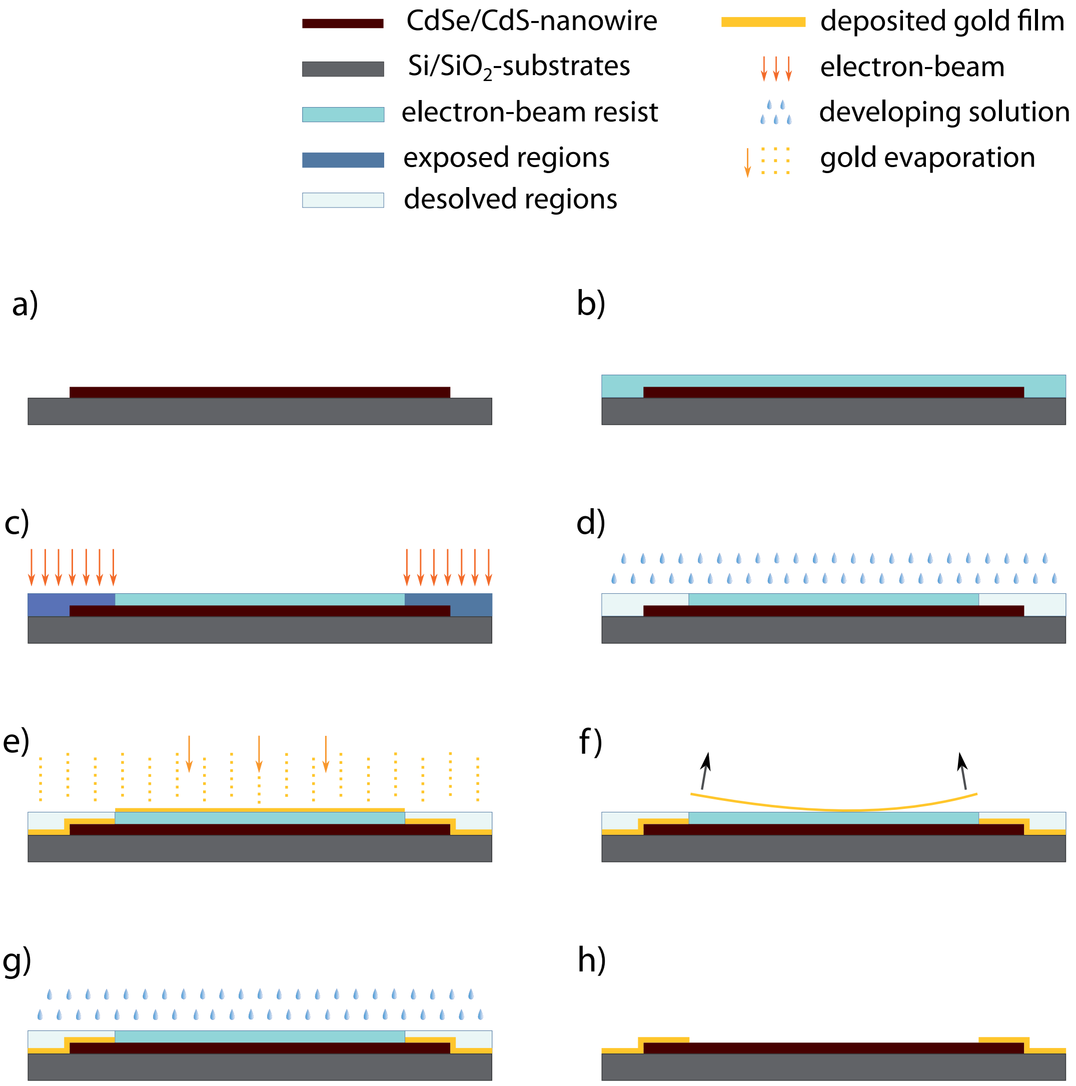

Figure 3.13: Lithographic steps (for details see text).

- Subsequent, post exposure baking was performed for 2 min at 110 °C.
- Unexposed areas were removed by development in tetramethylammonium hydroxide (25 %, w/v) for 20 s to 120 s.
- The silicon wafer was carefully rinsed with DI water.

Afterward, the sample was ready for electrical measurements.

3.3.2 Electrical Characterization

The sample was glued with a conductive silver/resin mixture to the chip frame which, in turn, was inserted into a sample holder. Electrical connections led out of the sample holder to a transport rack where BNC cables were connected to the AdWin control box. The AdWin controller can apply voltages between $-10\,\mathrm{V}$ and $+10\,\mathrm{V}$, in steps of 305 µV.

The bias was applied at the drain, while the source was grounded. Current flowing through the sample I_{ds} was measured at the source with an *I-U* converter and amplifier (DLPCA-200, FEMTO Messtechnik GmbH), with a variable gain of up to 1×10^{11}. Another output of the AdWin controller was used to apply a bias at the bottom of the n-doped silicon substrate (figure 3.14). This allows to measure nanodevices in a field effect transistor (FET) configuration. All measurements were performed in a two-probe setup, i.e. the measured resistance is a combination of the intrinsic resistance of the nanostructure as well as the contact resistance.

For non-standard samples a new sample-holder was developed (figure 3.15) which allows to use larger substrates and a closer approach with the microscope objective. The contacts were provided by a SIM-card holder of a mobile phone.

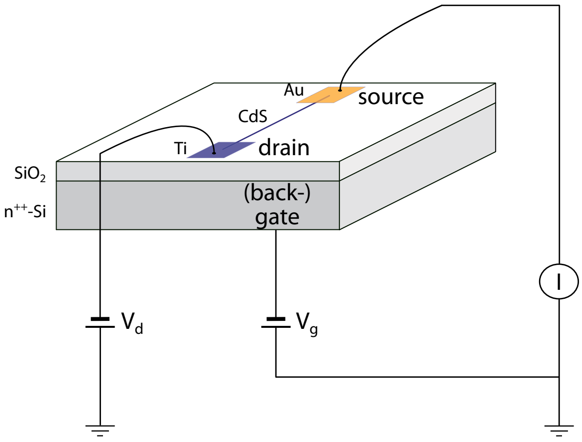

Figure 3.14: Connections of source, drain and gate for electrical measurements.

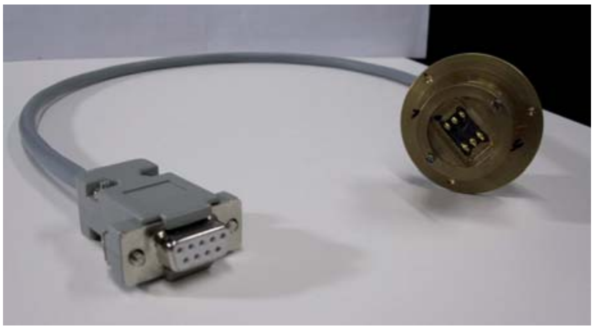

Figure 3.15: Custom sample holder for non-standardized samples.

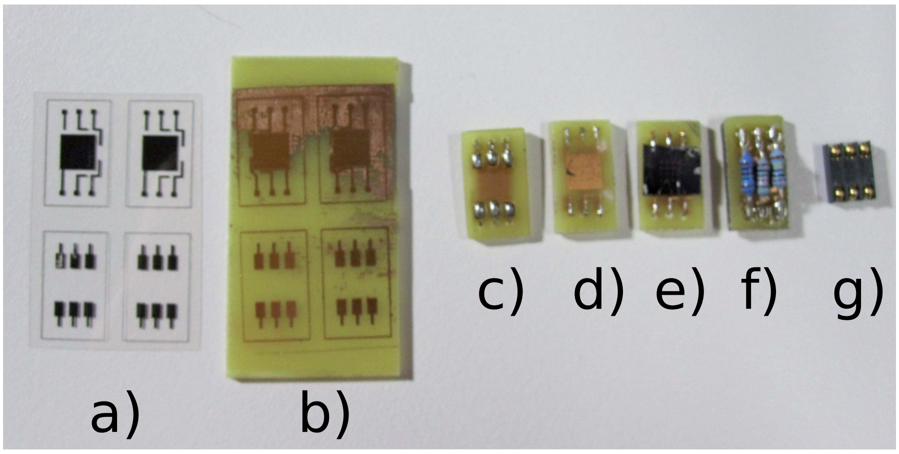

Figure 3.16: a) printed mask; b) partially developed circuit board; c) back of the chip carrier; d) front of the chip carrier; e) bonded substrate; f) chip carrier with test resistances; g) built-in SIM-card holder.

The chip carriers were prepared by conventional photolithography with printed masks as described in section 3.3.1. Afterwards, they were cut-out, drilled and soldered. Figure 3.16 shows the individual steps: 3.16a – the printed mask, which has to be applied at both sides of the circuit board; 3.16b a partially developed circuit board; 3.16c and 3.16d show the back and the front of the finished carrier. A bonded subtrate is shown in 3.16e and a test carrier with different resistances (10 kΩ to 1 MΩ) in 3.16f. The built-in SIM-card holder can be seen in 3.16g.

Scanning Photocurrent Microscopy (SPCM) is a convenient tool to investigate changes in band structure (such as Schottky barriers) along a contacted object. Hereby the drain current is measured as a function of the x-y position of the focused laser spot (figure 3.17). Either the reflected light, or the PL is recorded at the same time, to correlate the photoresponse with a particular position within the devices. Two different types of SPCM measurements were carried out in this work, namely with zero drain-source bias ($V_{ds} = 0\,\mathrm{V}$) and under

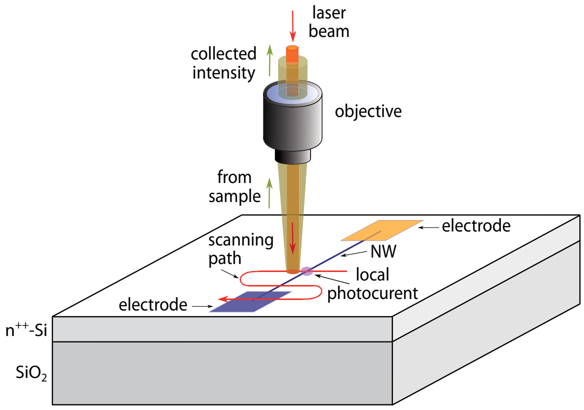

Figure 3.17: Principle of scanning photocurrent microscopy

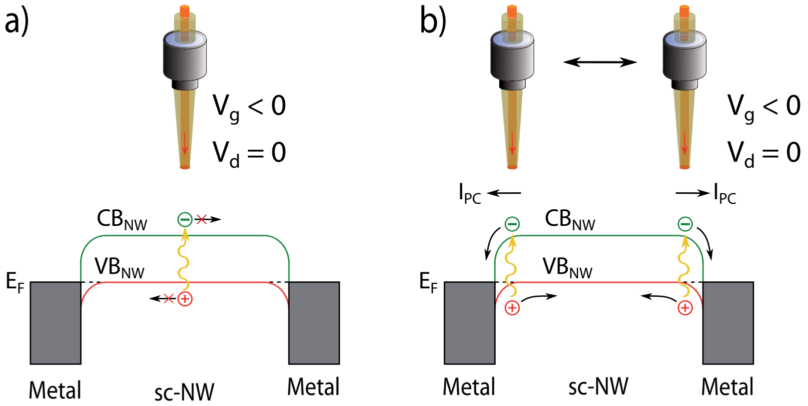

Figure 3.18: Principle of scanning photocurrent microscopy: a) If the laser illuminates the NW far away from the contacts, no current is observed. b) When the laser illuminates the wire in the proximity of the electrodes, the charges can reach the metal electrode and contribute to a measurable current.

applied drain-source bias. All measurements were performed under ambient conditions.

When a semiconductor is contacted with two metals (MSM structure), a charge transfer between the metal and the semiconductor re-equilibrates the Fermi levels of the materials according to their work functions, as described in section 2.3.1. This process leads to the formation of Schottky barriers at the contact point, which in turn lead to a photoconductivity response.

When the semiconductor is illuminated, as shown in figure 3.18, electron-hole pairs are generated in the valence and the conduction bands. If the laser illuminates the NW far away from the contacts (figure 3.18a), no current is observed. On the contrary, when the laser illuminates the wire in the proximity of the electrodes (figure 3.18b), the charges can reach the metal electrode and contribute to a measurable current. Changes in the band structure within the wire can be visualized in a similar manner with applied bias.

3.4 Additional Measurements

3.4.1 Atomic Force Microscopy

The basic idea of an AFM is shown in figure 3.19. It consists of a cantilever with a sharp tip, which is moved by piezo-electric elements. When the tip comes into proximity of the surface, interaction between the tip and the sample leads to a deflection of the cantilever. This is measured using a laser beam, which is reflected from the back of the cantilever to a photodetector made of four closely packed photodiodes. If the cantilever encounters a change in height while scanning in x- and y-direction, either the deflection of the cantilever is converted into a height information or the initial interaction force is restored by approaching or retracting the substrate. Three different modes can be distinguished: in the contact mode, the tip is brought down on the substrate and dragged along the surface. The deflection is used as a feedback signal, while the force between the tip and the surface is kept constant during scanning (figure 3.19). While this mode gives the best resolution for small structures, the tip is also easily contaminated and damaged by sudden changes in height. In intermittent contact mode, the cantilever is oscillated by a small piezoelectric element at or close to its fundamental resonance frequency (usually 200-400kHz). The amplitude of the oscillation is typically 100 to 200 nm. The oscillation amplitude, phase and resonance frequency are changed by the tip-to-sample interaction forces (van-der-Waals forces, dipole-dipole interactions, etc.). These modulations in oscillation with respect to the external reference oscillation give information about the sample's topography. A tapping AFM image is therefore produced by imaging the force of the oscillating contacts of the tip with the sample surface and not just by dragging the cantilever across the surface, such reducing the risk of surface damages. In the non-contact mode the tip is oscillated at a frequency slightly above its resonant frequency. In this case, long range forces decrease the resonance frequency of the cantilever. Sample and tip do not suffer from degradation but from the adsorbed water layer which is present under ambient conditions. This makes the realization of this method rather difficult.

The AFM was routinely operated in "intermittent contact" mode, mainly for localizing nanowires and tubes on the substrate and to determine their diameter. AFM images were taken with a DI Nanoscope III and a JPK Nanowizard II.

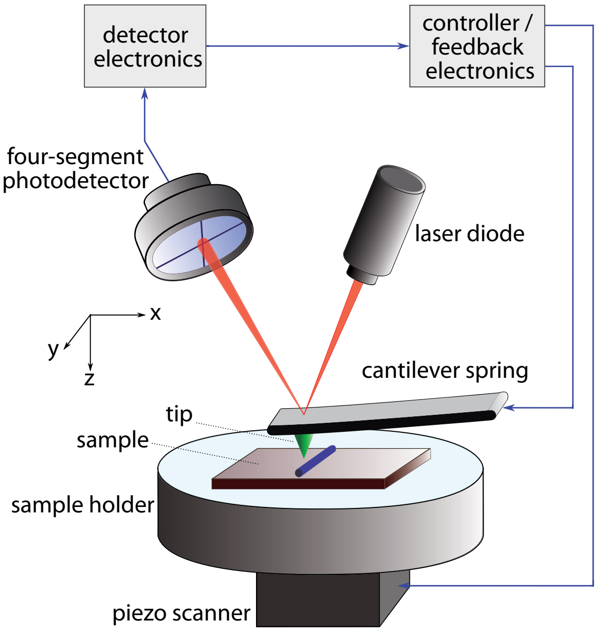

Figure 3.19: Sketch of the working principle of an atomic force microscope: A laser beam is reflected from the cantilever to a detector to determine the height of the structures on the sample.

3.4.2 Transmission Electron Microscopy

As discussed in section 3.2.3, the resolution of a given microscope is limited by the wavelength of the light used. To significantly improve the resolution it is possible to use electrons instead of photons, which can be easily accelerated in an electric field. Their wavelength λ_e is given by the de Broglie relationship:

$$\lambda_e = \frac{h}{p} \,. \tag{3.15}$$

Accounting for relativistic effects this results in

$$\lambda_{e,rel} = \frac{h}{\sqrt{2m_0E(1+\frac{E}{2m_0c^2})}} \,, \tag{3.16}$$

with the Planck's constant h, the rest mass of the electron m_0, the momentum p of the accelerated electron and its energy E. The first electron microscope was realized in 1932 by M. Knoll and E. Ruska[52].

The most important parts of a TEM are shown in figure 3.20 and are outlined in the following[53].

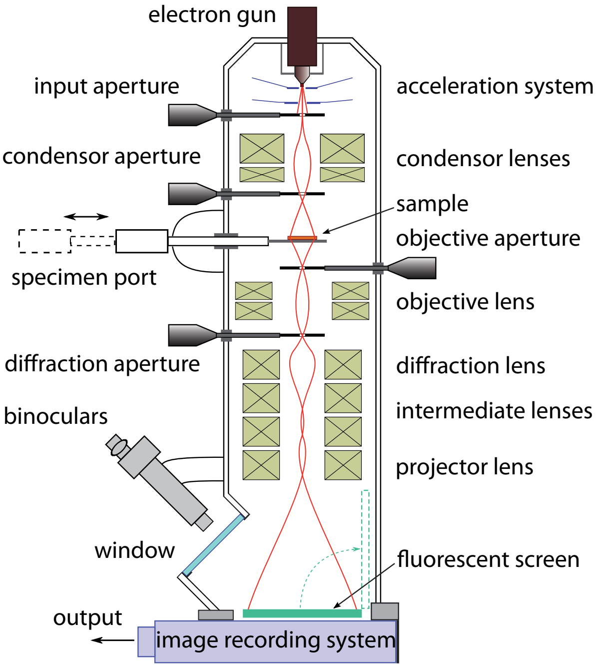

Figure 3.20: Sketch of the basic elements of a TEM, for details see text

The electron gun is a thin tungsten needle with a tip radius $< 0.1\,\mu\text{m}$. The underlying principle is that electric field strength is considerably increased at sharp points, in accordance with

$$E = \frac{V}{r} \; . \tag{3.17}$$

The quality of the emitted beam can be characterized by three parameters: brightness, coherency and stability.

The brightness β is defined as

$$\beta = \frac{4 i_e}{(\pi d_0 \alpha_0)^2} \; , \tag{3.18}$$

with i_e as the cathode emission current, d_0 the diameter of the electron source and α_0 the semiangle, at which electrons diverge from the source.

The coherency describes how well the electron waves are “in step” with each other. The coherence wavelength is defined as

$$\lambda_c = \frac{vh}{\Delta E} \quad , \tag{3.19}$$

where v is the electron velocity and ΔE the energy spread of the beam.

Finally, the high voltage supply and the electron current from the source have to be minimized to reduce variation in the exposed images. For cold field emission it is possible to keep the stability between 1 % to 5 %. Stability improves with ultra high vacuum (UHV) conditions.

Similar to light in an optical microscope, the electron beam needs to be focused and aligned. This is done by magnetic lenses made of soft iron. Each polepiece is wrapped by a copper wire. When a current passes through the coil, a magnetic field is created in the aperture. The field is inhomogeneous along the length of the lens, but axially symmetric. It can be derived from classical electromagnetic theory that the electrons follow a helical trajectory through the lens field.

For high resolution images, several distortion effects have to be taken into account. The spherical abberation leads to a surrounding halo for each point object P in the Gaussian image plane. Chromatic abberation originates from variation in the electron energy (and wavelength) created in the specimen and can be reduced by using thinner samples. Astigmatism results from electrons in a non-uniform magnetic field, originating from imperfections in the polepiece. These effects lead to a blurring of the image. If all abberations could to be compensated, the theoretical resolution limit, as in equation 3.4, could be reached.

Unless specified otherwise, all TEM images were taken with a *Jeol JEM-1011* at an acceleration voltage of 100 kV on silicon nitride membranes and HRTEM images were taken using a *JEOL JEM 2200 FS (UHR)* with CESCOR and CETCOR corrector at an acceleration voltage of 200 kV on a copper grid with a carbon film.

4 Diameter scaling of the optical band gap in individual CdSe Nanowires

This chapter can be divided into two parts. The first part presents a detailed optical and structural characterization of individual NWs. With a combination of atomic force microscopy, scanning fluorescence microscopy, and transmission electron microscopy the diameter dependence of the optical band gap of single CdSe NWs was investigated. Experimental results are compared with calculations within the effective mass approximation and other theoretical approaches. The second part describes the characterization of a heterojunction metal-semiconductor system with two promising nanomaterials: CdSe and carbon nanotubes. This system combines the advantage of size-dependent optical properties of CdSe NWs and the high conductivity of metallic carbon nanotubes on a very small area.

4.1 Individual CdSe Nanowires

4.1.1 Sample Preparation

CdSe NWs were synthesized using Bi nanoparticles (NPs) as catalysts[11,41]. A mixture of CdO, TOPO, and octanoic acid was dried and degassed under vacuum for 1 h at 100 °C. Then the flask was filled with N_2 and the temperature was raised to 300 °C. After CdO was completely dissolved, the system was adjusted to 250 °C. A mixture of Bi nanoparticles and TOPSe was quickly injected into the vessel and after 2 min the reaction was cooled down. Several mL of toluene were added to the solution to prevent TOPO from solidifying. Afterwards the nanowires were purified by repeated high-speed centrifugation.

To avoid bundling the following method was used: 100 µL of a stock solution of CdSe NWs were diluted with CH_2Cl_2 to 1 mL and centrifuged for 2 minutes at 18000 rpm. The overlaying solution was decanted and the process repeated two more times. Then, the suspension was treated with mild ultrasound for 5 min and 3-4 ultrasound pulses at 40 W. 20 μL of the suspension were withdrawn and spin-coated at approx. 5000 rpm on a silicon nitride membrane (50 nm thickness). Prior to deposition, a few drops of DI water and subsequently CH_2Cl_2 were dropped on the surface to remove potential remaining contaminants.

4.1.2 Correlation between Structure and Optical Properties

Investigated NWs typically exhibited a diameter distribution with an average diameter of 11 nm and a standard deviation of $\sigma \approx \pm 3$ nm. Therefore, thinner wires were specifically selected in the experiments and the data presented below does not reflect the actual size distribution of the samples. Without further treatment, most NWs form bundles and nanofibres upon deposition. Several parameters were tested to separate the wires. In short, ultrasonication debundles the wires, but at the same time reduces their average length. Also the number of fragments (CdSe NWs with length < 1 µm) increases. Centrifugation was used to purify the sample and remove CdSe nanocrystal admixtures which are formed during the synthesis as byproducts. However, thinner wires are also more difficult to precipitate, therefore wires with a larger diameter are enriched with each cleaning step.

Figure 4.1 shows a compilation of a scanned PL image, an AFM image, as well as TEM images of the same NW structure. The fluorescence image suggests emission of a single wire, including inhomogeneities of the PL emission with "hot spots" of strong emission. However, the AFM image reveals that the investigated structure is not necessarily a single NW. On the contrary, at least in the lower left part of the image, several NWs contribute to the PL emission.

Further, the TEM images allow a much closer look at the investigated structure. Here, clarified by the three magnified images, it becomes obvious that even when PL and AFM images suggest the investigation of a single NWs, in most cases two or three adjacent NWs are investigated. Comparison of different microscopy techniques demonstrates the difficulty in the investigation of individual NWs. From PL images alone it is not possible to decide whether the emission stems from a single wire. Even the spectrally dispersed PL emission does not prove the investigated structure to be a single wire. On the one hand, e.g., two adjacent NWs of the same size reveal a similar spectrum as an individual NW, on the other hand, the spectrum of two adjacent wires of different diameter is not necessarily just the sum of both spectra because of, e.g., energy transfer between the NWs. AFM images allow for a more reliable verification whether single NWs are investigated. However, due to limited lateral resolution, the assignment is not unambiguous when the NWs adjoin laterally (cf. figure 4.1).

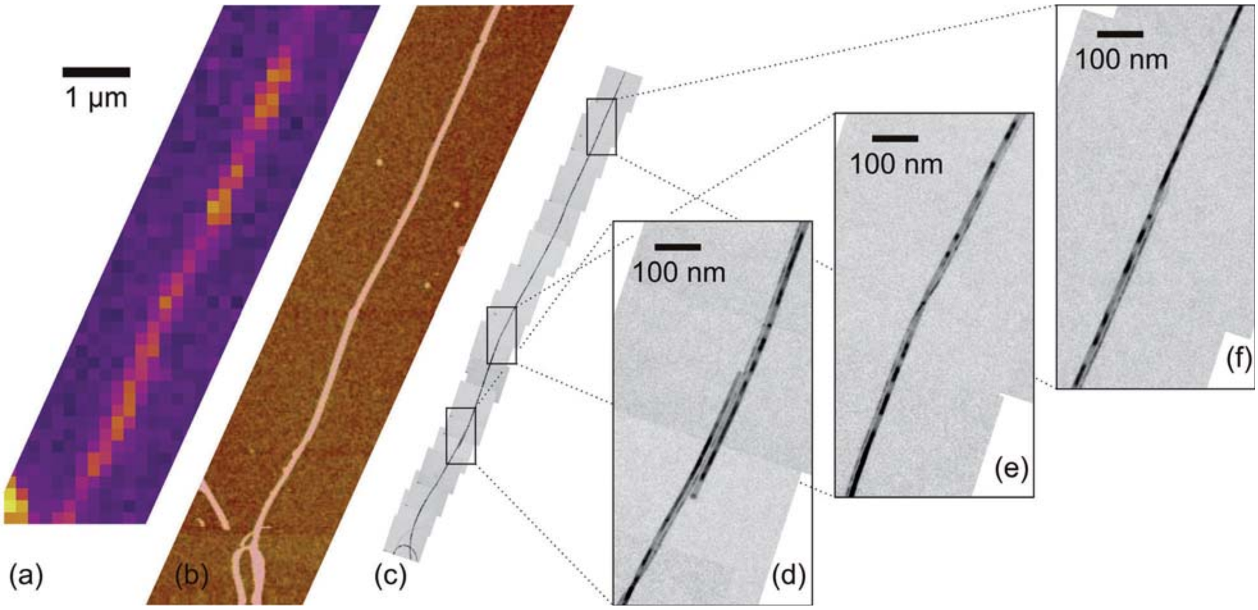

Figure 4.1: CdSe nanowires: a) PL image from a confocal microscope, b) AFM image of the same sample position, c) jointed TEM images of the same position, d-f) magnified areas marked in c). TEM images reveal that presumably single NWs, as judged from PL and AFM images, are in fact bundles of NWs. Additionally, AFM overestimates the diameter of the NWs, e.g., at the position of d) AFM gives a diameter of $\sim$ 14 nm, whereas the diameter determined from TEM for the three wires is 11.1 nm, 10.0 nm and 6.9 nm

Electron microscopy allows correlation of the PL data to the nanostructures under investigation. However, there are two major drawbacks: First, TEM investigations require special and easily damageable substrates for the NWs, like carbon coated copper grids or silicon nitride membranes. Second, TEM investigations drastically alter the optical properties of NWs. In fact, after TEM imaging, the NWs do not emit any measurable fluorescence anymore. Thus, the structural analysis of NWs by TEM can only be performed after a thorough investigation of their optical properties. To investigate the PL emission of single NWs and correlate it to their structural properties the following workflow was applied: First, the sample was characterized with AFM to estimate the overall quality of the sample. Despite above mentioned drawbacks of AFM, large agglomerates of NWs can be excluded from a more detailed investigation and regions of interest with presumably single NWs can be identified. Then, these regions were found again and investigated by scanning fluorescence microscopy. A comparison of AFM and confocal scans showed that presumably individual NWs have weak PL and can be easily overlooked. In several cases the PL is below the detection limit of the setup. The PL of presumably single NWs were recorded with spatial and spectral resolution for a subsequent in-depth analysis. Finally, these NW structures have been investigated by TEM.

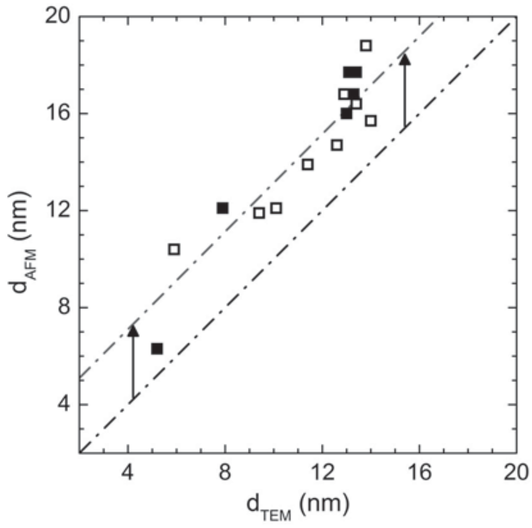

Figure 4.2: Comparison between diameters retrieved from AFM and TEM from the same individual nanowires. Solid squares are wires where luminescence was measured and which went into 4.4a. The black dash-dotted line shows the theoretical line for $d_{\mathrm{TEM}} = d_{\mathrm{AFM}}$. The red line is a linear fit of the experimental data. Compared to the black line it is essentially shifted by 3 nm.

The comparison of the three different microscopy methods revealed following general results. Individual NWs showed largely homogeneous PL along the whole NWs. Fluctuations in PL images mostly occur when bundled NWs are investigated. Figure 4.2 correlates the height of NWs as determined by AFM with their diameter as determined by TEM. The red line is a linear fit of the data proving that AFM typically overestimates the radius by about 3 nm. Since the AFM height depends on the interaction between the sample and the tip, it is influenced by the surface and ligands still attached to the NWs[54]. All optical data presented below has been measured from individual NWs, as verified by TEM. Figure 4.3 exemplarily shows two PL spectra of the thinnest and thickest NW under investigation together with their TEM images. The maximum PL emission energy strongly changes with the diameter of the NWs, as will be discussed in detail below. The typical PL peak's full width half maximum (FWHM) is about 80 to 90 meV. Investigation of the temporal evolution of the PL in consecutive time bins as small as 25 ms reveals intensity fluctuations. These fluctuations may be attributed to a similar process as the well known blinking of nanocrystals[55]. The rather large FWHM may originate from spectral shifting on a time scale smaller than 200 ms, i.e., the integration time of the spectrally resolved measurements. Furthermore, structural inhomogeneities of the NWs should contribute to a broadening. The diameter variations of the NWs were estimated by evaluating TEM images of several positions along each wire. Typical standard deviations are ±0.3 nm

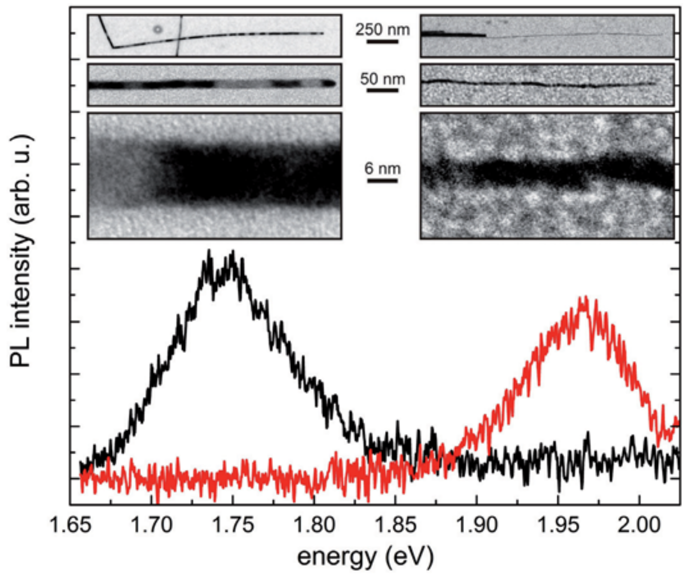

Figure 4.3: PL spectra of the thickest (black) and thinnest (red) NW under investigation. The inset show their TEM images of different magnifications. Differences in contrast may stem from changes in diffraction conditions, either by a rotation of a the stacking plane along the wire axis or by slightly shifting out of the beam focus. Another explanation may be charging of the sample.

for the whole range of different diameters. The effect of alternating crystal lattice modifications along the NWs will be addressed later. The data points in figure 4.4 a show the experimental results of the scaling of the optical band gap with the diameter of the NWs. The maximum PL emission energy was determined by fitting the rather broad PL emission of a NW with a Gaussian function. The optical band gap strongly increases with decreasing diameter.

4.1.3 Modeling of the Band Gap Energy

The diameter-dependence of the optical band gaps in CdSe NWs was modeled with the methods described in section 2.2. All calculations have been performed by Dr. T. Kipp and Dr. Ch. Strelow based on a code programmed with the software Mathematica. The results will be discussed at this point, as they are important to interpret the experimental findings.

As described in section 2.2, the optical band gap was separated into three parts: i) the diameter dependent quantization energy of electrons and holes due to the reduced diameter of the wire, ii) the exciton binding energy due to Coulomb attraction between an electron and a hole, and iii) the fundamental bulk band gap energy, which is independent of the diameter.

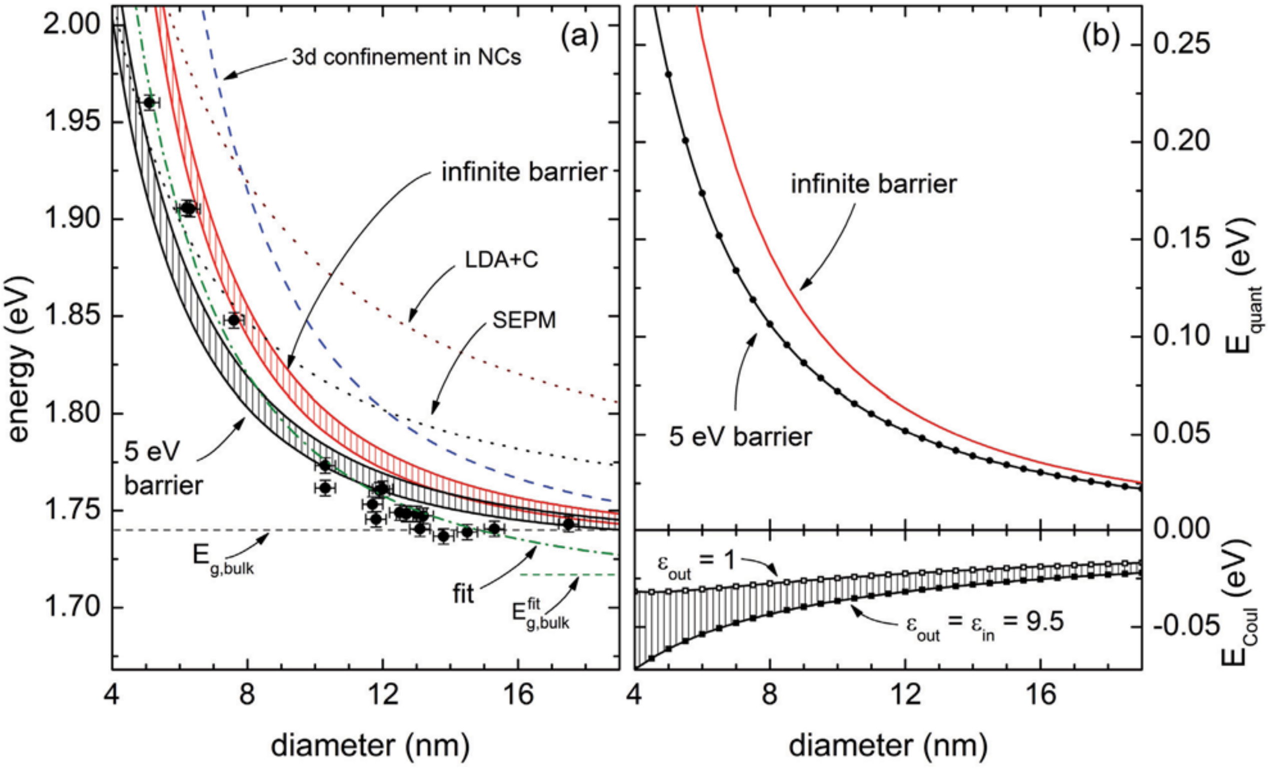

Figure 4.4: a) Scaling of the optical band gap with the NW diameter. The data points are experimental results, the lines represent model calculations. The red and black solid lines are results of the effective mass approximation (EMA), regarding the NW as potential well with infinite (red) or finite (height ≈ 5 eV, black) barriers. The lower line of both areas is calculated assuming no dielectric mismatch (i.e., $\epsilon_{\text{out}} = \epsilon_{\text{in}} = 9.5$) while for the upper curve $\epsilon_{\text{in}} = 9.5$ and $\epsilon_{\text{out}} = 1$ is assumed. The curves result from adding E_{quant}, E_{Coul}, and $E_{\text{g,bulk}}$. The green dash-dotted line represents results of the EMA obtained with fitted parameters (see text). For comparison, the blue dashed line shows the scaling of the optical band gap for spherical nanocrystals within the EMA. The dotted line represents results of different theoretical models reported in literature (see text). b) EMA calculation of E_{quant} for infinite and finite potential barriers (upper panel) and E_{Coul} with and without dielectric mismatch.

The diameter dependent quantization energy E_{quant} for a cylindrical CdSe NW is presented in the upper panel of figure 4.4b. The red curve represents the analytic solution of the Schrödinger equation for infinite barriers

$$E_{\text{quant}} \quad = \quad 2\hbar^2\beta_0^2\mu d^2 \tag{4.1}$$

where d is the diameter, $\beta_0 = 2.4048$ is the first root of the Bessel function J_0, and μ is the reduced effective exciton mass $\mu = (m_e m_h)/(m_e + m_h)$. For the effective electron and hole masses bulk values $m_e = 0.12m_0$ and $m_h = 0.5m_0$ were assumed (cf. Refs. 56 and 57). However, a possible ligand environment around the wires, as well as the supporting Si/SiO$_2$ substrate, should be better represented with finite barriers. The black curve was obtained by setting the barrier height to $U = 5$ eV[58] and numerically solving the corresponding Schrödinger equation with the Ben Daniel-Duke boundary conditions for the wavefunction at the semiconductor/air interface[32,59,60]. As can be seen from the diagram, E_{quant} strongly depends on the NW diameter. The different barrier heights E_{quant} most strongly alter for small diameters, and even for diameters as large as 20 nm E_{quant} is not negligible.

Slachmuylers and coworkers derived an analytical formula for the Coulomb binding energy of electrons and holes in a cylindrical NW, including the mismatch of the dielectric permittivity inside and outside the NWs[34]. The lower panel of figure 4.4b shows the numerical results for CdSe NWs, assuming a relative permittivity of $\epsilon_{\text{in}} = 9.5$ inside the CdSe NW (cf. Ref.[61]). Two cases are distinguished: either no dielectric mismatch, i.e., $\epsilon_{\text{out}} = \epsilon_{\text{in}}$, or a permittivity outside the NW of $\epsilon_{\text{out}} = 1$, corresponding to vacuum. The Coulomb interaction is smaller than the quantization energy, but its impact is not negligible. The dielectric mismatch leads to a weakened Coulomb interaction. Therefore the dielectric mismatch is taken into account, even though the effective relative permittivity differs from the vacuum value.

Adding $E_{\text{g,bulk}}$, E_{Coul}, and E_{quant} for the different model calculations the theoretical values gives the optical band gap, that can be compared to the experimental data. Results are shown as solid lines in 4.4a. The red (black) lines correspond to the infinite (finite) barrier model. In both cases, the dielectric mismatch is taken into account only for the upper curve. In principle, the model calculations follow the experimental data, however, some deviations are visible. These can be explained by intrinsic shortcomings of the two-band effective mass approximation itself, in particular for nanometer-sized structures, as well as by the uncertainty of the bulk parameters assumed for the calculation. For the effective electron and hole masses that are taken into account for the calculation of E_{quant} as well as for the relative permittivity that is needed to calculate E_{Coul} and even for the fundamental band gap $E_{\text{g,bulk}}$ several different values are given in literature[57,62]. The experimental data is fitted with the above given model assuming finite barrier heights for the calculation of E_{quant} and a strong dielectric mismatch ($\epsilon_{\text{out}} = 1$) for the calculation of E_{Coul}. Starting with the parameters given above, a better congruence is obtained for larger barrier heights, smaller effective masses and a smaller fundamental band gap. The dash-dotted curve in 4.4a, calculated for $m_e = 0.10m_0$, $U = 10$ eV and $E^{\text{fit}}_{\text{g,bulk}} = 1.717$ eV, fits the experimental data quite well. However, since there are four free fitting parameters, different combinations are possible.

Finally, the experimental data is compared to other models which simulate the electronic properties of semiconductor NWs. The first is the plane-wave semi-empirical pseudopotential method[14]. An increase in the band gaps of

CdSe quantum wires within the diameter range of $d = 1.39 - 13.25$ nm was found. The theoretical results were fitted empirically and the band gap was determined, with $E = E_{\mathrm{g,bulk}} + 1.82\ \mathrm{eV} \times (d/\mathrm{nm})^{-1.36}$. Assuming 1.74 eV as the bulk band gap, the result is included in figure 4.4 a as the black dotted line. This calculations overestimate the experimental PL peak. However, the Coulomb interaction was not taken into account. The increase of the energy with decreasing diameter is considerably smaller in theory compared to the presented experimental results.

The second approach relies on *ab initio* calculations using density functional theory under local density approximation in which the bulk effective mass is corrected to fit experimental values (LDA+C). This approach yields good values for the diameter dependent confinement energies, while the obtained absolute band gap energy should be corrected by a constant value to fit with the bulk band gap[63]. In this publication the authors calculated confinement energies and explicitly included electron-hole Coulomb interaction for diameters between 1.36 nm and 4.37 nm, then fitted their results empirically, and found an $E = E_{\mathrm{g,bulk}} + 2.0\ \mathrm{eV}/(d/\mathrm{nm})^{1.16}$ dependence. This result is also included in figure 4.4a, though strictly speaking, these results have been obtained for a diameter range smaller than accessible by the described synthesis. The curve generally lies above the experimental data, however, its slope fits the experiments better than the SEPM results.

4.2 Effective Band Gap and Crystal Structure

The investigated CdSe wires exhibit alternating WZ and ZB segments, as can be seen in the high-resolution TEM image in figure 4.5 a. The different phases complicate the discussion above of the optical band gap since their physical properties differ (cf. section 2.1)[15,16,27–29]. Theoretical works reveal a smaller band gap of the ZB modification in the range of $\Delta E_{\mathrm{g}} = 46 - 85$ meV, as well as conduction band (CB) and valence band (VB) offsets of $\Delta E_{\mathrm{CB}} = 76 - 144$ meV and $\Delta E_{\mathrm{VB}} = 30 - 59$ meV, respectively, leading to a staggered type-II potential along the NW with CB minima in the ZB segments and VB band maxima in the WZ segments[27–29]. Such a potential, corresponding to the TEM image, is sketched in 4.5 b.

The implications on the optical properties of the NWs are twofold: First, one might assume that the type-II potential along the wire leads to an effective confinement of charge carriers along the NW. The lowest electron and hole eigenenergies and corresponding wave functions were calculated for the sketched potential within the effective mass approximation (EMA) by numerically solving the Schrödinger equation. The Coulomb attraction was

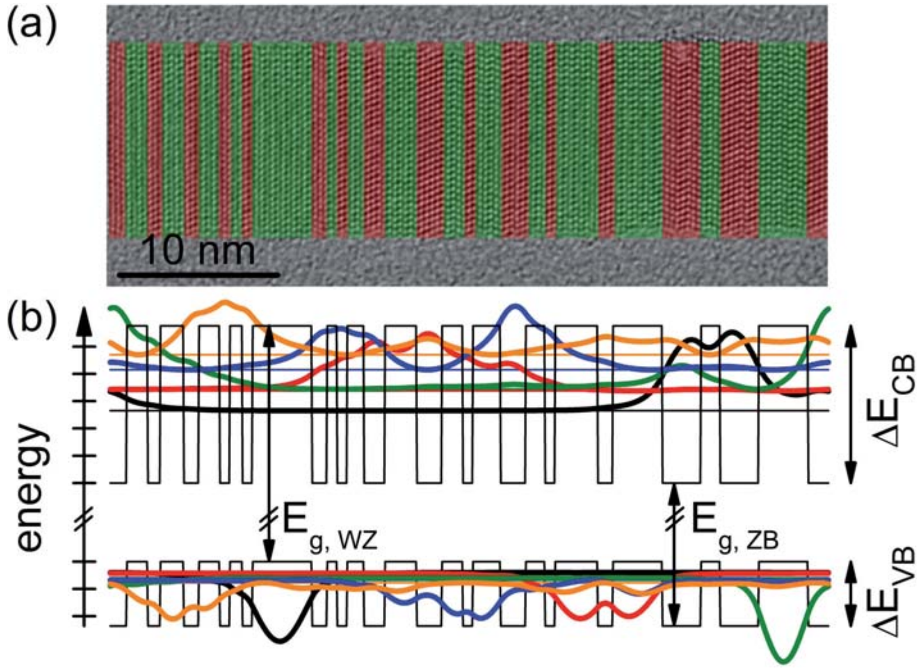

Figure 4.5: a) Typical high-resolution TEM image of a NW, where alternating crystal modifications can be distinguished. Wurtzite (zinc blende) segments are colored green (red). b) Scheme of the corresponding type-II potential of conduction and valence band (black), calculated lowest electron and hole eigenenergies (colored horizontal lines), and the corresponding squared wave functions. For the calculation $\Delta E_{\mathrm{CB}} = 144$ meV and $\Delta E_{\mathrm{VB}} = 59$ were assumed. The spacing of the tick marks is 25 meV.

not considered. For the model calculations the largest of above given theoretically predicted band offsets of $\Delta E_{\mathrm{CB}} = 144$ meV and $\Delta E_{\mathrm{VB}} = 59$ meV were assumed[29], since this should generate the strongest axial confinement. Periodic boundary conditions accounted for the much larger length of the real NW compared to the TEM image detail. The horizontal lines in figure 4.5b represent the five lowest electron and hole eigenenergies of the CB and VB potential, respectively. The corresponding squared wave functions are attached. For the CB, the energy difference of neighboring eigenstates is smaller than the thermal energy at room temperature ($kT \approx 25$meV = spacing of tick marks) and the corresponding wave functions do considerably overlap. The same applies for the VB, where the wave functions are less expanded, but the energy difference is much smaller.

These model calculations reveal that the different ZB and WZ segments are too short to effectively trap charge carriers at room temperature. Comparing the experimental data with the theoretical optical band gap of spherical CdSe nanocrystals treated in the effective mass approximation including Coulomb attraction, $E = E_{\mathrm{g,bulk}} + 2\hbar^2\pi^2/(\mu d^2) - 1.8e^2/(2\pi\epsilon\epsilon_0 d)$, as obtained by Brus[59] (dashed blue line in figure 4.4a), reveals that the three-dimensional confinement in QDs leads to a much stronger energy increase with decreasing diameter than in NWs. This is a strong indication for a two-dimensional confinement in the NWs investigated. A true quantum wire behavior is observed, as has been extensively discussed in refs. 14, 64, and 65.

The staggered type-II potential has a second implication concerning the effective fundamental band gap of the NW. Depending on the band alignment of WZ and ZB segments and on their mean widths, their band gaps differ from the bulk band gaps of the pure WZ or ZB phases. Assuming the above given band offsets, figure 4.5b illustrates that the effective band gap is smaller than the fundamental WZ band gap (up to 70 meV), but larger than the fundamental ZB band gap.

Another impact of the type-II potential affects the PL emission line width. The modeled potential in 4.5b has an overall length of about 45 nm while PL is detected from an area of at least 250 nm. On this rather large length scale the statistical nature of the segment lengths should indeed lead to an inhomogeneous broadening of the PL emission line, making the experimentally measured line widths reasonable (cf. figure 4.3).

4.3 Heterostructures of Carbon Nanotubes and CdSe Nanowires

With an all chemical route CNTs and CdSe NWs have been assembled to hybrid devices. Thereby, the problem of creating intimate contacts is avoided. The combination of individual nanostructures to more complex hybrid devices in a self-assembly process allows to further tailor their chemical, electronic, and optical properties. Such CdSe-Bi-CNT hybrids offer a wide range of applications as light-harvesting devices or photodiodes. In this section their optical properties will be discussed.

4.3.1 Synthesis

Synthesis on the substrate has two advantages with respect to the conventional synthesis in solution. First, individual wires are synthesized[66]: since NWs can only grow from bismuth particles, isolated Bi NCs can be deposited with appropriate electrochemical modification (ECM) conditions to keep a certain distance between CdSe NWs. Typically, one wire grows from one particle. Therefore bundles are avoided and the interpretation of data is much easier, than for spin-coated wires, described in section 4.1.2. Second, a clean interface between the CdSe, Bi and the CNT is created: Bismuth is directly reduced on the tube without an intermediate agent. In addition, only those Bi particles show catalytic activity which are not passivated on the surface.

After the growth of CNTs on a silicon substrate (cf. section 3.1), gold electrodes were deposited with conventional lithography. Then, a Bi solution was prepared with concentrations of 0.05 mᴍ to 0.1 mᴍ $BiCl_3$, 1 ᴍ HCl, 1 mᴍ KCl as an electrolyte and 5 mᴍ poly-(vinylpyridine) as a surfactant. The solution was purged with Ar for 20 minutes to remove oxygen. Then, the substrate was immersed into the solution in an electrochemical cell. A potential of 0.9 V to 1.5 V was applied with a potentiometer (HEKA Potentiostat Galvanostat PG 310) for 5 s to 10 s using a tungsten needle as a working electrode which was connected to an electrode and the CNTs underneath. Silver and platinum wires were used as reference and counter electrodes, respectively. After the electrochemical reaction, the sample was taken out and rinsed with DI water. Finally, the CdSe NWs were synthesized directly on the substrate with the multiple injection SLS method[66], similar to the procedure described in section 3.1.

4.3.2 Optical Properties of CNT-Bi-CdSe Heterostructures

Detection of PL and Raman scattering in one and the same setup allows to study optical properties of the CNT-Bi-CdSe heterostructures. PL emission above 520 nm was measured with a point-detector (APD 1, cf. figure **??**). The Raman signal from the G-line of the CNTs (1592 cm^{-1}) was isolated with a spectrograph and detected with a second detector (APD 2).

In figure 4.6a an AFM image of a typical sample is shown. Figure 4.6b displays a superposition of the PL of the CdSe wires (red, left scale bar) and Raman signal of the tubes (yellow, right scale bar) of the same area. CdSe wires are marked with dotted arrows to indicate their growth direction. Corresponding spectra are shown in figures 4.6c and figures 4.6d. Not all carbon nanotubes are visible for one particular excitation wavelength since Raman scattering probability strongly depends on the resonance condition[67].

Overall, the NWs show a the quantum-size effect (figure 4.7). The PL peak position shifts to higher energies as the height of the wires decreases, which was determined by AFM. However, due to the distortion of the wire diameter in the AFM, as discussed in section 4.1.2, this data could not be analyzed quantitatively.

Figure 4.8 a shows a SEM image of three CdSe NWs and the corresponding PL image (figure 4.8 b). The diameter of the CdSe wire gradually increases with rising distance from the Bi particle, which can be seen in the AFM in figure 4.8 c. Also, the fluorescence varies for different sections of the wire. This may be attributed to the fluorescence of ligands and organic contamination still present on the sample. Their fluorescence, which is spread over the whole

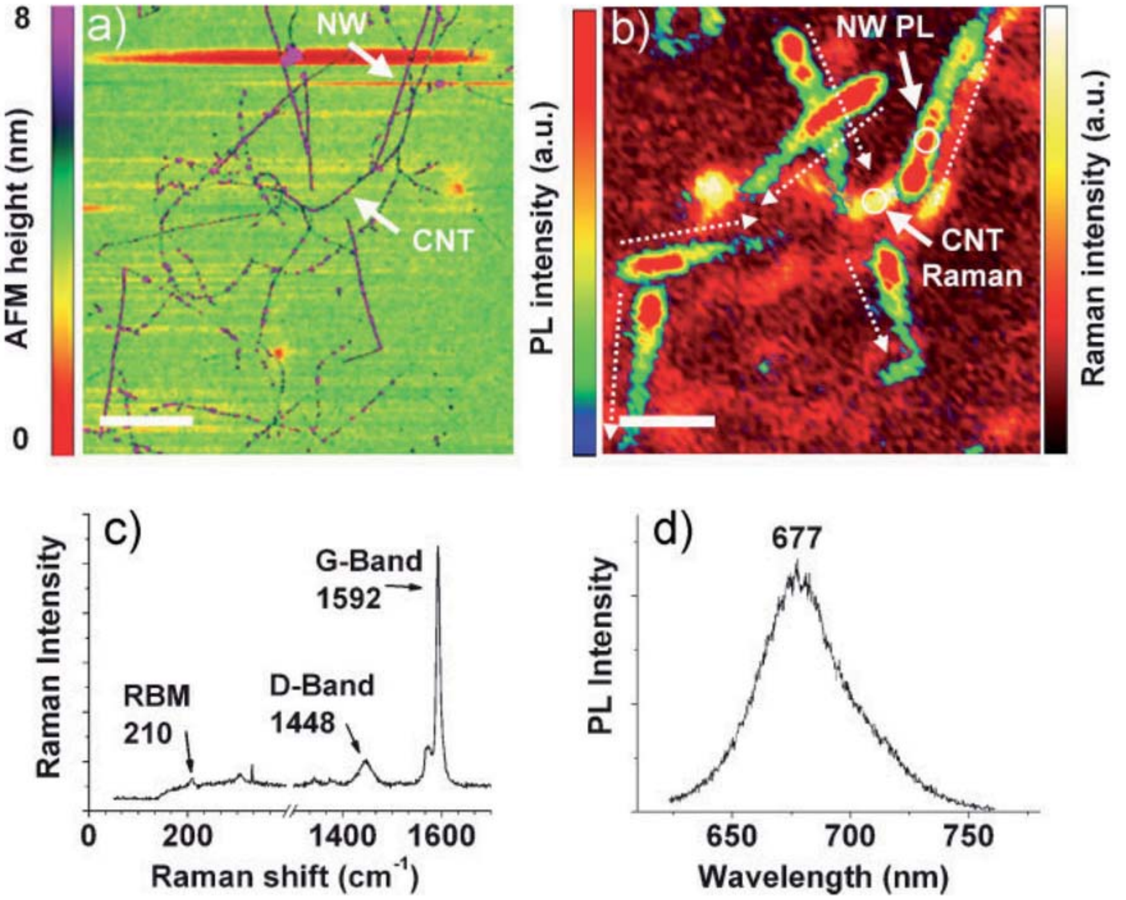

Figure 4.6: a) AFM image of CNT-Bi-CdSe heterostructures. Nanowires and carbon nanotubes can be distinguished by different colors, according to the scale; b) Superposition of a G-line Raman scan of the CNTs and a PL image of the CdSe NWs; the scale bar length is 1 μm, the dotted arrows indicate the growth direction of the nanowires. c) Raman spectrum of the CNT indicated by the arrows in a) and b); d) PL spectrum of the CdSe NW indicated by the arrow in a) and b).

visible range of the spectrum, adds a significant background, and is in some cases even comparable to the NW signal in the confocal image.

The specific reaction conditions may also explain the diameter change of the wire, as well as account for the enhanced PL at the thinner end. After the ECM no further Bi precursor is delivered from solution, and the Bi might partially dissolve into the CdSe wire, thus shrinking during further growth. The amount of dissolved bismuth in the CdSe wires is expected to be very low and cannot be detected within the accuracy of energy-dispersive X-ray spectroscopy (EDAX)[68].

This gradual decrease of the Bi nanocatalyst volume is followed by a successive decrease of the CdSe NW during the growth process. A similar mechanism was suggested for silicon NWs grown from gold catalysts by the vapor-liquid-

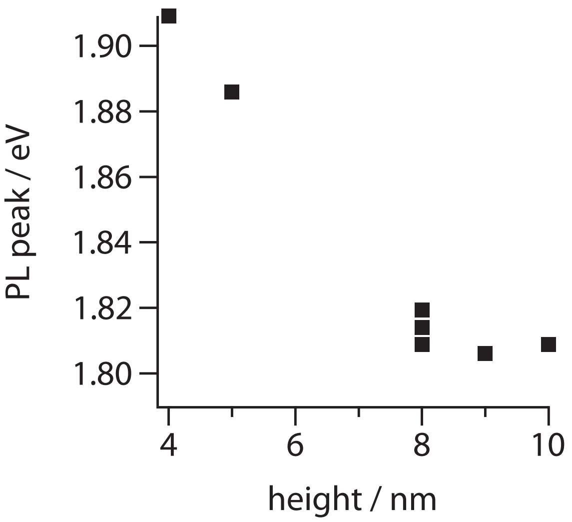

Figure 4.7: Dependence of the PL energy on the wire diameter, determined by AFM. A shift to higher energies is observed for thinner wires.

solid (VLS) mechanism[69]. Moreover, a recent theoretical study predicted that the impurity concentration of the catalyst material inside the wire decreases with its diameter[70]. Such a dependency may also explain the low PL intensity of CdSe NWs in general (quantum yield (QY) $< 1\,\%$)[9], as well as the fluorescence intensity fluctuation along the wires. Since Bi impurities will lead to an n-type doping of the CdSe nanowires, the excess charge carriers could quench the NW fluorescence in an Auger-like process, a mechanism that has already been proposed for the PL quenching in CdSe nanocrystals[71].

The assumption of a lower concentration of Bi at thinner sections of the CdSe nanowire would provide a possible explanation for the increased fluorescence at thinner parts of the nanowires observed during investigations. However, a more detailed analysis of the structure and chemical composition of the nanowires in relation to investigations of the fluorescence dynamics of individual nanowires is needed to verify this hypothesis.

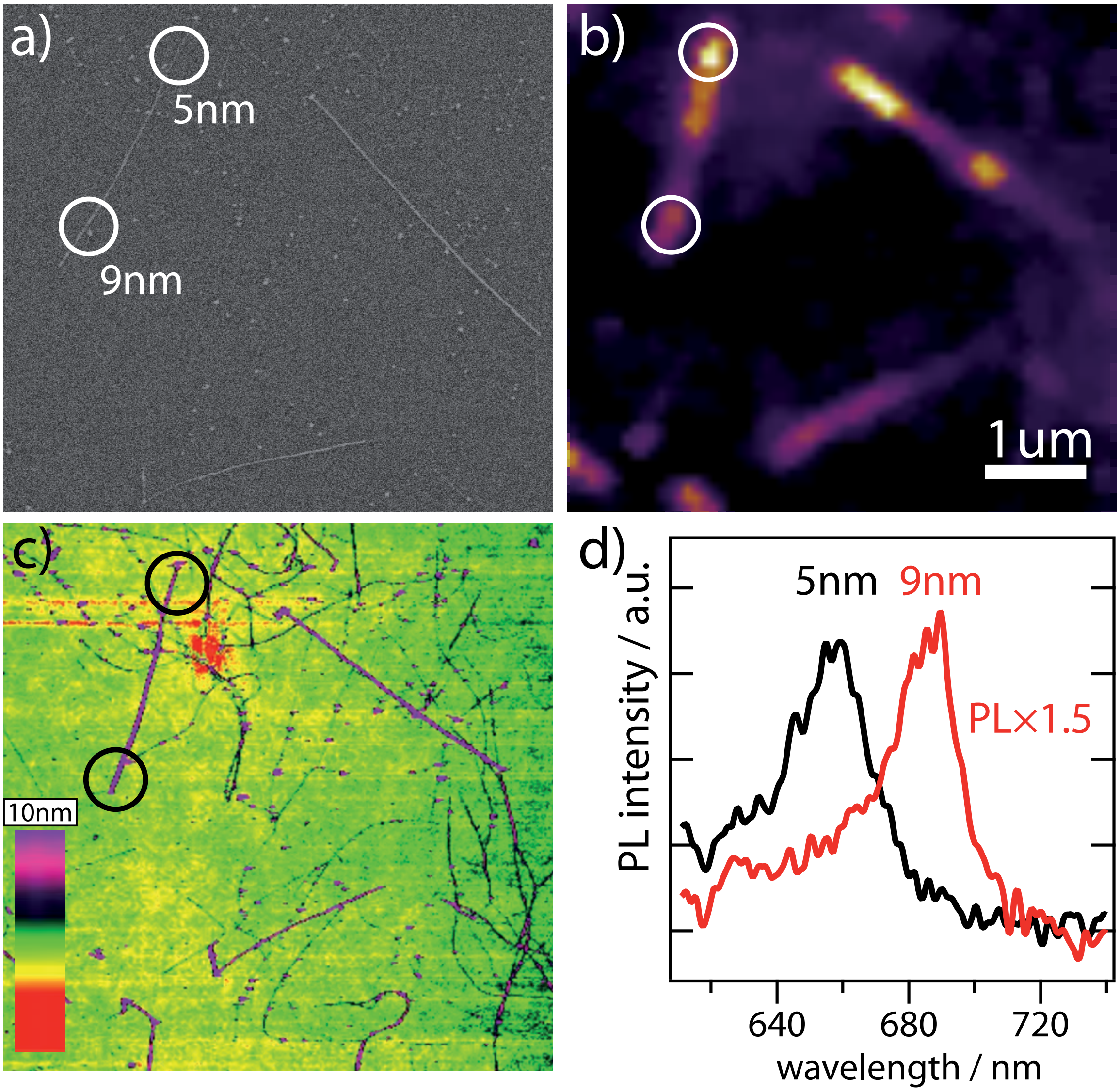

Figure 4.8: Correlation of morphology, PL intensity, and the respective spectra of individual CdSe NWs. a) SEM image of three CdSe nanowires, with diameters gradually increasing with greater distance from the Bi catalyst. b) PL is higher at the thinner part of the NW close to the Bi particle. c) Spectra taken at the positions marked in a) and b), the PL peak shifts to higher energies for thinner parts of the NW according to size quantization effects.

5 Photosensing Devices from CdS Nanowires

In this chapter the optoelectronic properties of a CdS NW device are discussed. Gold and titanium are used as electrode materials to form different types of asymmetric contacts. Such structures are of particular interest for photodetectors and photovoltaic devices. In contrast to conventional p-i-n photodiodes, metal-semiconductor-metal (MSM) photodetectors are planar, can be prepared by photolithography and are compatible with existing FET technology. First, the Au-CdS-Ti samples were optically and electrically characterized. Then, a closer look at the photovoltaic processes at the Schottky junction was taken. Finally, the photocurrent and photoluminescence characteristics were manipulated by varying the bias to obtain a deeper insight into the band structure of CdS NWs.

5.1 Sample Preparation

CdS NWs are formed by a controlled precipitation of Cd^{2+} and S^{2-} ions, dissolved in ethylendiamine (en):

$$Cd^{2+} + S^{2-} \longrightarrow CdS\downarrow \tag{5.1}$$

Spherical particles are formed without former precautions. Anisotropic growth can be achieved either by adding a catalyst, e.g. gold NP[72], in a CVD synthesis in the gas phase, or by coordinating ligands in solution[73].

NWs used within this work were synthesized by dissolving 1 mmol of cadmium diethyldithiocarbamate $[(Cd(S_2CN(CH_2CH_3)_2]_2)$ in 50 ml ethylenediamine $H_2N{-}CH_2{-}CH_2{-}NH_2$ and heating to 200 °C for 48 h in an autoclave. Single-crystalline CdS wires were obtained from this solvothermal reaction with lengths of up to 20 µm and diameters in the range between 20 to 80 nm. The wires were dispersed in ethanol and ultrasonicated for 30 s to avoid bundling. Subsequently they were deposited on silicon substrates with a 300 nm thick SiO_2 layer and gold marker structures used for localizing individual NWs.

The samples were provided by the group of Prof. Kern at the Max-Planck-Institute of Solid State Research. Electron-beam lithography was used to define the electrode structures to contact CdS NWs. Hereby, polymethylmethacrylate (PMMA) is used as a positive photoresist. Upon irradiation with an electron beam its molecular weight was reduced and the treated polymer was removed with an appropriate solvent. The exposed regions were treated with an Ar-ion bombardment to n-dope the CdS contacts. In two subsequent steps $\sim 80\,\text{nm}$ of titanium and gold were evaporated on top.

5.2 Optoelectrical Characterization of Au-CdS-Ti Devices

An overview of an as-prepared device is given in figure 5.1. Panel a) shows an optical reflection image taken with the confocal microscope with a spot size of around 300 nm. The gold and titanium electrode can be distinguished, since they reflect more light. Gold markers, with a spacing of 10 µm, were used to localize the contacts. A scheme of the finished device is shown in 5.1 b. It should be noted that the CdS lies under the respective electrode, therefore allowing an intimate contact between the metal and the semiconductor. A 3-D visualization of an AFM image of the same area can be seen in fig. 5.1 c. Different heights of the CdS NWs and the electrodes are represented by different colors. The CdS NW has a diameter of aproximatly 60 nm, as can be seen from the cross-section (fig. 5.1 d), and extends underneath both electrodes. The height of the unique gold markers in the vicinity is around 20 nm.

A fluorescence image is presented in fig. 5.1 e, collected with a longpass filter in front of the APD to remove scattered laser light. Adjacent CdS wires can be used to determine the exact position of the sample. In the PL spectrum (fig. 5.1 f) two bands were identified. First, the sharp peak at 2.48 eV which corresponds to the band edge emission of bulk CdS. Part of this PL is cut off due to a laser line filter at 2.54 eV. Since the NW diameter is significantly larger than its Bohr exciton radius, no quantum confinement effects are observed (cf. Ref. 74). Second, the broad emission peak at lower energy may be attributed to deep trap states in the band gap region. The ratio between these two peaks, as well as the overall PL intensity, varied from wire to wire. Still, radiative exciton recombination from deep traps contributes significantly to the detected PL signal which suggests there is a large number of surface defects present in the CdS wire. Similar observations were made by Zhang *et al.* by adjusting the *pH* during synthesis and adding an excess of Cd^{2+} ions[75]. In principle,

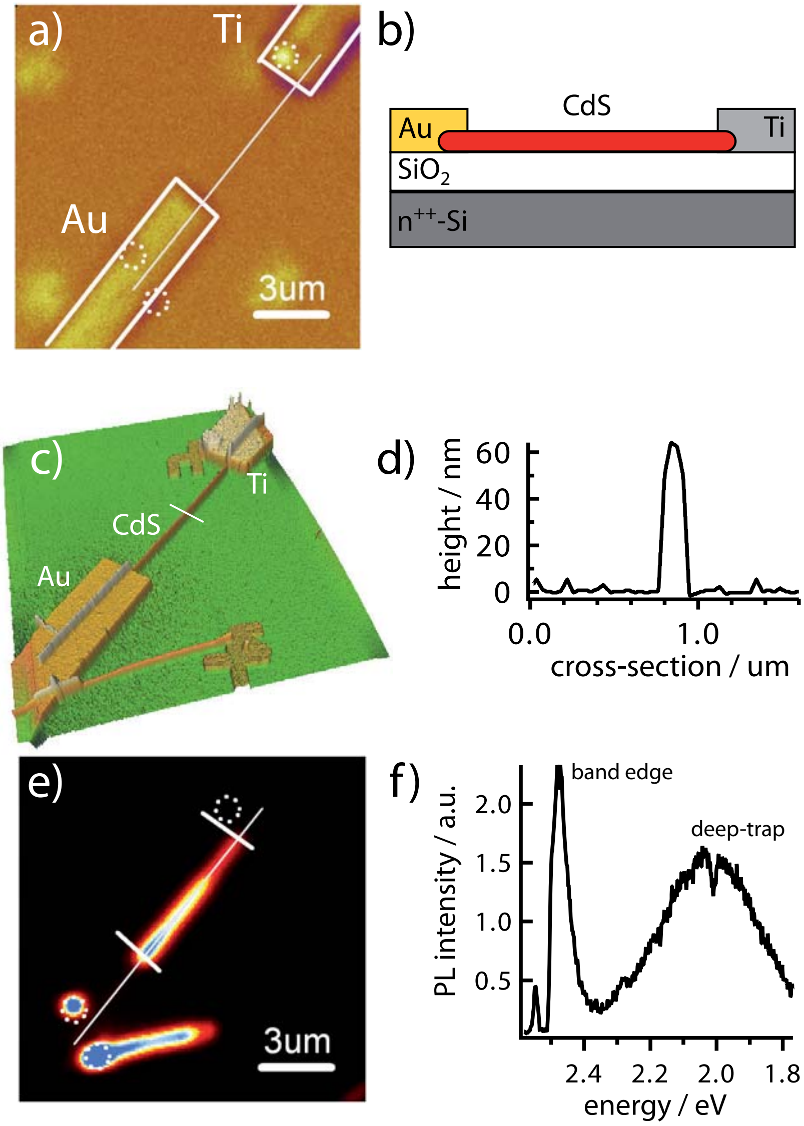

Figure 5.1: a) Optical reflection image of an Au-CdS-Ti device. The position of the electrodes and the CdS wire is marked with white lines. b) Scheme of the device. The CdS is clamped between the insulating SiO$_2$ and the metal contacts. c) AFM image of the same device. Areas where Au and Ti have been evaporated on top of the CdS NW are elevated. d) Cross-section view, taken along the white line in c). The CdS wire has a diameter of ∼60 nm, which is far above the Bohr exciton radius. e) Fluorescence image of the same area. PL is detected from all non-covered CdS parts. f) PL spectrum of the same wire. The band-edge emission corresponds to the bulk value of 2.4 eV. The broad peak originates from emission from deep traps. The laser excitation peak at 2.54 eV is not completely removed by the longpass filter.

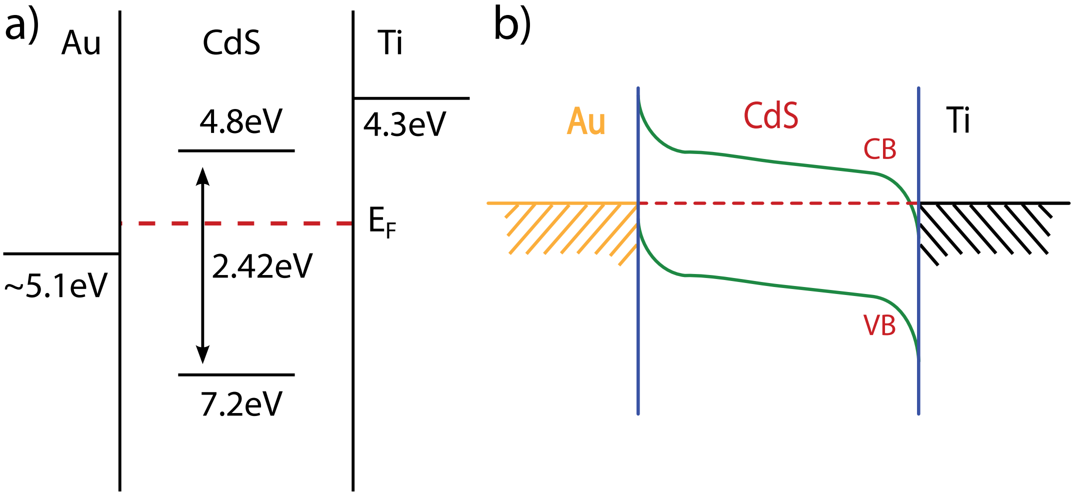

Figure 5.2: a) Bulk gold and titanium work functions of Au and Ti and CdS valance and conduction bands[76]. The position of the conduction band CB is given by the electron affinity, the position of the valence band VB is determined by the band gap. b) When brought in contact, their Fermi energies align. Charges accumulate at the interface, leading to a Schottky barrier for electrons at the Au-CdS contact and an ohmic contact at the Ti-CdS side.

this corresponds to n-doping of the CdS by creating sulfur-vacancies through Ar-plasma.

Usually, the Au contact was used as drain electrode while current was measured at the Ti source electrode. The silicon substrate may be used as a back-gate to apply an electric field in a field-effect-transistor configuration.

In figure 5.2 a the work functions of bulk gold and titanium and valance and conduction bands of bulk CdS are shown. All values were obtained from Ref. 76. Since the CdS NWs typically show n-type behavior, their Fermi-level is located closer to the conduction band than to the valence band. When brought into contact, their Fermi levels equilibrate. A Schottky-type contact is formed on the Au contact range of the CdS NW while the Ti-CdS contact exposes ohmic behavior. Strictly, this picture is only valid without light, where electrons are majority charge carriers. Under illumination, electron-hole pairs are generated – therefore both types of charge carriers contribute to the photocurrent.

The wires were illuminated with the 488 nm (2.54 eV) Ar-laser line, which is sufficient to excite electrons across the band gap of CdS ($\Delta E_g = 2.42$ eV). In contrast to CdSe NWs, discussed in chapter 4, CdS NWs exposed excellent long-term photostability and could be investigated over a long time: Reproducible results for PL and PC could be obtained for the same wires even after several weeks. During the first minutes of illumination the conductivity typically increases by up to one order of magnitude. In figure 5.3 the photosensitivity of the CdS wires is shown. At bias V_{ds} of 1 V and illumination power of 1 µW the

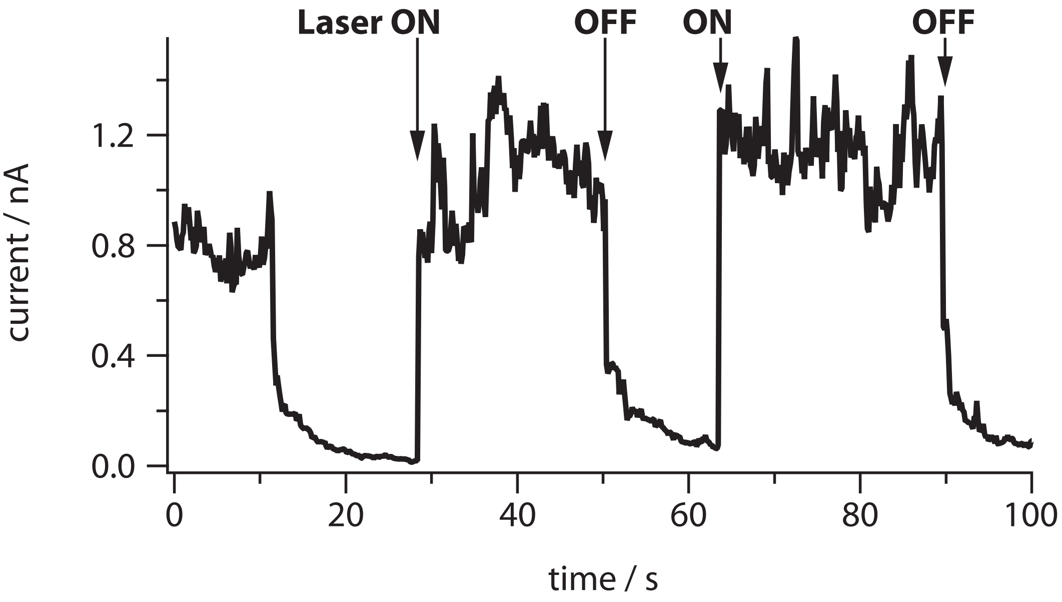

Figure 5.3: Photoconductivity of the CdS at bias $V_{\mathrm{ds}} = 1\mathrm{V}$. Upon illumination the NWs show an increased conductivity. After the laser has been turned off the dark current is higher than initially.

conductivity increases by a factor of 100. After the laser has been switched off, the dark current is higher than before illumination but decreases slowly with time. This effect may be due to desorption and reabsorption of O_2-molecules at the wire surface[77]. Recently it was shown that the conductivity of CdS NWs strongly depends on the oxygen partial pressure[78]. O_2 molecules, adsorbed at the surface, donate electrons into the CdS, thus filling the traps below the Fermi level. When the CdS is illuminated, the photo-generated holes can recombine with the adsorbed oxygen anions, O_2^-, releasing the O_2 molecules.

The observed dark currents are very small, around 10 pA at -1 V. For $+1$ V bias the current is beyond the detection limit of the experimental setup ($<$5 pA). Figure 5.4 a shows I-V curves for different excitation powers when the whole device is illuminated. The conductivity increases with higher excitation power.

To further elucidate the origin of the photocurrent, only specific regions of the device have been illuminated (figure 5.5 a). The red curve shows photocurrent while illuminating at the titanium electrode. The blue curve corresponds to illumination in the middle part of the CdS NW, the green curve represents the PC behavior when shining on the Au electrode. The sum of all three curves is represented by the black dotted line. Under negative bias, photocurrent upon illumination at the gold contact is observed, while a photocurrent on titanium is collected only under a positive bias. This can be visualized with SPCM, as described in section 3.3.2. The maximum current in figure 5.5 b is 85 nA for -9 V and 50 nA for $+9$ V in 5.5 c (cf. also figure 5.9). Horizontal "fringes"

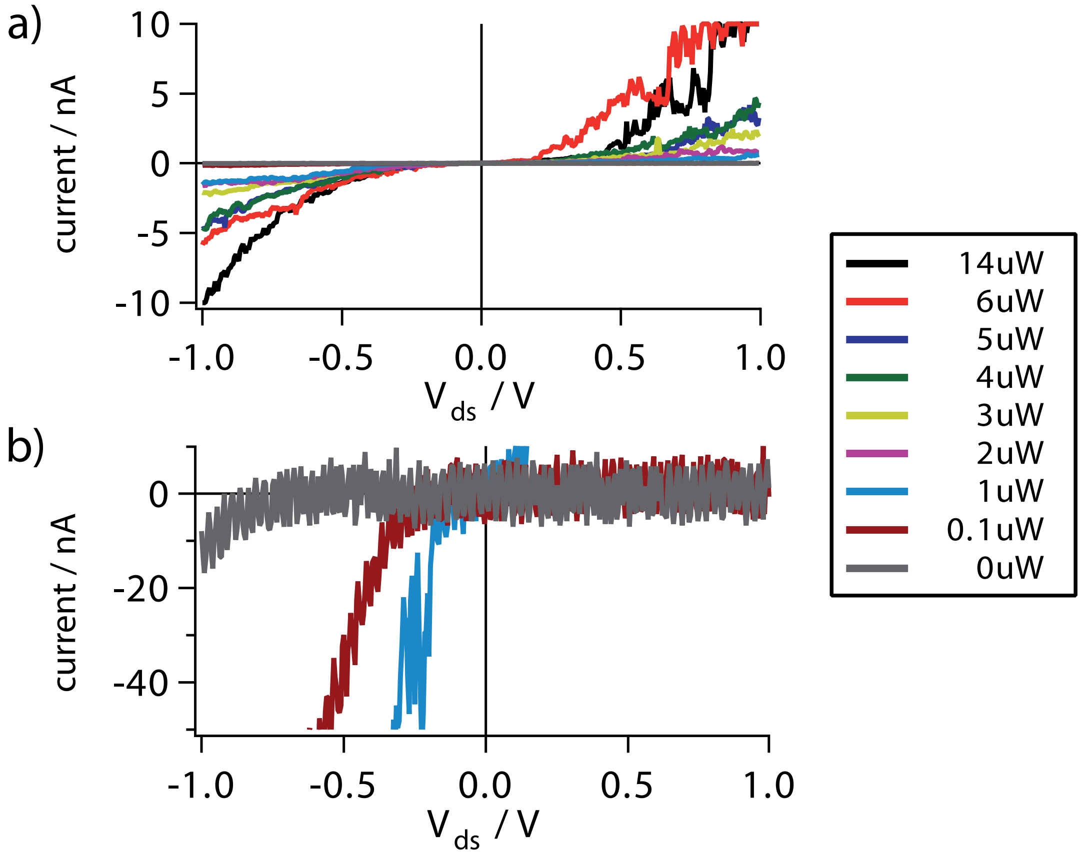

Figure 5.4: a) Typical I-V curves for Au-CdS-Ti devices at different excitation powers at 2.54 eV / 488 nm. b) Zoom in on low excitation powers.

along the scanning direction (left/right) are equivalent to the time-trace in figure 5.3 after the laser has been turned off and illustrate the rather slow oxygen resorption.

This suggests that by lifting the potential of the gold, electron flow through the wire is facilitated (cf. section 2.3.1). Holes are collected directly at the gold contact. The same holds for a positive bias: holes are now collected at the titanium electrode, while the electrons drift to the gold through the CdS. This is in accordance with the results of Lauhon *et al.* who observed a five times lower mobility of holes in CdS NWs[79], compared to electrons. The corresponding band schemes are shown in the insets of fig. 5.5 and will be discussed later in more detail.

Further, different areas of the NW displayed different photoconductivities. The steps where the changes occur coincide with the variations in PL intensity (cf. fig. 5.1 e) and may be attributed to different curvatures of the conduction and the valence bands, which will be discussed later in this chapter.

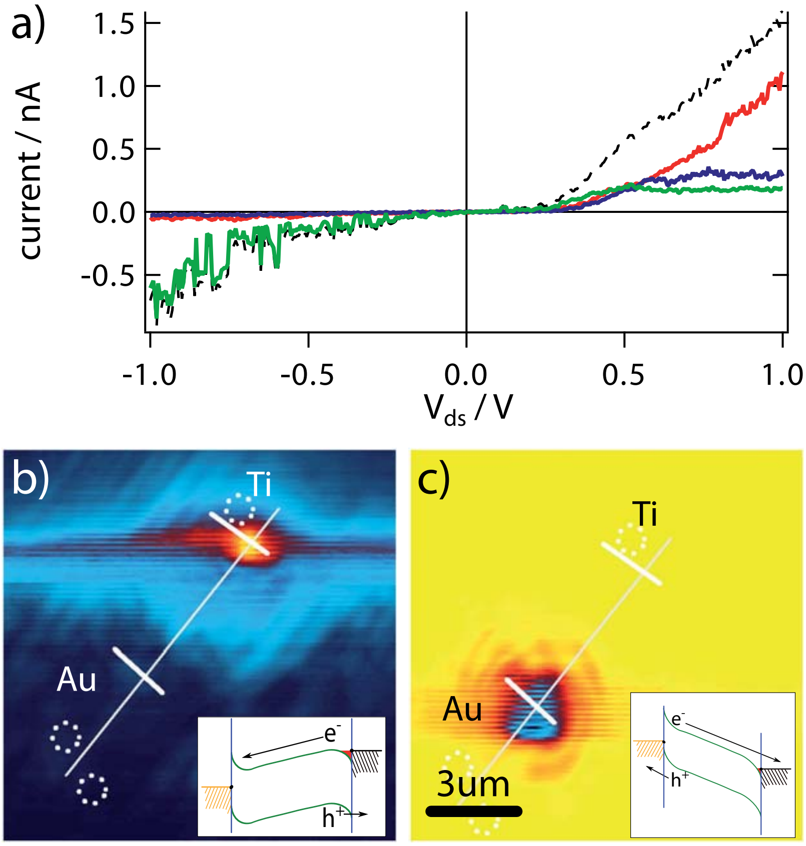

Figure 5.5: a) Spatially resolved photocurrent measurements: photoexcitation close to the Ti electrode (red curve); excitation in the middle of the CdS wire (blue curve); close to the Au electrode (green curve). The black curve represents the sum of all three characteristics. b) An SPCM image for a positive bias; c) An SPCM image for a negative bias. The insets illustrate the movement of charges.

5.3 Photocurrent Microscopy on Individual CdS NWs

Photocurrent and fluorescence are competitive processes. The absorption of a photon creates an electron-hole pair within the semiconductor. This exciton can either dissociate into free charges, which contribute to the current, or decay radiatively to emit a photon. Both rates are determined by the shape of the valence and conduction band, as well as the Coulomb binding energy of the exciton and its lifetime. Therefore changes in crystal structure along the wire axis should be reflected in modulations in PL and PC.

5.3.1 Schottky Junction-Based Photovoltaics

Dai and coworkers have shown that CdS-Au Schottky contacts can be used as simple photovoltaic devices[80]. Due to charge transfer from the n-doped CdS NW to the electron-accepting gold electrode a band-bending occurs at

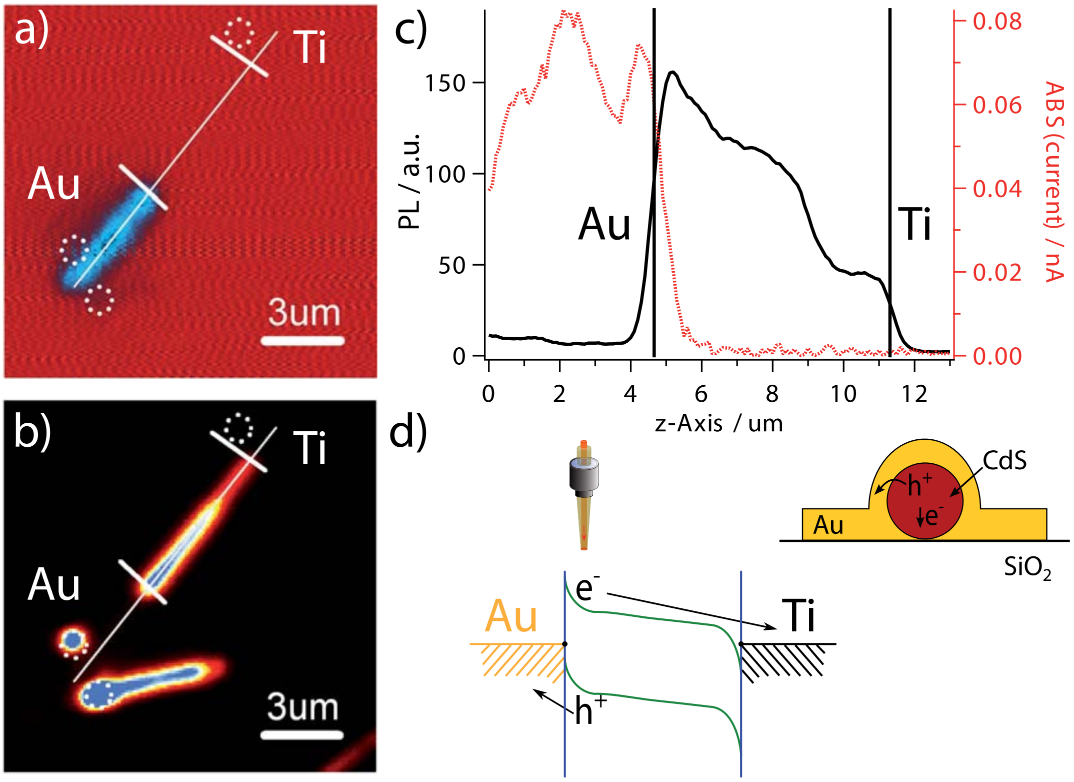

Figure 5.6: An Au-CdS-Ti device without bias. a) PC image and b) the respective PL. The dotted circles are short CdS particles which were used for orientation. c) Cross-sections of the PL (black solid line) and the PC (red dotted line) along the device. d) Corresponding band scheme: holes have an extremely low mobility and can only be collected where the band-bending is strongest. Electrons travel through the CdS wire and are collected at Ti.

the metal-semiconductor interface. The resulting Schottky contact favors the extraction of holes, while electrons encounter a barrier. The built-in electric field is sufficient to separate the electron-hole pairs, created by illumination, and to lead to a photocurrent. Similar results are obtained by SPCM in the Au-CdS-Ti device, as shown in figure 5.6 a, A corresponding PL image is displayed in fig. 5.6 b.

The images are complementary: PC is detected underneath the gold electrode, while the PL of the CdS is only collected between the electrodes. A cross-section (fig. 5.6 c) has been taken along the white line of the SPCM image (fig. 5.6 a) and the PL image (fig. 5.6 b). The sharp boundary between the covered and exposed parts of the CdS wire can be easily distinguished.

A major contribution to the photocurrent arises from the part of the wire located underneath the gold contact. Even though the electrode has a thickness of 80 nm, enough photons reach the CdS to create a measurable photocurrent.

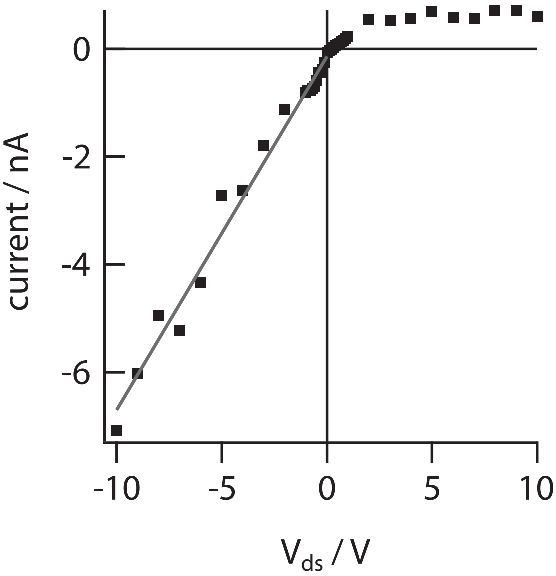

Figure 5.7: Photocurrent beneath the gold electrode at different bias. The red line is a linear fit for bias $V_{\mathrm{ds}} < 0\mathrm{V}$.

The built-in potential of the Schottky junction V_{Sch} can be described with the equation

$$V_{\mathrm{Sch}} = (\phi_{\mathrm{Au}} - \phi_{\mathrm{CdS}})/e = (\phi_{\mathrm{Au}} - \chi_{\mathrm{CdS}} - \phi_{\mathrm{n}})/e\,, \tag{5.2}$$

where ϕ_{Au} is the work function of the gold, ϕ_{CdS} is the Fermi level of the n-doped CdS, χ_{CdS} is the electron affinity of the CdS and ϕ_{n} is the depth of the Fermi level below the CdS conduction band edge. It can be calculated by $\phi_{\mathrm{n}} = k_{\mathrm{B}}T\ln(N_{\mathrm{c}}/n_{\mathrm{e}})$, with N_{c} the effective density of state in the conduction band ($N_{\mathrm{c}} \sim 2.44 \times 10^{18}\,\mathrm{cm}^{-3}$) and n_{e} the electron density of the CdS NW ($n_{\mathrm{e}} \sim 1 \times 10^{13}\,\mathrm{cm}^{-3}$)[81], which was estimated to be smaller than 0.1 eV[80]. This explains why the current does not extend to the lateral CdS-Au interface:

In principle, holes can be collected at the gold electrode, while electrons drift through the CdS towards the titanium (fig. 5.6 d). However, even though there is no evident barrier for both charge carriers, the band bending between the electrodes is not enough to separate the exciton. On the one hand, the potential in radial direction is expected to be much higher, since the space charge region is limited to the wire diameter. On the other hand, the contact has been highly n-doped due to Ar-ion bombardment. Both assertions support the experimental findings. In figure 5.7 the photocurrent is plotted versus the applied drain-source voltage. The open circuit voltage V_{oc} is around 0.2 V, the short circuit current I_{sc} is 65 pA, similar to other devices. Other parameters, such as the fill factor FF and the energy conversion efficiency η, were not calculated, as monochromatic light was used and the results are not comparable to standard conditions where the spectral distribution of the sun is assumed. For negative bias, where the gold potential is raised, ohmic behavior is observed. The red line is a linear fit and yields a resistivity of 140 MΩ. Applying a positive bias gives a typical diode I-V curve, with a saturation current of 72 pA. In this case, electrons have to tunnel into the gold through the Schottky barrier. Additionally, the hole transport in CdS is five times less efficient than electron transport[79].

5.3.2 Competitive Exciton Decay

To further elucidate the influence of the band structure on exciton recombination and decay, series of SPCM images with different drain-source bias V_{ds} were recorded (figure 5.8). Simultaneously, the corresponding fluorescence was detected. Cross-sections were taken along the wire axis and are denoted by a white line. The length of the line corresponds to the actual length of the CdS wire, as determined by AFM. Two cases can be distinguished for clarity: First, the potential of the gold has been raised, in relation to the titanium, with a negative bias (figure 5.9 a). For easier reading, the absolute values are plotted. A significant increase in current is observed close to the gold electrode, which partially extends into the wire, concurrently the PL decreases. Second, PC and the corresponding PL for a positive bias (Fermi energy of the Au is lowered in relation to Ti) can be seen in figure 5.9 b. For positive bias current increases close to the titanium and saturates. The modulation of the PL is comparatively low. For both cases three characteristic areas can be identified: Close to the gold

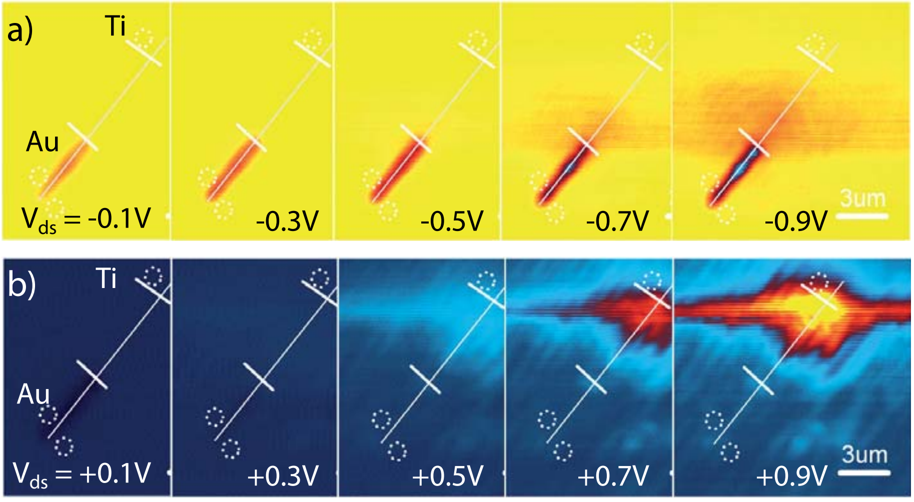

Figure 5.8: SPCM images for different bias. The bias increases/decreases in steps of 0.2 V from left to right. a) The Au potential is raised: holes are collected at Au, electrons at the Ti. b) With increased voltage holes are collected at Ti, electrons at Au.

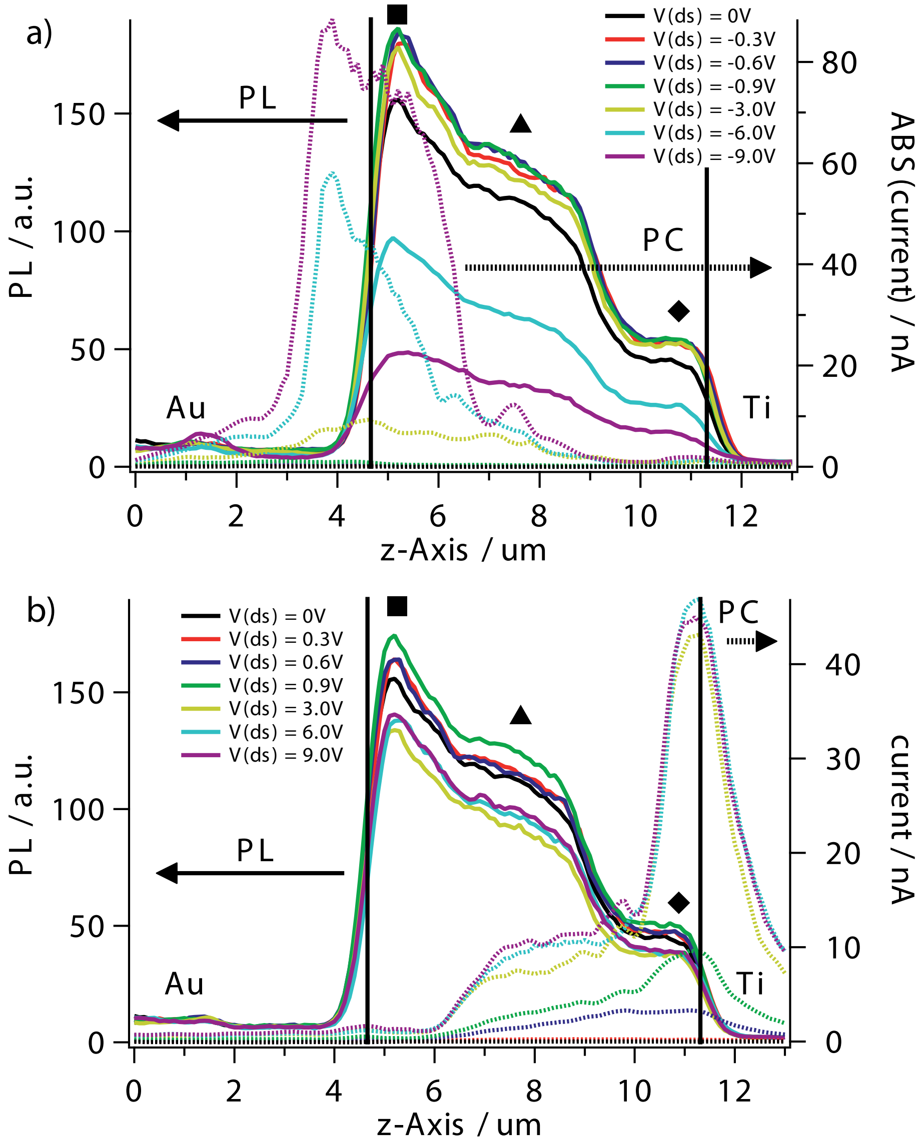

Figure 5.9: Cross-sections of PL (solid line) and PC (dotted line) for a) negative bias and b) positive bias. Vertical lines mark the edges of the Au and Ti electrode. At positions marked ■, ▲ and ♦, PL and PC are plotted vs. the bias V_{ds} in fig. 5.10

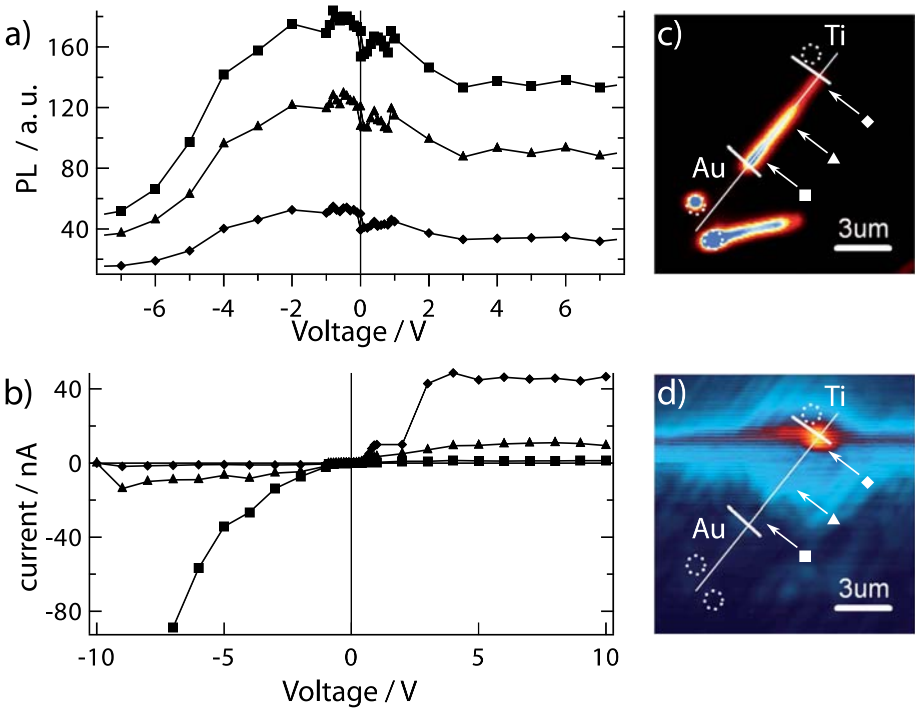

Figure 5.10: a) PL versus applied bias for three selected positions (marked ■, ▲ and ♦ in c) and d) and the cross-sections in fig. 5.9). b) Corresponding PC for the same positions. c) PL at V_{ds} 1 V and d) the corresponding SPCM image.

electrode is a short section of high PL, in the middle of the wire intermediate PL intensity is observed and close to the titanium the PL is the lowest. The PC response is structured in the same way and roughly follows the PL intensity steps.

For three distinct positions the PL and PC have been plotted versus the applied drain-source bias V_{ds} in figure 5.10, marked ■, ▲ and ♦, respectively. The PL intensity increases slightly for negative bias, up to a maximum at around -0.7 V, but declines below its initial intensity for stronger bias. Positive bias quenches PL until saturation is reached at $+3$ V. In general, the PC shows a similar trend: It increases as the PL drops close to the gold electrode (■). The saturation in photocurrent coincides with $+3$ V close to the titanium (♦). The center of the CdS wire (▲) occupies an intermediate position. However, a corresponding minimum in the photocurrent is missing. This suggests that there are at least two different radiative recombination channels for electron-hole pairs. One channel is directly related to the band curvature, which can be determined from the PC. The other channel is only weakly modulated by the applied drain-source bias V_{ds} and should therefore have a different origin.

The charge separation occurs in an electric field and the can be understood in terms of a simple band scheme, as sketched in figure 5.11. Illumination at the gold electrode leads to charge separation due to band alignment and

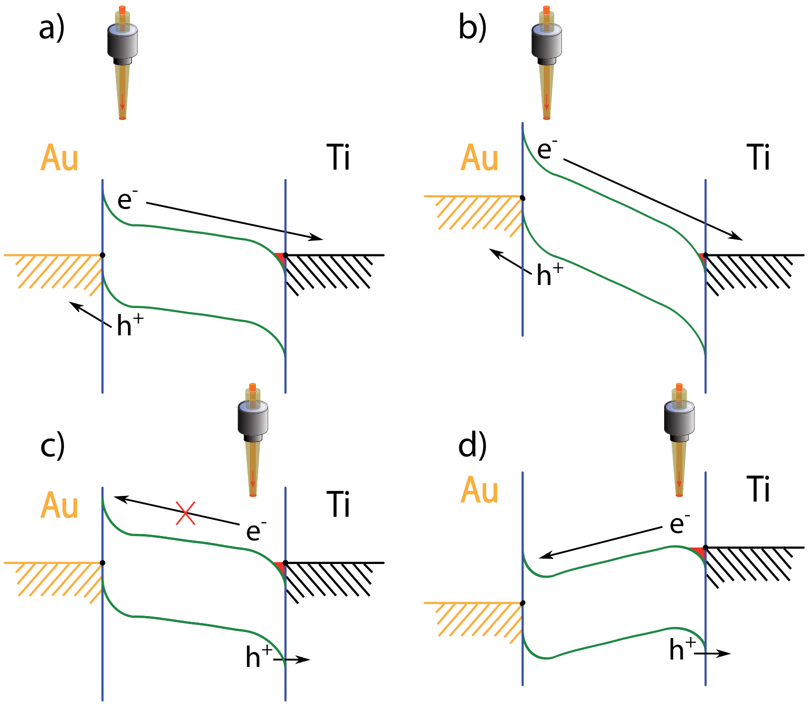

Figure 5.11: Simplified model for the band structure within a M_1SM_2 device: a) At zero bias only holes close to the gold can reach the electrode. b) Upon applying a bias, current flow is initiated. c) At the Ti electrode no photocurrent is observed as electrons would have to move up the conduction band to be collected at the gold electrode. d) When the potential of the gold electrode is lowered, electrons can move down the conduction band of the CdS.

Fermi level pinning. By lifting the gold electrode the band curvature increases and the charges can be separated more easily (fig. 5.11 b). As two metals with different work functions have been used, the potential decreases along the wire axis. This leads to a moderate photocurrent and a slightly quenched PL. High PL intensity is observed when the bands are flat. The reason for the change in curvature is not clear yet, but they occur in different regions for different wires.

Close to the titanium contact, holes are collected at the electrode. Electrons can diffuse through the wire if the gold electrode potential is lowered (fig. 5.11 d) with a positive bias. The charge separation also reduces the PL intensity. However, the effect is significantly lower since the ohmic contact provides an excess of electrons.

The relative position of the valence and conduction band can also be manipulated through an external field (figure 5.12). By applying a bias at the gate electrode, the valence and the conduction band of the CdS are shifted up ($V_G < 0V$, blue curve) or down ($V_G > 0V$, red curve). When the gold electrode is illuminated, a positive gate increases the band curvature. Therefore,

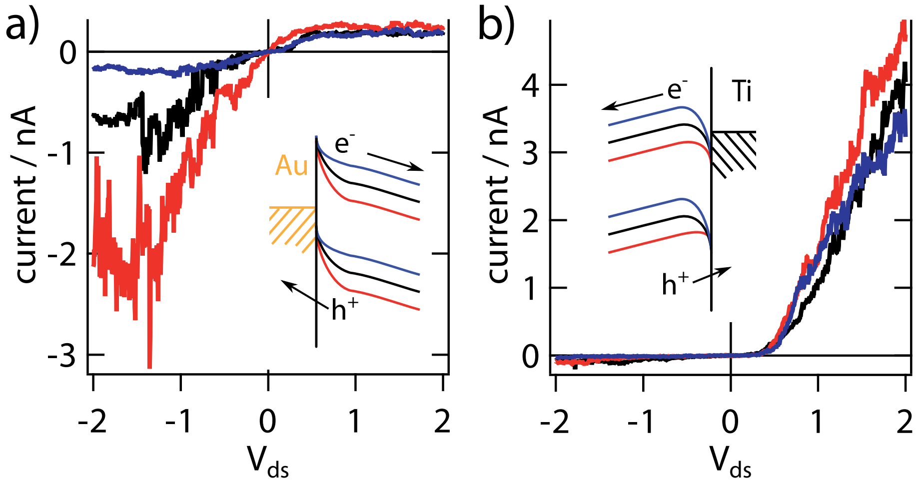

Figure 5.12: Modulation of the conductivity by applying a back-gate voltage: (black) $V_{gs} = 0V$, (red) $V_{gs} = +10V$ and (blue) $V_{gs} = -10V$ and a) illumination on gold; b) illumination on titanium. The gate has little influence on the titanium, since the bands are flat. At the gold contact the curvature can be changed and the device switched. The insets show the corresponding change in the semiconductor valence and conduction band. The bands move down for $V_{gs} > 0V$ and up for $V_{gs} > 0V$.

more electron-hole pairs can be separated before recombining and the current increases. In contrast, a negative gate flattens the bands and the current flow is reduced.

On the contrary, the gate has only little effect at the titanium contact. Since the holes are collected at this electrode, they experience no barrier. Shifting the CdS bands with an electric field does not influence the electron diffusion through the wire.

Other Au-CdS-Ti structures showed similar behavior. In fact, the highest PL intensity is not necessarily close to the gold electrode, as can be seen in figure 5.13. The fluorescence images indicate that high PL is observed where the bands are relatively flat, low PL correspond to a strong band curvature. The PL shown has been recorded at zero bias. Therefore, the potential drop along the wire is tentatively related to the intrinsic structure of the wire.

In summary, these experiments show an external manipulation of the conductivity in semiconductor nanowires by influencing the valence and conduction band curvature. However, the reasons for the intrinsic potential variation are not fully understood yet. In TEM images it can be seen that unprocessed wires are single crystalline[42]. Also, the deep-trap emission from these wires is much lower compared to the finished Au-CdS-Ti devices. Future experiments with Kelvin probe force microscopy and spectral analysis into the CdS PL at different bias should give more insight of the potential variations along the nanowires and their origin.

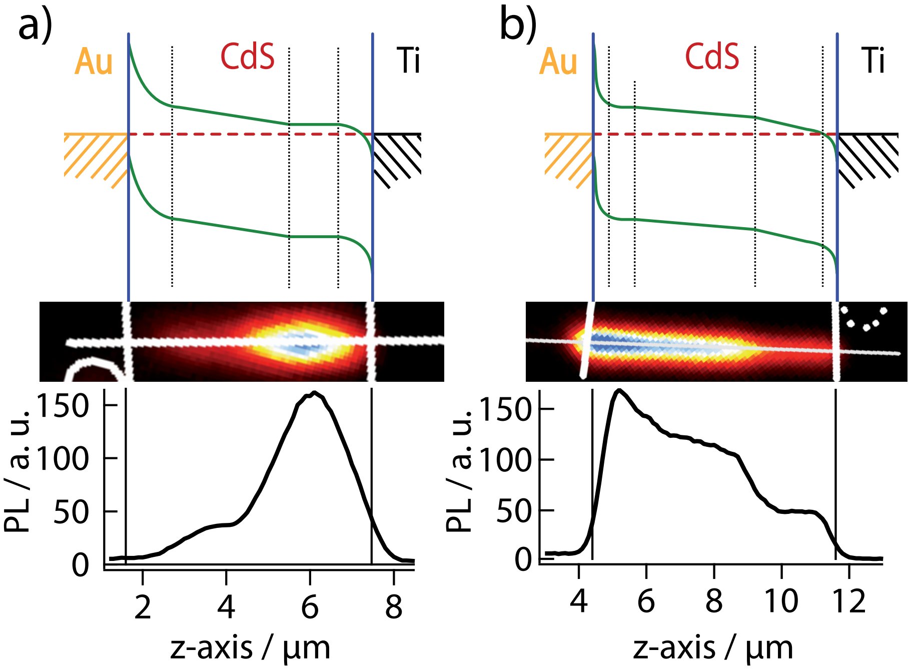

Figure 5.13: Band schemes (top) of different CdS wires with a modulation of the PL along their axis (middle) and the corresponding cross-sections. High PL intensity is detected at areas of flat bands, low PL indicates strong band curvature. Steps are developed when the band curvature changes.

6 Photovoltaics

In this chapter semiconductor nanocrystal-polymer heterojunction solar cells were investigated. These photovoltaic elements are used to improve organic semiconductor solar cells. Generally, polymer solar cells utilize the bulk-heterojunction approach, where a blend of conductive polymer and fullerene derivatives is used as a 'donor-acceptor' system to separate photoexcited electrons and holes [82–85]. However, most of the fullerene related molecules have poor extinction coefficients [84]. CdSe NCs, on the contrary, have a high absorption coefficient [86], which in addition can be tuned across the whole visible range of the solar spectrum [40,87]. Until today hybrid solar cells based on CdSe NCs achieved power conversion efficiencies of up to 3 % [88,89].

6.1 CdSe-P3HT Solar Cells

The fabrication process of a CdSe-polymer solar cell is shown in figure 6.1 a-f: First, a titanium electrode was defined by e-beam lithography and subsequent thermal evaporation of titanium. Then, the metal was partially thermally oxidized to TiO_2 at 400 °C. The oxide is a wide band gap semiconductor (see also figure 6.3), which acts as a hole blocking layer. Subsequently, a gold electrode was deposited near the titanium (fig. 6.1 d) and a CdSe NCs film was spin-coated on top of the metal structures (fig. 6.1 e). Finally, the nanocrystals were covered with P3HT, as sketched in fig. 6.1 f. An optical image of the device is shown in fig. 6.1 g with the inset representing an area of 25 × 25 µm. The titanium and gold electrodes have a variable spacing to study the diffusion of holes through the polymer.

Figure 6.2 a shows an exemplary current-voltage *I*-*V* characteristic of a hybrid solar cell without (black curve) and with illumination (red curve). The open circuit voltage V_{oc} of 0.7 V corresponds well to previously reported values [90,91]. The samples exhibited a slow degradation during illumination, even though all measurements were performed under a continuous nitrogen flow.

The band diagram of a CdSe-P3HT device is sketched in figure 6.3 with the respective bulk values of the titanium and gold work functions [76] and the valence and conduction bands of CdSe [92], TiO_2 [93] and P3HT [94]. In principle, after charge separation, electrons either diffuse to the TiO_2 or tunnel through

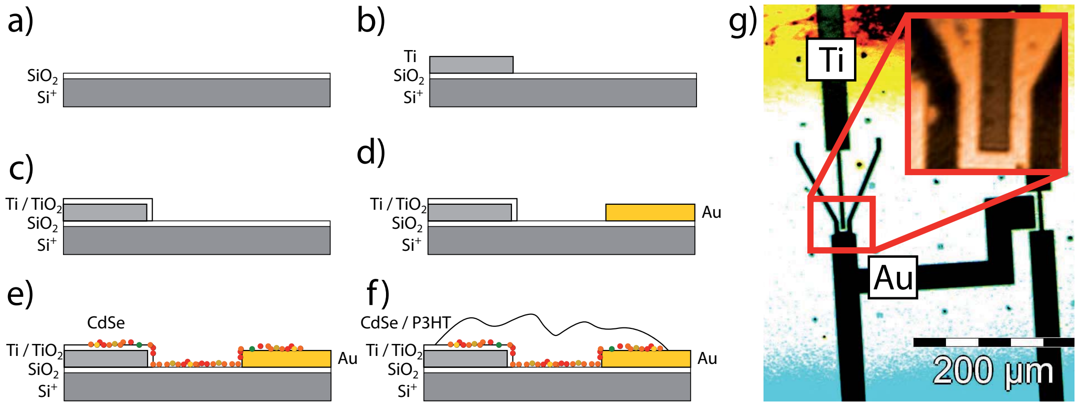

Figure 6.1: Schematics of the fabrication process of CdSe-P3HT photovoltaic devices. a) Electrodes are defined by lithography on a silicon substrate with an insulating oxide layer. b) Ti is evaporated, followed by c) thermal oxidation of Ti to TiO_2 to create a hole blocking layer. d) Au is deposited and e) CdSe is spin coated from a toluene solution. f) P3HT is spin coated on top in order to contact the Ti/CdSe with the Au electrode. g) Wide field image of the finished device. The Au and Ti electrodes are marked accordingly. The inset shows a false-color image of the active region of the device.

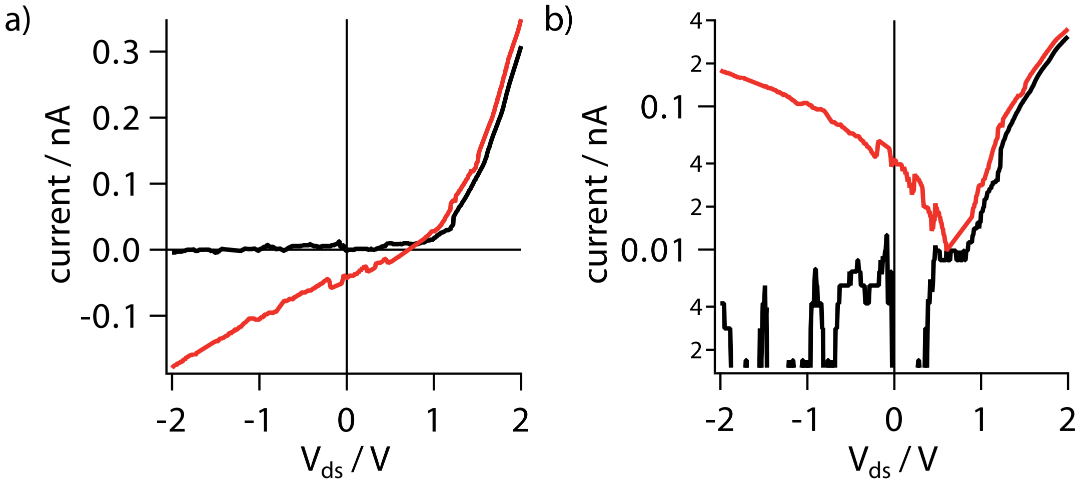

Figure 6.2: a) Current-voltage (I-V) characteristic of the CdSe-P3HT device in the dark (black) and with illumination (red). b) Same plot with a logarithmic scale

the oxide into the Ti electrode[96,97]. In contrast, holes move through the P3HT polymer to the Au electrode[98].

However, different mechanisms of charge separation are possible, as depicted in figure 6.4[95]. If photons are absorbed in the P3HT, charge separation can be achieved by electron transfer to the CdSe NC (fig. 6.4 a). Additionally, the entire exciton can be transferred to the NC, where, in turn, the hole diffuses back to the polymer (fig. 6.4 b). Thirdly, the exciton can be created in the CdSe whereas the hole decays to the P3HT (fig. 6.4 c). The relative positions of the energy levels of the NC and the conductive polymer influence the charge transfer in

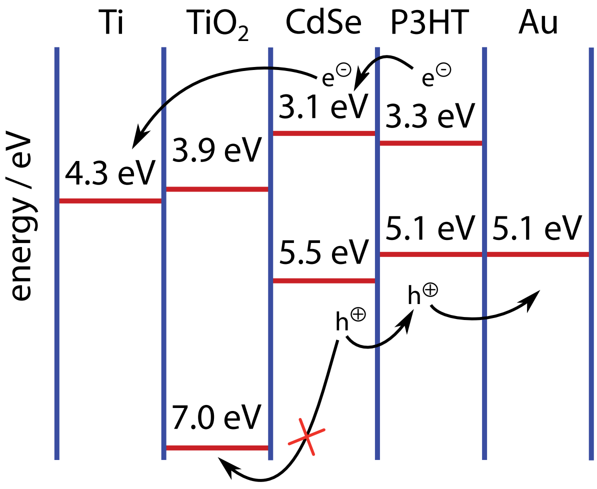

Figure 6.3: Band scheme of a CdSe-P3HT cell. Work functions and valence and conduction band energies correspond to the bulk values. Position of the CdSe, TiO_2 and P3HT bands were taken from Ref. 92–94. The exact position of the valence and conduction band depends on the NC size. In this case the band gap was assumed to be 1.9 eV. The current flow is indicated by the arrows.

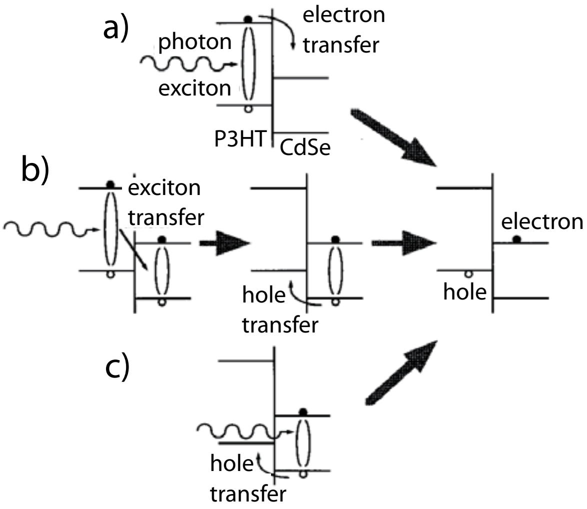

Figure 6.4: Exciton and charge transfer in a CdSe-P3HT device: a) Photons are absorbed in the polymer, followed by electron transfer onto the NC. b) Absorption in the polymer with exciton transfer onto the NC and subsequent hole transfer onto the polymer. c) Absorption in the NC, followed by hole transfer onto the polymer. Adopted from Ref. 95.

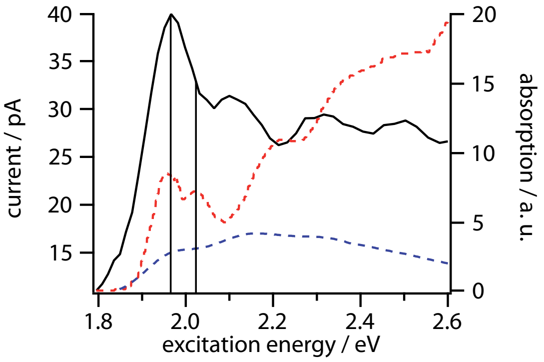

Figure 6.5: (—) Photoaction spectrum of the solar cell; (- - -) absorption of CdSe NCs; (- - -) absorption of a P3HT thin film.

this donor-acceptor system. For example, in ultra-small CdSe NCs route b) in fig.6.4 is not accessible since the band gap energy of the NC is larger than that of the polymer.

The photon absorption and charge transfer in the PV device was investigated by photoaction current spectroscopy (PACS). Thereby the photocurrent was measured at a fixed position of the sample, while continuously tuning the laser excitation energy. Peaks in the PACS represent a high contribution of the absorbed light to the photocurrent, troughs are an indication of either a reduced charge separation or a low absorption of the material. A typical PA spectrum as shown in figure 6.5 with a solid black curve. The red dashed curve corresponds to the absorption spectrum of CdSe NCs, the blue curve to the absorption of a P3HT thin film. The main photocurrent peak at ~1.9 eV corresponds to the band gap of the CdSe NCs used. This is a strong indication of the absorption occurring in the CdSe since the onset of the absorption of the P3HT film happens at slightly larger energies. The exciton is subsequently separated by a hole transfer to the polymer, while the electrons are collected at the titanium. At shorter excitation wavelengths the PA spectrum resembles the absorption curve of P3HT. Therefore the absorption of higher energetic light should be dominated by the polymer.

To further investigate the exciton dissociation process SPCM measurements were performed on the CdSe-P3HT devices. Complementary images of PL and PC are displayed in figure 6.6. In panel a) the combination of the PL and back-scattered light is shown. However, the light emitted from the sample is dominated by the fluorescence of CdSe NCs, as can be seen in the inset. Even though the investigated area is completely covered by CdSe and P3HT, photocurrent is only detected at the CdSe/TiO_2/Ti interface. The electrons can be injected from the CdSe into the TiO_2 [6,97,99], from where they are collected at the titanium. However, efficient collection of electrons further away from

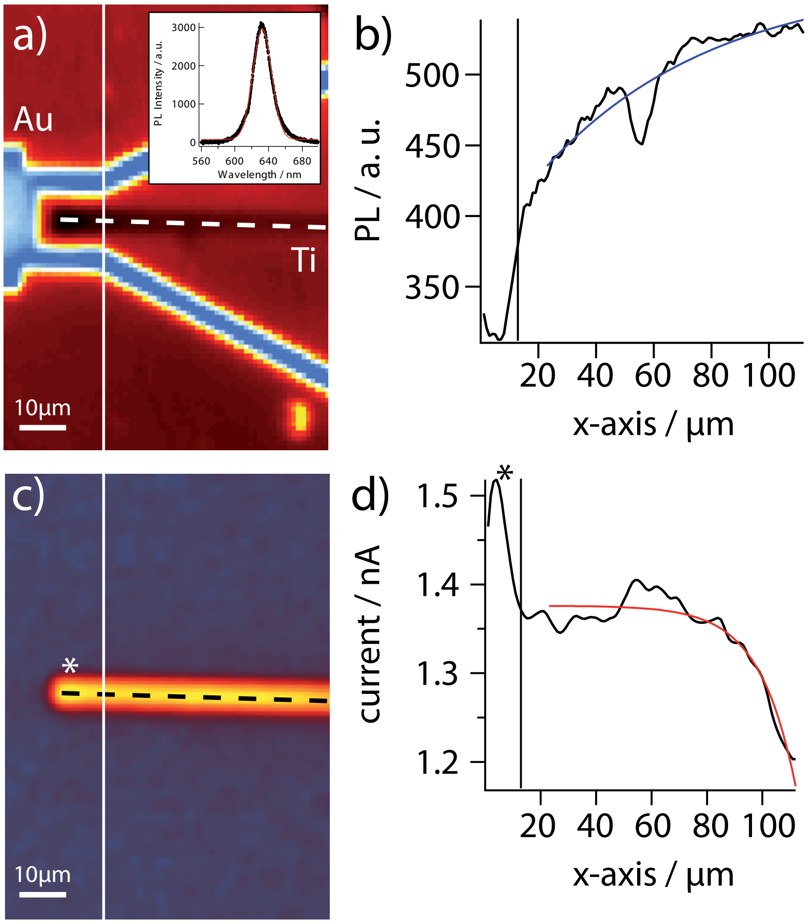

Figure 6.6: a) Confocal scan of the PV device. Excitation was at 488 nm, with a power of 200 nW. PL and back-scattered light were detected. The inset shows a spectrum of a random position on the substrate, which corresponds to CdSe fluorescence. c) SPCM image of the same area. b), d) Cross-section along the dotted lines in a) and c). The vertical lines correspond to the solid white lines, the $*$ denotes the same positions in c) and d). PC is only detected on top of the Ti electrode. A minimum in PL coincides with a maximum in PC, at the closest position to the Au counter electrode. The blue and red curves are exponential fits to experimental data.

the Ti electrode is prevented by hopping of charges from one CdSe NP to another[100].

Line profiles were taken along the dashed lines and are shown in fig. 6.6 b and d, respectively. A sharp decrease in PL is observed when the titanium electrode is in proximity to the gold electrode. Similarly, the SPCM image shows an increase of PC at the same position. Otherwise the PC decreases for larger distances from the gold electrode, while the PL increases. The PL quenching suggests that excitons are separated at the NC/polymer boundary[95]. However, since no external bias is applied in the PV cell, the built-in potential between the Ti and Au has to pull the charges apart. The increasing PL intensity with increasing inter-electrode distance suggests that the pull acting on electron-hole pairs lessens and that the charges have more time to recombine as the band-bending becomes shallower. Therefore not only the mobility of holes in the polymer determines the efficiency of a solar cell but also the steepness of the *quasi*-pn junction at the NC-polymer interface.

Overall, spatially resolved photocurrent was measured in a photovoltaic device with only a few NPs in the excitation spot and a successful transfer of the excited electron to the acceptor material was demonstrated. Since the absorption spectrum of the CdSe NCs does partially overlap with the PL spectrum of the P3HT, is it possible that at higher excitation energies either only the electron is transferred to the NC (preferred process) or if the entire exciton is transferred by Förster resonance energy transfer.

7 Summary & Outlook

In conclusion, a combination of optical and electrical measurements was used to explore the electronic band structure in one-dimensional nanostructures.

Individual CdSe NWs from colloidal synthesis were thoroughly characterized with different microscopy techniques. The optical band gap was determined from fluorescence spectra and was correlated with the wire diameter. The shift PL peak in CdSe NWs was explained by the quantization effects and the Coulomb attraction between the electron and the hole. In the future, low-temperature experiments should be performed to better resolve spectral features of the wire PL. Thereby it should be possible to probe shallow potential minima which remain hidden at room temperature. Particularly the influence of the wurtzite and zinc blende segments on the optical band gap should be detectable.

Optoelectrical measurements on CdS wires showed a strong connection between photocurrent and photoluminescence. Both originate from excitons which either recombine and emit light or are separated into free charges and contribute to an electric current. The exciton binding energy is an important factor for successfully dissociating electron-hole pairs and can be evaluated by a varying source-drain bias.

Hybrid structures composed of nanocrystals and a photoactive polymer were used to study the absorption of light in solar-cells. Photoaction spectroscopy with a high spatial resolution revealed different types of absorption processes in the photosensitizer and the conducting material. More detailed investigations at the interface of these donor-acceptor systems will allow to further improve the efficiency of heterojunction solar-cells.

Bibliography

[1] C. N. R. Rao, A. Mueller, and A. Ceetham. *The Chemistry of Nanomaterials* (Wiley-VCH, 2004).

[2] D. V. Talapin, A. L. Rogach, A. Kornowski, M. Haase, and H. Weller. *Highly Luminescent Monodisperse CdSe and CdSe/ZnS Nanocrystals Synthesized in a Hexadecylamine-Trioctylphosphine Oxide-Trioctylphospine Mixture*. Nano Letters **1**(4), 207 (2001).

[3] G. Yu and C. M. Lieber. *Assembly and Integration of Semiconductor Nanowires for Functional Nanosystems*. Pure and Applied Chemistry **82**(12), 2295 (2010).

[4] R. Agarwal. *Heterointerfaces in Semiconductor Nanowires*. Small **4**(11), 1872 (2008).

[5] K. C. Chiang, W.-Y. Wu, and J.-M. Ting. *Enhanced Lateral Growth of Zinc Oxide Nanowires on Sensor Chips*. Journal of the American Ceramic Society **94**(3), 713 (2011).

[6] J. C. Lee, W. Lee, S. H. Han, T. G. Kim, and Y. M. Sung. *Synthesis of Hybrid Solar Cells Using CdS Nanowire Array Grown on Conductive Glass Substrates*. Electrochemistry Communications **11**(1), 231 (2009).

[7] A. Javey, S. Nam, R. S. Friedman, H. Yan, and C. M. Lieber. *Layer-by-Layer Assembly of Nanowires for Three-Dimensional, Multifunctional Electronics*. Nano Letters **7**(3), 773 (2007).

[8] B. Timko, T. Cohen-Karni, Q. Qing, B. Tian, and C. Lieber. *Design and Implementation of Functional Nanoelectronic Interfaces With Biomolecules, Cells, and Tissue Using Nanowire Device Arrays*. IEEE Transactions on Nanotechnology **9**(3), 269 (2010).

[9] M. Kuno. *An overview of solution-based semiconductor nanowires: synthesis and optical studies*. Phys. Chem. Chem. Phys. **10**, 620 (2008).

[10] J. W. Grebinski, K. L. Hull, J. Zhang, T. H. Kosel, and M. Kuno. *Solution-Based Straight and Branched CdSe Nanowires*. Chemistry of Materials **16**(25), 5260 (2004).

[11] Z. Li, A. Kornowski, A. Myalitsin, and A. Mews. *Formation and Function of Bismuth Nanocatalysts for the Solution-Liquid-Solid Synthesis of CdSe Nanowires*. Small **4**(10), 1698 (2008).

[12] J. Puthussery, T. H. Kosel, and M. Kuno. *Facile Synthesis and Size Control of II-VI Nanowires Using Bismuth Salts*. Small **5**(10), 1112 (2009).

[13] F. D. Wang and W. E. Buhro. *An Easy Shortcut Synthesis of Size-Controlled Bismuth Nanoparticles and Their Use in the SLS Growth of High-Quality Colloidal Cadmium Selenide Quantum Wires*. Small **6**(4), 573 (2010).

[14] H. Yu, J. B. Li, R. A. Loomis, P. C. Gibbons, L. W. Wang, and W. E. Buhro. *Cadmium Selenide Quantum Wires and the Transition from 3D to 2D Confinement*. Journal of the American Chemical Society **125**(52), 16168 (2003).

[15] V. V. Protasenko, K. L. Hull, and M. Kuno. *Disorder-Induced Optical Heterogeneity in Single CdSe Nanowires*. Advanced Materials **17**(24), 2942 (2005).

[16] I. Robel, B. A. Bunker, P. V. Kamat, and M. Kuno. *Exciton Recombination Dynamics in CdSe Nanowires: Bimolecular to Three-Carrier Auger Kinetics*. Nano Letters **6**(7), 1344 (2006).

[17] J. J. Glennon, R. Tang, W. E. Buhro, R. A. Loomis, D. A. Bussian, H. Htoon, and V. I. Klimov. *Exciton Localization and Migration in Individual CdSe Quantum Wires at Low Temperatures*. Physical Review B **80**(8), 081303 (2009).

[18] J. J. Glennon, R. Tang, W. E. Buhro, and R. A. Loomis. *Synchronous Photoluminescence Intermittency (Blinking) Along Whole Semiconductor Quantum Wires*. Nano Letters **7**(11), 3290 (2007).

[19] J. J. Glennon, W. E. Buhro, and R. A. Loomis. *Simple Surface-Trap-Filling Model for Photoluminescence Blinking Spanning Entire CdSe Quantum Wires*. Journal of Physical Chemistry C **112**(13), 4813 (2008).

[20] V. Biju, R. Kanemoto, Y. Matsumoto, S. Ishii, S. Nakanishi, T. Itoh, Y. Baba, and M. Ishikawa. *Photoinduced Photoluminescence Variations of CdSe Quantum Dots in Polymer Solutions*. Journal of Physical Chemistry C **111**(22), 7924 (2007).

[21] S. Wang, C. Querner, M. D. Fischbein, L. Willis, D. S. Novikov, C. H. Crouch, and M. Drndic. *Blinking Statistics Correlated with Nanoparticle Number*. Nano Letters **8**(11), 4020 (2008).

[22] A. M. Mintairov, J. Herzog, M. Kuno, and J. L. Merz. *Near-Field Scanning Optical Microscopy of Colloidal CdSe Nanowires*. Physica Status Solidi (b) **247**(6), 1416 (2010).

[23] *International Technology Roadmap for Semiconductors* (2005). http://www.itrs.net/Links/2005ITRS/ExecSum2005.pdf.

[24] P. V. Kamat. *Quantum Dot Solar Cells. Semiconductor Nanocrystals as Light Harvesters*. The Journal of Physical Chemistry C **112**(48), 18737 (2008).

[25] V. Subramanian, E. E. Wolf, and P. V. Kamat. *Catalysis with TiO_2/Gold Nanocomposites. Effect of Metal Particle Size on the Fermi Level Equilibration*. Journal of the American Chemical Society **126**(15), 4943 (2004).

[26] M. T. Sheldon, P.-E. Trudeau, T. Mokari, L.-W. Wang, and A. P. Alivisatos. *Enhanced Semiconductor Nanocrystal Conductance via Solution Grown Contacts*. Nano Letters **9**(11), 3676 (2009).

[27] M. Murayama and T. Nakayama. *Chemical Trend of Band Offsets at Wurtzite/Zinc-Blende Heterocrystalline Semiconductor Interfaces*. Physical Review B **49**(7), 4710 (1994).

[28] S.-H. Wei and S. B. Zhang. *Structure Stability and Carrier Localization in CdX (X=S, Se, Te) Semiconductors*. Physical Review B **62**(11), 6944 (2000).

[29] J. Li and L.-W. Wang. *Shape Effects on Electronic States of Nanocrystals*. Nano Letters **3**(10), 1357 (2003).

[30] A. Gómez-Rodríguez, L. M. Beltrán-del Río, and R. Herrera-Becerra. *SimulaTEM: Multislice Simulations for General Objects*. Ultramicroscopy **110**(2), 95 (2010).

[31] D. Vogel, P. Krueger, and J. Pollmann. *Self-Interaction and Relaxation-Corrected Pseudopotentials for II-VI Semiconductors*. Phys. Rev. B **54**(8), 5495 (1996).

[32] D. J. BenDaniel and C. B. Duke. *Space-Charge Effects on Electron Tunneling*. Physical Review **152**(2), 683 (1966).

[33] A. F. Slachmuylders, B. Partoens, W. Magnus, and F. M. Peeters. *Exciton States in Cylindrical Nanowires*. Journal of Physics: Condensed Matter **18**(16), 3951 (2006).

[34] A. F. Slachmuylders, B. Partoens, W. Magnus, and F. M. Peeters. *Dielectric Mismatch Effect on the Exciton States in Cylindrical Nanowires*. Physical Review B **74**(23), 235321 (2006).

[35] A. Klein. *Halbleitergrenzflächen, Script* (TU Darmstadt, Darmstadt, 2006).

[36] E. Becquerel. *Mémoire sur les effets électriques produits sous l'influence des rayons solaires*. Comptes Rendus **9**, 561 (1839).

[37] D. M. Chapin, C. S. Fuller, and G. L. Pearson. *A New Silicon p-n Junction Photocell for Converting Solar Radiation into Electrical Power*. Journal of Applied Physics **25**(5), 676 (1954).

[38] D. C. Reynolds, G. Leies, L. L. Antes, and R. E. Marburger. *Photovoltaic Effect in Cadmium Sulfide*. Physical Review **96**(2), 533 (1954).

[39] M. Scolari. *Local Optical and Electronic Properties of Individual Single Wall Carbon Nanotubes*. Ph.D. thesis, University of Siegen (2007).

[40] R. Xie, U. Kolb, J. Li, T. Basche, and A. Mews. *Synthesis and Characterization of Highly Luminescent CdSe-Core CdS/Zn0.5Cd0.5S/ZnS Multishell Nanocrystals*. Journal of the American Chemical Society **127**(20), 7480 (2005).

[41] Z. Li, O. Kurtulus, N. Fu, Z. Wang, A. Kornowski, U. Pietsch, and A. Mews. *Controlled Synthesis of CdSe Nanowires by Solution-Liquid-Solid Method*. Advanced Functional Materials **19**(22), 3650 (2009).

[42] H. J. Boettcher. *Synthesis and Characterization of Group II-VI Semiconductor Nanowires*. Ph.D. thesis, Ecole Polytechnique Federale de Lausanne (2010).

[43] J. Kong, A. M. Cassell, and H. Dai. *Chemical Vapor Deposition of Methane for Single-Walled Carbon Nanotubes*. Chemical Physics Letters **292**(4-6), 567 (1998).

[44] R. E. Smalley, Y. Li, V. C. Moore, B. K. Price, R. Colorado, H. K. Schmidt, R. H. Hauge, A. R. Barron, and J. M. Tour. *Single Wall Carbon Nanotube Amplification: En Route to a Type-Specific Growth Mechanism*. Journal of the American Chemical Society **128**(49), 15824 (2006).

[45] W. R. Bennett and A. M. Javan. *Gas Optical Laser* (1964). patent.

[46] J. Hecht. *The Laser Guidebook* (Mcgraw Hill Book Co, 1992), 2nd edition.

[47] Fianium. *Source of Optical Supercontinuum Generation*. patent.

[48] H. B. Manning, G. T. Kennedy, D. M. Owen, D. M. Grant, A. I. Magee, M. A. A. Neil, Y. Itoh, C. Dunsby, and P. M. French. *A Compact, Multidimensional Spectrofluorometer Exploiting Supercontinuum Generation*. Journal of Biophotonics **1**(6), 494 (2008).

[49] Perkin Elmer Optoelectronics. *Single Photon Counting Module* (2005). manual.

[50] C. Trottier, M. Davies, H. Dautet, M. Wabuyele, S. A. Soper, A. N. Kapanidis, T. Lacoste, and S. Weiss. *Single Photon-Counting Technology* (2004).

[51] Intevac, Inc. *MOSIR 950 User Manual*.

[52] M. Knoll and E. Ruska. *Das Elektronenmikroskop*. Zeitschrift fuer Physik **78**, 318 (1932).

[53] D. Williams and B. Carter. *Transmission Electron Microscopy : A Textbook for Materials Science* (Plenum Press, 1996).

[54] Y. Ebenstein, E. Nahum, and U. Banin. *Tapping Mode Atomic Force Microscopy for Nanoparticle Sizing: Tip-Sample Interaction Effects*. Nano Letters **2**(9), 945 (2002).

[55] M. Nirmal, B. O. Dabbousi, M. G. Bawendi, J. J. Macklin, J. K. Trautman, T. D. Harris, and L. E. Brus. *Fluorescence intermittency in single cadmium selenide nanocrystals*. Nature **383**, 802 (1996).

[56] O. Madelung, U. Rössler, and M. Schulz, editors. *Cadmium Selenide (CdSe) Effective masses, Fröhlich Coupling Constant, Hexagonal Modification*, *Landolt-Börnstein - Group III Condensed Matter*, volume 41B (SpringerMaterials - The Landolt-Börnstein Database).

[57] O. Madelung, U. Rössler, and M. Schulz, editors. *Cadmium Selenide (CdSe) Electronic Properties, Zincblende Modification*, *Landolt-Börnstein - Group III Condensed Matter*, volume 41B (SpringerMaterials - The Landolt-Börnstein Database).

[58] A. H. Nethercot. *Prediction of Fermi Energies and Photoelectric Thresholds Based on Electronegativity Concepts*. Physical Review Letters **33**(18), 1088 (1974).

[59] L. E. Brus. *Electron-Electron and Electron-Hole Interactions in Small Semiconductor Crystallites: The Size Dependence of the Lowest Excited Electronic State*. The Journal of Chemical Physics **80**, 4403 (1984).

[60] G. Bastard. *Wave Mechanics Applied to Semiconductor Heterostructures*. Monographies de physique (Les éditions de physiquue, Paris, 1992).

[61] O. Madelung, U. Rössler, and M. Schulz, editors. *Cadmium Selenide (CdSe) Dielectric Constants, Landolt-Börnstein - Group III Condensed Matter*, volume 41B (SpringerMaterials - The Landolt-Börnstein Database).

[62] O. Madelung, U. Rössler, and M. Schulz, editors. *Cadmium Selenide (CdSe) Energy Gaps, Hexagonal Modification, Landolt-Börnstein - Group III Condensed Matter*, volume 41B (SpringerMaterials - The Landolt-Börnstein Database).

[63] J. Li and L.-W. Wang. *Band-Structure-Corrected Local Density Approximation Study of Semiconductor Quantum Dots and Wires*. Physical Review B **72**(12), 125325 (2005).

[64] H. Yu, J. Li, R. A. Loomis, L.-W. Wang, and W. E. Buhro. *Two- Versus Three-Dimensional Quantum Confinement in Indium Phosphide Wires and Dots*. Nature Materials **2**, 517 (2003).

[65] F. D. Wang, H. Yu, S. H. Jeong, J. M. Pietryga, J. A. Hollingsworth, P. C. Gibbons, and W. E. Buhro. *The Scaling of the Effective Band Gaps in Indium-Arsenide Quantum Dots and Wires*. ACS Nano **2**(9), 1903 (2008).

[66] N. Fu, Z. Li, A. Myalitsin, M. Scolari, R. T. Weitz, M. Burghard, and A. Mews. *One-Dimensional Heterostructures of Single-Walled Carbon Nanotubes and CdSe Nanowires*. Small **6**(3), 376 (2010).

[67] S. Reich, C. Thomsen, and J. Maultzsch. *Carbon Nanotubes* (Wiley, Weinheim, Germany, 2004).

[68] P. Villars, A. Prince, and H. Okamoto. *Handbook of Ternary Alloy Phase Diagrams*, volume 5 (Wiley, Weinheim, Germany, 1995).

[69] J. B. Hannon, S. Kodambaka, F. M. Ross, and R. M. Tromp. *The Influence of the Surface Migration of Gold on the Growth of Silicon Nanowires*. Nature **440**, 69 (2006).

[70] E. J. Schwalbach and P. W. Voorhees. *Phase Equilibrium and Nucleation in VLS-Grown Nanowires*. Nano Letters **8**, 3739 (2008).

[71] A. L. Efros and M. Rosen. *Random Telegraph Signal in the Photoluminescence Intensity of a Single Quantum Dot*. Physical Review Letters **78**, 1110 (1997).

[72] C. J. Barrelet, Y. Wu, D. C. Bell, and C. M. Lieber. *Synthesis of CdS and ZnS Nanowires Using Single-Source Molecular Precursors*. Journal of the American Chemical Society **125**(38), 11498 (2003).

[73] W. Qingqing, X. Gang, and H. Gaorong. *Solvothermal Synthesis and Characterization of Uniform CdS Nanowires in High Yield*. Journal of Solid State Chemistry **178**(9), 2680 (2005).

[74] L. V. Titova, T. B. Hoang, H. E. Jackson, L. M. Smith, J. M. Yarrison-Rice, J. L. Lensch, and L. J. Lauhon. *Low-Temperature Photoluminescence Imaging and Time-Resolved Spectroscopy of Single CdS Nanowires*. Applied Physics Letters **89**(5), 053119 (2006).

[75] F. Wu, J. Z. Zhang, R. Kho, and R. K. Mehra. *Radiative and Nonradiative Lifetimes of Band Edge States and Deep Trap States of CdS Nanoparticles Determined by Time-Correlated Single Photon Counting*. Chemical Physics Letters **330**(3-4), 237 (2000).

[76] S. M. Sze and K. K. Ng. *Physics of Semiconductor Devices* (Wiley-Interscience, 2006).

[77] Y. Gu and L. J. Lauhon. *Space-Charge-Limited Current in Nanowires Depleted by Oxygen Adsorption*. Applied Physics Letters **89**(14), 143102 (2006).

[78] J. An, K. Xue, W. Xie, Q. Li, and J. Xu. *Effects of an Oxygen Environment on the Electrical Properties of a Single CdS Nanobelt Device*. Nanotechnology **22**(13), 135702 (2011).

[79] Y. Gu, J. P. Romankiewicz, J. K. David, J. L. Lensch, and L. J. Lauhon. *Quantitative Measurement of the Electron and Hole Mobility-Lifetime Products in Semiconductor Nanowires*. Nano Letters **6**(5), 948 (2006).

[80] Y. Ye, L. Dai, P. C. Wu, C. Liu, T. Sun, R. M. Ma, and G. G. Qin. *Schottky Junction Photovoltaic Devices Based on CdS Single Nanobelts*. Nanotechnology **20**(37), 375202 (2009).

[81] P. C. Wu, R. M. Ma, C. Liu, T. Sun, Y. Ye, and L. Dai. *High-Performance CdS Nanobelt Field-Effect Transistors with High-κ* HfO_2 *Top-Gate Dielectrics*. J. Mater. Chem. **19**, 2125 (2009).

[82] S. E. Shaheen, D. S. Ginley, and G. E. Jabbour. *Organic-Based Photovoltaics Toward Low-Cost Power Generation*. MRS Bulletin **30**(1), 10 (2005).

[83] M. C. Scharber, D. Wuhlbacher, M. Koppe, P. Denk, C. Waldauf, A. J. Heeger, and C. L. Brabec. *Design Rules for Donors in Bulk-Heterojunction Solar Cells - Towards 10 % Energy-Conversion Efficiency*. Advanced Materials **18**(6), 789 (2006).

[84] S. Cook, R. Katoh, and A. Furube. *Ultrafast Studies of Charge Generation in PCBM:P3HT Blend Films Following Excitation of the Fullerene PCBM*. Journal of Physical Chemistry C **113**(6), 2547 (2009).

[85] S. Cook, H. Ohkita, Y. Kim, J. J. Benson-Smith, D. D. C. Bradley, and J. R. Durrant. *A Photophysical Study of PCBM Thin Films*. Chemical Physics Letters **445**(4-6), 276 (2007).

[86] W. W. Yu, L. Qu, W. Guo, and X. Peng. *Experimental Determination of the Extinction Coefficient of CdTe, CdSe, and CdS Nanocrystals*. Chemistry of Materials **15**(14), 2854 (2003).

[87] A. P. Alivisatos. *Perspectives on the Physical Chemistry of Semiconductor Nanocrystals*. Journal of Physical Chemistry **100**(31), 13226 (1996).

[88] S. Kumar and G. D. Scholes. *Colloidal Nanocrystal Solar Cells*. Microchimica Acta **160**(3), 315 (2008).

[89] D. J. Milliron, I. Gur, and A. P. Alivisatos. *Hybrid Organic - Nanocrystal Solar Cells*. MRS Bulletin **30**(1), 41 (2005).

[90] F. Zutz, I. Lokteva, N. Radychev, J. Kolny-Olesiak, I. Riedel, H. Borchert, and J. Parisi. *Study of the Influence of the Cd and Se Precursor Ratio During the Synthesis of CdSe Nanocrystals on the Performance of CdSe/P3HT Hybrid Solar Cells*. Physica Status Solidi a **206**(12), 2700 (2009).

[91] W. U. Huynh, J. J. Dittmer, N. Teclemariam, D. J. Milliron, A. P. Alivisatos, and K. W. J. Barnham. *Charge Transport in Hybrid Nanorod-Polymer Composite Photovoltaic Cells*. Phys. Rev. B **67**(11), 115326 (2003).

[92] *Landoldt-Börnstein Database* (Springer-Verlag, Heidelberg, 2011).

[93] J. W. Yoon, T. Sasaki, and N. Koshizaki. *Dispersion of Nanosized Noble Metals in* TiO_2 *Matrix and Their Photoelectrode Properties*. Thin Solid Films **483**, 276 (2005).

[94] J. C. Nolasco, R. Cabre, J. Ferre-Borrull, L. F. Marsal, M. Estrada, and J. Pallares. *Extraction of Poly (3-hexylthiophene) (P3HT) Properties from Dark Current Voltage Characteristics in a P3HT n-Crystalline-Silicon Solar Cell*. Journal of Applied Physics **107**, 044505 (2010).

[95] N. C. Greenham, X. Peng, and A. P. Alivisatos. *Charge Separation and Transport in Conjugated-Polymer/Semiconductor-Nanocrystal Composites Studied by Photoluminescence Quenching and Photoconductivity*. Phys. Rev. B **54**(24), 17628 (1996).

[96] P. Yu, K. Zhu, A. G. Norman, S. Ferrere, A. J. Frank, and A. J. Nozik. *Nanocrystalline* TiO_2 *Solar Cells Sensitized with InAs Quantum Dots*. The Journal of Physical Chemistry B **110**(50), 25451 (2006).

[97] I. Robel, V. Subramanian, M. Kuno, and P. V. Kamat. *Quantum Dot Solar Cells. Harvesting Light Energy with CdSe Nanocrystals Molecularly Linked to Mesoscopic* TiO_2 *Films*. Journal of the American Chemical Society **128**(7), 2385 (2006).

[98] Z. Bao, A. Dodabalapur, and A. J. Lovinger. *Soluble and Processable Regioregular Poly(3-Hexylthiophene) for Thin Film Field-Effect Transistor Applications with High Mobility*. Appl. Phys. Lett. **69**(26), 4108 (1996).

[99] D. Liu and P. V. Kamat. *Electrochemical Rectification in CdSe +* TiO_2 *Coupled Semiconductor Films*. Journal of Electroanalytical Chemistry **347**(1-2), 451 (1993).

[100] D. S. Ginger and N. C. Greenham. *Charge Injection and Transport in Films of CdSe Nanocrystals* **87**(3), 1361 (2000).

Acknowledgements

This thesis would not have been completed in this way without the input of many people.
First of all I would like to thank Prof. Dr. Alf Mews for giving me the great opportunity to work in his group. He taught me a lot.
I am very grateful to Dr. Tobias Kipp and Dr. Christian Strelow for the theoretical calculations on the CdSe nanowires, which allowed to interpret the experimental data.
Many samples changed hands in the last four years. Therefore I would like to acknowledge the people who provided the samples for me to work with:
Dr. Zhen Li and Zhe Wang for the CdSe nanowires.
Dr. Nan Fu for the CdSe-Carbon Nanotube hybrids.
Dr. Jens Böttcher for the CdS nanowires.
Thomas Dufaux from the Max-Planck Institute of Solid State Research for preparing the optoelectric devices (CdS photodetectors and CdSe-P3HT solar cells).

I am also very thankful to
Jan Flügge for his technical support.
Andreas Kornowski for the high resolution TEM images.
Igor Kogut for the TEM simulations.

I could rely on many students to try out new (and also some old) projects. Therefore I would like to thank
André Rosehr, Lukas Mateki, Jana Gerber, Michael Neumann, Max Völker, Aina Reich and Dino Behn.

For careful proof reading and moral support I want to thank:
Sandra Flessau, Jana Gerber, Jens Böttcher, Sebastian Schäfer and Nadine Bohn.

I am very grateful for the support my family gave me. My mother Larissa, my father Vladimir, my brother Aleksej and Dela.

Hazardous Materials

Substance	Hazard symbol	R-phrases	S-phrases
Selenium	T	23/25-33-53	20/21-28-45-61
Tributylphosphine	F, C	17-21/22-34	17-26-36/37/39-43-45
Cadmium oxide	N,T+	45-26-48/23/25-68-50/53-62-63	53-45-61-60
Tetradecylphosphonic acid		36/37/38	26-36/37/39
Trioctylphosphine oxide	Xn	38-41	26-39
Octadecylamine	Xn	36/37/38	26-36
Hexane	F,Xn,N	11-38-48/20-62-65-67-51/53	9-16-29-33-36/37-61
Methanol	F,T	11-23/24/25-39/23/24/25	7-16-36/37-45
Oleic acid	Xn	38	
Octadecene	Xn	65-53	62
Sulfur	F	11	16-26
Trichloromethane	Xn	22-38-40-48/20/22	36/37
Dichloromethane	Xn	40	23-24/25-36/37
N-Methyl-2-pyrrolidon	T	61-36/37/38	53-45
Acetone	F,Xn	11-36-66-67	9-16-26-46
Isopropanol	F,Xn	11-36-67	7-16-24/25-26
Tellurium	T	25	45
Trioctylphosphine	C	34	26-36/37/39-45
Cyclohexane	F,Xn,N	11-38-51/53-65-67	9-16-33-61-62
Ammonia	T,N	10-23-34-50	9-16-26-36/37/39-45-61
Ethanol	F	11	7-16
3-(Trihydroxysilyl)-propyl methylphosphonate, monosodium salt solution	Xn	20/21/22-20/21/22	20/21/22
Chloroauric acid	C	34-43	26-36/37/39-45

Sulfuric acid	C	35	26-30-45
Hydrogen peroxide	Xn	22-41	26-39
1, 2-Ethanedithiol	T	10-23/24/25-36	26-36/37-45
Toluene	F,Xn	11-38-48/20-63-65-67	36/37-62-46

Hazard symbols

C	corrosive
E	explosive
F+	extremely flammable
F	highly flammable
N	dangerous to the environment
O	oxidizing
T+	very toxic
T	toxic
Xi	irritant
Xn	harmful

Risk (R-) and safety precaution (S-) phrases

R-Phrases

R1: Explosive when dry
R2: Risk of explosion by shock, friction fire or other sources of ignition
R3: Extreme risk of explosion by shock friction, fire or other sources of ignition
R4: Forms very sensitive explosive metallic compounds
R5: Heating may cause an explosion
R6: Explosive with or without contact with air
R7: May cause fire
R8: Contact with combustible material may cause fire
R9: Explosive when mixed with combustible material
R10: Flammable
R11: Highly flammable
R12: Extremely flammable
R13: Extremely flammable liquefied gas
R14: Reacts violently with water
R15: Contact with water liberates highly flammable gases
R16: Explosive when mixed with oxidizing substances
R17: Spontaneously flammable in air
R18: In use, may form flammable/explosive vapor-air mixture
R19: May form explosive peroxides
R20: Harmful by inhalation
R21: Harmful in contact with skin
R22: Harmful if swallowed
R23: Toxic by inhalation
R24: Toxic in contact with skin
R25: Toxic if swallowed
R26: Very toxic by inhalation
R27: Very toxic in contact with skin
R28: Very toxic if swallowed
R29: Contact with water liberates toxic gas
R30: Can become highly flammable in use
R31: Contact with acids liberates toxic gas
R32: Contact with acids liberates very toxic gas
R33: Danger of cumulative effects
R34: Causes burns
R35: Causes severe burns
R36: Irritating to eyes
R37: Irritating to respiratory system

R38: Irritating to skin
R39: Danger of very serious irreversible effects
R40: Possible risk of irreversible effects
R41: Risk of serious damage to eyes
R42: May cause sensitization by inhalation
R43: May cause sensitization by skin contact
R44: Risk of explosion if heated under confinement
R45: May cause cancer
R46: May cause heritable genetic damage
R47: May cause birth defects
R48: Danger of serious damage to health by prolonged exposure
R49: May cause cancer by inhalation
R50: Very toxic to aquatic organisms
R51: Toxic to aquatic organisms
R52: Harmful to aquatic organisms
R53: May cause long-term adverse effects in the aquatic environment
R54: Toxic to flora
R55: Toxic to fauna
R56: Toxic to soil organisms
R57: Toxic to bees
R58: May cause long-term adverse effects in the environment
R59: Dangerous to the ozone layer
R60: May impair fertility
R61: May cause harm to the unborn child
R62: Possible risk of impaired fertility
R63: Possible risk of harm to the unborn child
R64: May cause harm to breastfed babies
R65: Harmful: may cause lung damage if swallowed
R66: Repeated exposure may cause skin dryness or cracking
R67: Vapors may cause drowsiness and dizziness
R68: May cause irreversible effects

Combination of risks

R14/15: Reacts violently with water, liberating highly flammable gases
R15/29: Contact with water liberates toxic, highly flammable gas
R20/21: Harmful by inhalation and in contact with skin
R20/21/22: Harmful by inhalation, in contact with skin and if swallowed
R20/22: Harmful by inhalation and if swallowed
R21/22: Harmful in contact with skin and if swallowed

R23/24: Toxic by inhalation and in contact with skin
R23/24/25: Toxic by inhalation, in contact with skin and if swallowed
R23/25: Toxic by inhalation and if swallowed
R24/25: Toxic in contact with skin and if swallowed
R26/27: Very toxic by inhalation and in contact with skin
R26/27/28: Very toxic by inhalation, in contact with skin and if swallowed
R26/28: Very toxic by inhalation and if swallowed
R27/28: Very toxic in contact with skin and if swallowed
R36/37: Irritating to eyes and respiratory system
R36/37/38: Irritating to eyes, respiratory system and skin
R36/38: Irritating to eyes and skin
R37/38: Irritating to respiratory system and skin
R42/43: May cause sensitization by inhalation and skin contact.
R48/20: Harmful: danger of serious damage to health by prolonged exposure
R48/20/21: Harmful: danger of serious damage to health by prolonged exposure through inhalation and in contact with the skin
R48/20/21/22: Harmful: danger of serious damage to health by prolonged exposure through inhalation, in contact with skin and if swallowed
R48/20/22: Harmful: danger of serious damage to health by prolonged exposure through inhalation, and if swallowed
R48/21: Harmful: danger of serious damage to health by prolonged exposure in contact with skin
R48/21/22: Harmful: danger of serious damage to health by prolonged exposure in contact with skin and if swallowed
R48/22: Harmful: danger of serious damage to health by prolonged exposure if swallowed
R48/23: Toxic: danger of serious damage to health by prolonged exposure through inhalation
R48/23/24: Toxic: danger of serious damage to health by prolonged exposure through inhalation and
in contact with skin
R48/23/24/25: Toxic: danger of serious damage to health by prolonged exposure through inhalation, in contact with skin and if swallowed
R48/23/25: Toxic: danger of serious damage to health by prolonged exposure through inhalation and if swallowed
R48/24: Toxic: danger of serious damage to health by prolonged exposure in contact with skin
R48/24/25: Toxic: danger of serious damage to health by prolonged exposure in contact with skin and if swallowed
R48/25: Toxic: danger of serious damage to health by prolonged exposure if swallowed

R50/53: Very toxic to aquatic organisms, may cause long term adverse effects in the aquatic environment
R51/53: Toxic to aquatic organisms, may cause long term adverse effects in the aquatic environment
R52/53: Harmful to aquatic organisms, may cause long-term adverse effects in the aquatic environment
R68/20: May cause irreversible effects by inhalation
R68/21: May cause irreversible effects in contact with skin
R68/22: May cause irreversible effects if swallowed
R68/20/21: May cause irreversible effects by inhalation and in contact with skin
R68/20/22: May cause irreversible effects by inhalation and if swallowed
R68/21/22: May cause irreversible effects in contact with skin and if swallowed
R68/20/21/22: May cause irreversible effects by inhalation, in contact with skin and if swallowed

Safety precaution phrases (S-Phrases)

S1: Keep locked up
S2: Keep out of reach of children
S3: Keep in a cool place
S4: Keep away from living quarters
S5: Keep contents under … (appropriate liquid to be specified by the manufacturer)
S6: Keep under … (inert gas to be specified by the manufacturer)
S7: Keep container tightly closed
S8: Keep container dry
S9: Keep container in a well ventilated place
S12: Do not keep the container sealed
S13: Keep away from food, drink and animal feeding stuffs
S14: Keep away from … (incompatible materials to be indicated by the manufacturer)
S15: Keep away from heat
S16: Keep away from sources of ignition-No Smoking
S17: Keep away from combustible material
S18: Handle and open container with care
S20: When using do not eat or drink
S21: When using do not smoke
S22: Do not breathe dust
S23: Do not breathe gas/fumes/vapour/spray (appropriate wording to be

specified by manufacturer)
S24: Avoid contact with skin
S25: Avoid contact with eyes
S26: In case of contact with eyes, rinse immediately with plenty of water and seek medical advice
S27: Take off immediately all contaminated clothing
S28: After contact with skin, wash immediately with plenty of … (to be specified by the manufacturer)
S29: Do not empty into drains
S30: Never add water to this product
S33: Take precautionary measures against static discharges
S34: Avoid shock and friction
S35: This material and its container must be disposed of in a safe way
S36: Wear suitable protective clothing
S37: Wear suitable gloves
S38: In case of insufficient ventilation, wear suitable respiratory equipment
S39: Wear eye/face protection
S40: To clean the floor and all objects contaminated by this material use (to be specified by the manufacturer)
S41: In case of fire and/or explosion do not breath fumes
S42: During fumigation/spraying wear suitable respiratory equipment (appropriate wording to be specified by the manufacturer)
S43: In case of fire, use … (indicate in the space the precise type of fire fighting equipment. If water increases the risk, add "never use water")
S44: If you feel unwell, seek medical advice (show the label where possible)
S45: In case of accident or if you feel unwell, seek medical advice immediately (show the label where possible)
S46: If swallowed, seek medical advice immediately and show the container or label
S47: Keep at temperature not exceeding … °C (to be specified by the manufacturer)
S48: Keep wetted with … (appropriate material to be specified by the manufacturer)
S49: Keep only in the original container
S50: Do not mix with … (to be specified by the manufacturer)
S51: Use only in well ventilated areas
S52: Not recommended for interior use on large surface areas
S53: Avoid exposure - obtain special instructions before use
S54: Obtain the consent of pollution control authorities before discharging to waste-water treatment plants
S55: Treat using the best available techniques before discharge into drains or

the aquatic environment
S56: Do not discharge into drains or the environment, dispose to an authorized waste collection point
S57: Use appropriate containment to avoid environmental contamination
S58: To be disposed of as hazardous waste
S59: Refer to manufacturer/supplier for information on recovery/recycling
S60: This material and/or its container must be disposed of as hazardous waste
S61: Avoid release to the environment. Refer to special instructions / safety data sheet
S62: If swallowed, do not induce vomiting: seek medical advice immediately and show the container or label
S63: In case of accident by inhalation: remove casualty to fresh air and keep at rest
S64: If swallowed, rinse mouth with water (only if the person is conscious)

Combined safety phrases

S1/2: Keep locked up and out of reach of children
S3/9: Keep in a cool, well ventilated place
S3/7/9: Keep container tightly closed in a cool, well ventilated place
S3/14: Keep in a cool place away from …(incompatible materials to be indicated by the manufacturer)
S3/9/14: Keep in a cool, well ventilated place away from …(incompatible materials to be indicated by the manufacturer)
S3/9/49: Keep only in the original container in a cool, well ventilated place
S3/9/14/49: Keep only in the original container in a cool, well ventilated place away from (incompatible materials to be indicated by the manufacturer)
S3/9/49: Keep only in the original container in a cool, well ventilated place
S3/14: Keep in a cool place away from…(incompatible materials to be indicated by the manufacturer)
S7/8: Keep container tightly closed and dry
S7/9: Keep container tightly closed and in a well ventilated place
S7/47: Keep container tightly closed and at a temperature not exceeding… °C (to be specified by manufacturer
S20/21: When using do not eat, drink or smoke
S24/25: Avoid contact with skin and eyes
S29/56: Do not empty into drains, dispose of this material and its container to hazardous or special waste collection point
S36/37: Wear suitable protective clothing and gloves
S36/37/39: Wear suitable protective clothing, gloves and eye/face protection

S36/39: Wear suitable protective clothing, and eye/face protection
S37/39: Wear suitable gloves and eye/face protection
S47/49: Keep only in the original container at temperature not exceeding… °C (to be specified by the manufacturer)

Anton Myalitsin

Personal Data

Place and Date of Birth: Protvino, Russia | 04 November 1982
Nationality: German
Address: Institute of Physical Chemistry
University of Hamburg
Grindelallee 117, 20146 Hamburg, Germany
Phone: +49 40 42838 7631
email: myalitsin@chemie.uni-hamburg.de

Education

Sep 2007	Master of Science in Chemistry, **University of Siegen**, Siegen Thesis: "Optical and Electrical Properties of CdSe Nanowires" | Advisor: Prof. A. Mews
Sep 2005	Bachelor of Science in Chemistry, **University of Siegen**, Siegen Thesis: "Studies of Trifluorotris(perfluorethyl)phosphates and Synthesis of Novel Cyano(perfluorethyl)phosphates" | Advisor: Prof. H.-J. Deiseroth
Jun 2003	Abitur (secondary school leaving examination), **Fürst-Johann-Moritz-Gymnasium**, Siegen

Experience

Oct 2007 - *Current*	**University of Hamburg**, Hamburg and **University of Siegen**, Siegen, Germany PhD research at the Institute of Physical Chemistry and the "Interdisciplinary Nanoscience Centre Hamburg" (INCH), Hamburg and Department of Chemistry-Biology, Siegen. Advised two graduate students.
Oct 2005 - *Current*	**University of Hamburg**, Hamburg and **University of Siegen**, Siegen, Germany Teaching Assistant: Intermediate Physical Chemistry Exercises and Physical Chemistry Lab Course for Bachelor students.
Oct 2005 - Sep 2007	**University of Siegen**, Siegen, Germany Studies towards MSc.
Mar 2005 - Aug 2005	**Bergsche University of Wuppertal**, Wuppertal, Germany Bachelor thesis; student assistant at the "Ionic Liquids" devision of Merck in Wuppertal, Germany.
Oct 2003 - Sep 2005	**University of Siegen**, Siegen, Germany Undergraduate studies towards BSc.

Scholarships and Certificates

Sep 2005	Haeuseler Award of the University of Siegen (Departmental Undergraduate Award)
2004 - 2007	Scholarship of the German National Academic Foundation. http://www.studienstiftung.de/

Projects

German National Academic Foundation Summer Schools:

2007	Guidel, France: Nanoscience
2006	Guidel, France: Nanophotonics
2004	Olang, Italy: Paradoxes of the Special Relativity

Other:
2006 Prague: “Crossborders”, Introduction to McKinsey case studies

Publications

1. A. Myalitsin, Ch. Strelow, Zh. Wang, Zh. Li, T. Kipp, A. Mews (*accepted*): *Diameter scaling of the optical band gap in individual CdSe nanowires.*
2. Y. Cai, D. Wolfkuehler, A. Myalitsin, J. Perlich, A. Meyer, Ch. Klinke (2011): *Tunable Electrical Transport through Annealed Monolayers of Monodisperse Cobalt-Platinum Nanoparticles*; ACS Nano **5**, *1*, 67.
3. B. Ritz, H. Heller, A. Myalitsin, A. Kornowski, F. J. Martin-Martinez, S. Melchor, J. A. Dobado, B. H. Juarez, H. Weller and Ch. Klinke (2010): *Reversible Attachment of Platinum Alloy Nanoparticles to Nonfunctionalized Carbon Nanotubes*; ACS Nano **4**, 2438.
4. N. Fu, Z. Li, A. Myalitsin, M. Scolari, R. T. Weitz, M. Burghard and A. Mews (2010): *One-Dimensional Heterostructures of Single-Walled Carbon Nanotubes and CdSe Nanowires*; Small **6**, 376.
5. Z. Li, A. Kornowski, A. Myalitsin and A. Mews (2008): *Formation and Function of Bismuth Nanocatalysts for the Solution-Liquid-Solid Synthesis of CdSe Nanowires*; Small **4**, 1698.
6. M. Scolari, A. Mews, N. Fu, A. Myalitsin, T. Assmus, K. Balasubramanian, M. Burghard and K. Kern (2008): *Surface enhanced Raman scattering of carbon nanotubes by individual fluorescent gold particles*; Journal of Physical Chemistry C, **112**, 391.
7. T. Assmus, K. Balasubramanian, M. Burghard, K. Kern, M. Scolari, N. Fu, A. Myalitsin and A. Mews (2007): *Raman properties of gold nanoparticle-decorated individual carbon nanotubes*; Applied Physics Letters **90** 173109.

Conferences

Talks:
European Material Research Society (E-MRS) Spring Meeting, 2011, (Nice, France)
German Fluorine Conference, 2006 (Schmitten, Germany)
Posters:
German Physical Chemistry Society Meeting, 2011 (Berlin, Germany): Analysis and Control of Ultrafast Photoinduced Reactions
German Colloid Society Meeting, 2009 (Hamburg, Germany)
German Physical Chemistry Society Meeting, 2008 (Saarbruecken, Germany): Analysis, Manipulation and Simulation on the Nanometer Scale

References

Alf Mews	University of Hamburg	mews@chemie.uni-hamburg.de
Marko Burghard	MPI for Solid State Research	m.burghard@fkf.mpg.de
Christian Klinke	University of Hamburg	klinke@chemie.uni-hamburg.de

Languages

German: Mothertongue
Russian: Mothertongue
English: Fluent